Engineered graphene Josephson junctions probed by quantum interference effects

Inauguraldissertation

zur
Erlangung der Würde eines Doktors der Philosophie
vorgelegt der
Philosophisch-Naturwissenschaftlichen Fakultät
der Universität Basel

von

David Indolese

Basel, 2020

Genehmigt von der Philosophisch-Naturwissenschaftlichen Fakultät
auf Antrag von
Prof. Dr. Christian Schönenberger
Prof. Dr. Richard Warburton
Prof. Dr. Sophie Guéron
Dr. Srijit Goswami

Basel, 13.10.2020

Prof. Dr. Martin Spiess
Dekan

Widmung

Diese Arbeit widme ich meiner Frau Bettina für ihre stetige und
immerwährende Unterstützung.

Contents

Contents

1 Introduction

In today's fundamental research many groups at universities and companies around the globe dedicate their time, knowledge and efforts to study quantum physics in electronic structures on the nanometer scale. One very practical reason is to explain the performance and limitations of classical processors and transistors in the future, which undergo a steady miniaturization according to the phenomenological Moore's law. But besides this, much more fundamental questions are asked and want to be answered, like: What is the underlying physics of these quantum devices? How can we explain the behavior of electrons on the nano scale and low dimensional systems? How can we control and engineer quantum states? How can we make use of the quantum nature? Can it be used for computation? These questions are driving the field of condensed matter physics, nano scale fabrication, and electron transport further and further. New insights are gained day by day, new materials are developed and the limits are pushed beyond the state of the art.

As indicated by the previous questions, a major goal is to find a way to realize computation using quantum mechanical states instead of classical bits. While a classical bit can be either in the state 0 or 1, a quantum bit can be in a superposition of both states. This will allow to perform certain calculations much faster than on a classical computer, to encrypt and communicate informations, and to simulate quantum mechanical systems like molecules, which can be used to design new materials or medicine [1, 2]. The quantum bit is not only an object in the studies of universities but also enterprises like Google, IBM, and Microsoft investing time and money in this technology due to its huge potential.

Most of the approaches towards the quantum computer include superconductors [3]. A superconductor is a material, which loses its electrical resistance and shows perfect diamagnetic behavior when cooled below a certain temperature [4, 5]. The combination of superconductor and low dimensional quantum devices is expected to generate new quantum mechanical states in condensed matter that are unaffected by external influences, which is in general not the case. Often these studies include the investigation of low-dimensional superconducting hybrid devices in a magnetic field. The interaction between superconductivity and magnetic fields is everything else but trivial, which makes this field an interesting play ground to learn more about the individual com-

ponents and their interplay.

In the center of this thesis stands graphene, a true two-dimensional conductor, in contact with superconducting materials. Graphene itself is an one atom thick layer of carbon atoms arranged in a honeycomb lattice and was extracted the first time in 2004 by Novoselov et al. [6]. Before its discovery, it was even questioned, if a two-dimensional crystal can even exist due to thermodynamical instability [7, 8]. Since then an entire family of two-dimensional materials was found and every member brought its own unique physical properties into play, like boron-nitride an insulator, which can serve as a substrate [9] or tunnel barrier [10], tungsten-diselenide a semiconductor, which shows a strong spin-orbit coupling [11], tungsten-ditelleride a topological insulator hosting conductive hinge states [12–14], niobium-diselenide a superconductor [15] or chromium-triiodide a ferromagnetic insulator [16], just to mention a few to show the extreme diversity of two-dimensional materials. Soon after the exfoliation of graphene, it was realized that novel materials with combined or new properties can be engineered by pairing different 2D materials in layered structures [17–22] and control the alignment of their crystal structures [23–25].

In this thesis we used the ability of stacking different 2D material to create high quality electronic devices and to engineer counter propagating edge states in multilayer graphene structures. The coupling of the structures to superconductors is then studied in the scope of magnetic field dependence, crystal orientations, and device structures.

Outline of the thesis

In the beginning of the thesis the theoretical background of the investigated physical phenomena is given in Ch.2. In Ch.3 the fabrication of the nano structures is described and some of basic properties of graphene based Josephson junction with superconducting molybdenum-rhenium contacts are summarized. In the end of the chapter the applied methods for processing the data are explained. Afterwards the results of the supercurrent transport in superlattices of graphene and boron-nitride are summarized, which reveal the existence of van Hove singularities and satellite Dirac points in the band structure. In Ch.5 different realized approaches to create a helical quantum Hall state in graphene are described using the engineering of van der Waals heterostructures. The potential coupling of the helical states to superconductors was investigated. In the last experimental chapter, Ch.6, we focus on the magnetic field dependence of a double layer graphene heterostructure and show by current-phase relation measurements, that highly transparent superconducting modes exists within both graphene layers. In Ch.7 a summary of the thesis is given and possibilities of future experiments are sketched.

2 Theoretical background
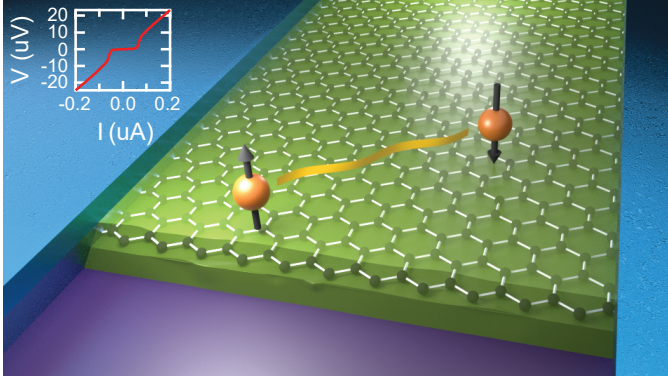
In this chapter we give the theoretical background regarding the physical phenomena investigated through out this thesis. It starts with a brief overview about superconductivity with a following introduction on superconducting proximity effects. Especially, the physical properties of Josephson junctions are described. Then, the graphene's linear bandstructure is discussed using the tight binding approximation and its change under the presence of a hBN-graphene superlattice is shown. After an overview of ballistic and diffusive electron transport in graphene, the concept of electrostatically defined Fabry-Pérot cavities is introduced and how they influence the electron transport. Furhter, we take a look at the quantum Hall effect in graphene and discuss the extraordinary properties of the 0th Landau level and its possible ground states. The last part of the chapter is dedicated to recently observed superconducting correlations in graphene based superconducting hybrid devices in the quantum Hall regime and the major findings are summarized.

2.1. Superconductivity and the Josephson effect

In 1911 Kamerlingh Onnes surprisingly observed that the electrical resistance of mercury, lead and tin vanishes at low temperatures [4] (see Fig.2.1 a). Later it was found that these materials not only carry a dissipationless current, but that they show as well a perfect diamagnetic behavior, such that any magnetic field is screened and its magnitude inside the materials is zero [5], except in a small region, given by the London penetration depth (λ_L), at the material's boundaries. These materials are called superconductors. Both phenomena appear when the superconductor is cooled down below its specific critical temperature (T_c). Just like the T_c, a critical magnetic field (B_c) exists. When the value of the applied magnetic field exceeds B_c the superconductivity breaks down, since expelling of the external magnetic field needs energy, which will overcome the condensation energy of the superconducting state. It was found that two kinds of superconductor exist with distinct different behavior in magnetic field. While type I superconductors fully expel the external magnetic field up to B_c, type II superconductors can host vortices of one magnetic flux quantum. These Abrikosov vortices appear at magnetic fields above B_c^1 without destroying the perfect conductivity, which vanishes as soon as the value of the second critical magnetic field B_c^2 is exceeded. A current flowing in a conductor creates as well a magnetic field, such that there exists a upper limit for the amount of dissipationless supercurrent, the critical current (I_c). Even though current is carried perfectly below T_c, it was observed that the heat conduction vanishes and decays exponentially with temperature below T_c attributed to a gap in the quasiparticle density of states [26].

A microscopic model to explain the phenomena of superconductivity was developed in 1957 by Bardeen, Cooper and Schriefer: the BCS theory [27]. They proposed an attractive interactions between electrons mediated by phonons, which pair electrons of opposite momentum and spin to Cooper pairs. These pairs of electrons condense around the Fermi energy (E_F) into the same quantum mechanical state. The pairing happens in an energy window given by the superconducting gap Δ, which creates a gap in the density of states (DoS). The quasi-particle, unpaired electrons, DoS was calculated to be equal to

$$\mathrm{DoS}_q(E) = \mathrm{DoS}_n(E_F)\frac{|E - E_F|}{\sqrt{(E - E_F)^2 - \Delta^2}} \text{ if } |E - E_F| > \Delta$$

$$\text{and } 0 \text{ otherwise,} \tag{2.1}$$

where DoS_q is DoS of the quasi-particles in the superconducting state, DoS_n is the DoS in the normal state, and E the energy of the particle. A schematic drawing of DoS_q and DoS_n is shown in Fig.2.1 b.

Already before the BCS-theory, Ginzburg and Landau developed a phenomenological description by introducing the superconducting wave function
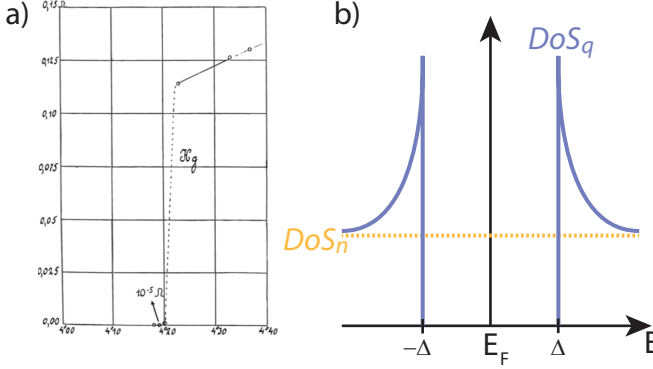
Figure 2.1. a) Resistance as a function of temperature for mercury. The figure is adapted from Ref.[4]. b) Density of states of the quasi-particles in the superconducting state shown in blue ($T_c > T$) and in the normal state shown in yellow ($T_c < T$). A gap of 2Δ manifests itself around E_F in the superconducting state.

$\psi(\vec{r},t) = \sqrt{n_s(\vec{r},t)}e^{i\varphi(\vec{r},t)}$, where $n_s(\vec{r},t)$ corresponds to the local Cooper pair density and φ to the macroscopic phase of the superconductor. Within this model the coherence length (ξ_s) of the superconducting state, λ_L, B_c, and the spatial variation of the superconducting order parameter ψ could be described successfully. For further reading and detailed derivations I would like to refer to Tinkham's book "Introduction to superconductivity" [28] and Heikkilä's book "The Physics of Nanoelectronics" [29].

2.1.1. Superconducting proximity effects

In this thesis we studied the interplay between superconductors and graphene, i.e. a two-dimensional (2D) conductor. It has been shown that superconducting correlations can be found in a non-superconducting material, if it is brought into electrical contact with a superconductor. One of the most prominent consequence of this fact is the Jospheson effect [30], where dissipation-less current is carried through a tunnelling junction. Even though, he made his calculation for a superconductor-insulator-superconductor (SIS) junction, it has been shown that it is valid in more general cases and also apply to junctions, where the insulator is replaced by another weak link, like a metal (N), graphene [31], a semiconductor, a ferromagnet or a constriction [32].

In the following we will discuss the electron energy dependent reflection at a NS interface, from which we derive the energy of possible states in the normal

part of a SNS Josephson junction (JJ). Depending on the number of states and their transparency one can then derive the relation between the supercurrent and the superconducting phase difference across the junction. In the end the influence of a magnetic field on the supercurrent flowing in a SNS junction is explained.

Andreev reflection

An important first step to understand the physics of a SNS device is to explore the effects taking place at a single NS interface. Especially, we will now discuss the energy dependent reflection of an electron approaching the NS interface coming from the normal conductor.

The electron has a certain energy ε, which is measured with respect to E_F. If this energy is smaller than Δ, the electron can not enter into the superconductor since DoS_q is gapped. The electron can now be reflected as an electron off the interface, but what also can happen is that the electron forms a Cooper pair with an other electron from N with an energy of $-\varepsilon$ and opposite momentum and spin as shown in Fig.2.2 a for the bandstructure of graphene. This pair can enter the superconductor and a charge of $2e$, where e is the electron charge, is transmitted via the interface. If the electron's energy is larger than Δ, it could enter the superconductor as a quasi-particle with the same energy.

However, we will focus on the situation when $\varepsilon < \Delta$. As mentioned the electron can not just be transmitted across the interface, but has to form a Cooper pair with a second electron. This can also be seen as it undergoes a so called Andreev reflection meaning that the incoming electron is reflected as a hole with opposite propagation direction (see Fig.2.2 b). The probability to undergo this kind of reflection depends strongly on the interface transparency. The influence of the transparency was investigated by Blonder et al. [33] by introducing a repulsive potential given by $H\delta(x)$, where H is the barrier height and δ the Dirac function. The transparency (t) is then given by $t = 1/(1+Z^2)$, where $Z = H/\hbar v_F$ with $\hbar$ the reduced Plank constant and v_F the Fermi velocity. For perfect transmitting interfaces it was found that the conductance should double for $\varepsilon < \Delta$ compared to $\varepsilon > \Delta$, since every electron is reflected as a hole leading to a charge transfer of $2e$ into the superconductor. However, for a small t the conductance is suppressed in the gap, since the Andreev reflection processes have a probability of t^2, and in the tunneling regime the conductance mimics the DoS of the SC electrode.

The Andreev reflection problem can be solved by matching the wave functions, which are solutions from the Bogoliubov-de Gennes equations, at the NS interface [29, 33]. An Andreev reflection is a phase coherent process, in which the reflected hole picks-up a phase difference $\delta\phi$ with respect to the electron

given by ε and φ.

$$\delta\phi = -\arccos(\varepsilon/\Delta) \pm \varphi, \tag{2.2}$$

where the + sign describes the phase difference, when an electron reflects as a hole, and the - sign the case of a incoming hole being reflected as an electron [34] .

The previous discussion was made under the assumption that $E_F \gg \Delta$, which leads to retroreflection of the hole within the same electronic band. In graphene, a zero band gap semiconductor (see Sec.2.2), an additional process is possible close to the Dirac point (DP), when $E_F < \Delta$. Instead of being retro reflected, which is an intraband process, the hole can be reflected specular, e.g. an electron of the conduction band is reflected as a hole in the valence band. In the latter case, which is an interband process, the velocity parallel to the contact is the same for the incoming electron and the reflected hole [35, 36] (see Fig.2.2 b & c), which means that the electron and hole do not counter propagate as in the previous case.

Andreev bound states

Lets consider now the situation where two superconductors are connected by a normal material of length L. As shown in Fig.2.3 a a right moving electron can undergo an Andreev reflection at the right superconductor. The reflected hole may reach again the left superconductor and is then converted into an electron moving to the right. This process is sketched in Fig.2.3 a. The electron and the hole pick-up a phase of $k_{e/h}L$, while moving in the normal material from one superconductor to the other, where $k_{e/h}$ is the wave vector of the electron or the hole, respectively. In addition, as discussed in the previous section, a phase difference $\delta\phi$ is obtained during the two Andreev reflections. This leads to a total phase of

$$\phi_{tot} = (k_e + k_h)L + \Delta\varphi - 2\arccos(\varepsilon/\Delta), \tag{2.3}$$

picked-up by the Andreev pair during one cycle, where $\Delta\varphi$ is equal to the phase difference of the two superconductors. It is also possible that the electron and hole travel in the opposite direction as described before, which would lead to a minus sign in front of $\Delta\varphi$, k_e and k_h. For perfect NS interfaces the reflected hole has the opposite momentum of the electron, and in the case of graphene is reflected into the other valley [37]. The sum of $k_e = k_F + \frac{\varepsilon}{\hbar v_F}$ and $k_h = -k_F + \frac{\epsilon}{\hbar v_F}$ can be written as $k_e + k_h = \frac{2\varepsilon}{\hbar v_F} = \frac{2}{\xi}\frac{\varepsilon}{\Delta}$, where $\xi = \frac{\hbar v_F}{\pi\Delta}$ is the superconducting coherence length in the weak link for the ballistic electron transport in N and k_F the wave vector at E_F. To obtain a bound state the total phase difference has to be equal to zero modulo 2π. This leads to the condition

$$-2\arccos(\varepsilon/\Delta) + \Delta\varphi + \frac{2L\varepsilon}{\xi\Delta} = 0 \ [mod \ 2\pi]. \tag{2.4}$$
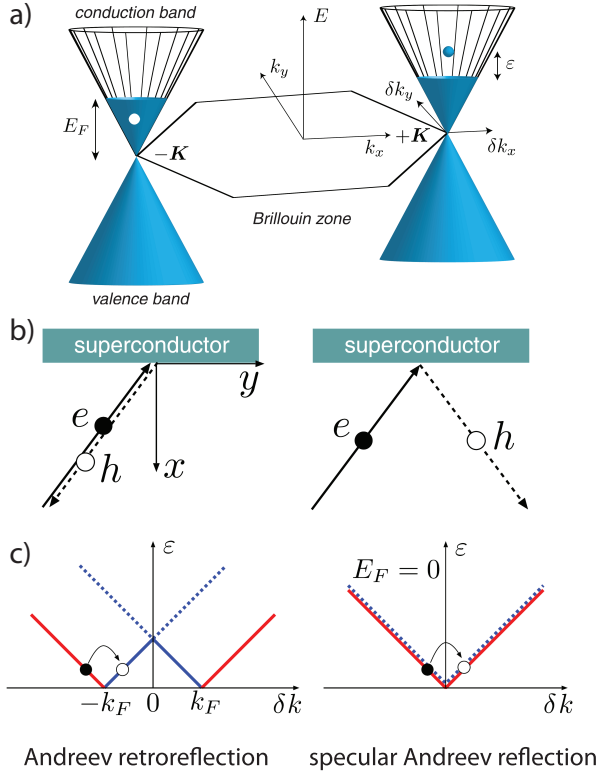
Figure 2.2. a) Electron (filled circle) and hole (empty circle) excitations in the bandstructure of graphene. During an Andreev reflection they convert into each other at the superconductor. b) (Left) Andreev retro-reflection at a NS interface. (Right) Specular Andreev reflection between the undoped graphene and the superconductor. The arrows indicate the direction of travel and solid or dashed lines, whether the particle is a negatively charged electron or a positively charged hole. c) Dispersion relation of graphene for two values of E_F for the case of normal incidence ($\delta k_y = 0, \delta k_x = \delta k$). The blue and red lines correspond to the electron band and the hole band, while the solid (dashed) lines stands for the conduction (valence) band. In the left panel the electron-hole conversion is shown for the case of retro-reflection at the NS interface and on the right the conversion of an electron in the conduction band into a hole in the valance band is shown. This figure is adapted from Ref.[35]

Two distinct different cases are now given depending on the ratio of ξ and L. If $L \ll \xi$ the junction is in the short regime, such that the additional phase coming from the propagation in the normal conductor can be neglected. While in the long junction limit $L > \xi$ the additional phase has to be taken into account. Note, that the ξ depends on the transport nature, ballistic or diffusive, of the weak link and is given by $\xi = \frac{\hbar v_F}{\pi \Delta}$ for the ballistic case and $\xi = \sqrt{\frac{\hbar D}{\Delta}}$ for the diffusive case [28], where D is the diffusion constant.

Long and short junction limit

Now, we will discuss the difference between the short and long junction limit in more detail. If L is smaller than ξ the JJ is in the short junction limit. This means that the phase picked-up by the electron and hole, while passing the normal region, can be neglected and Eq.2.4 simplifies to $2 \arccos(\varepsilon/\Delta) = \Delta\varphi$. The solution of this equation gives then the Andreev bound state energy (E^{ABS}) as a function of the phase difference between the two superconductors.

$$E^{ABS} = \pm\Delta \cos(\Delta\varphi/2). \qquad (2.5)$$

This means that besides the gaped DoS in the normal region caused by the induced superconducting correlations, a discrete state exists within Δ, which carries the supercurrent. At zero temperature only states with $E^{ABS} < 0$ are occupied. This is also true for the long junction limit described below.
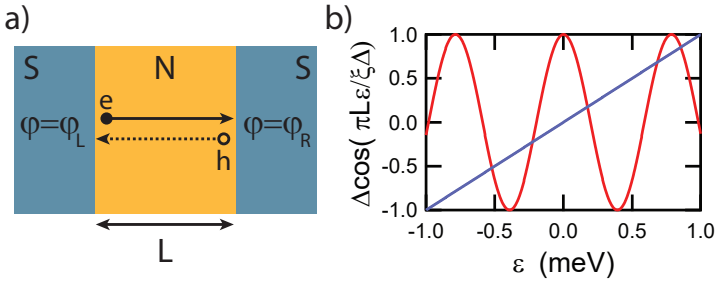
Figure 2.3. a) Schematic drawing of a JJ. The filled (empty) circle corresponds to an electron (hole) moving to the right (left). The electron and hole are converted into each other at the NS interface forming an Andreev pair. b) Graphic solution of Eq.2.6 for $\varepsilon \in (-\Delta, \Delta)$, where Δ is equal to $1\,\mathrm{meV}$. The junction length is chosen to be 8 times larger than ξ and $\Delta\varphi = 0$.

In the long junction limit, where $L > \xi$, the solutions for the possible An-

dreev bound state are determined by

$$\varepsilon = \pm\Delta \cos\left(\Delta\varphi/2 + \frac{L}{\xi}\frac{\varepsilon}{\Delta}\right). \tag{2.6}$$

In this case there exists more than one solution for ε. The graphical solution of Eq.2.6 is shown in Fig.2.3 b for $\varepsilon \in (-\Delta, \Delta)$, $\Delta\varphi = 0$ and $\Delta = 1\,\mathrm{meV}$. It can be seen that in the long junction limit several solutions for Andreev bound states exist in energy, which number depends on the ratio of L and ξ. By assuming ε is small, i.e. $\epsilon \ll \Delta$, the solutions are given by setting the right side of Eq.2.6 equal to zero, which leads to

$$\frac{\Delta\varphi}{2} + \frac{L\varepsilon}{\xi\Delta} = \frac{\pi}{2} + j\pi, \tag{2.7}$$

where j is a integer number. The spacing in energy of different solutions is given by $1/2$ times the Thouless energy $E_{th} = \frac{\hbar v_F}{L}$. A gap of E_{th} exists for $\Delta\varphi = 0$ in the normal conductor, while it closes for $\Delta\varphi = \pi$. The superconducting gap Δ is therefore filled with many Andreev bound states, which all contribute to the supercurrent transport [38]. During all previous discussions we assumed prefect transmission, which leads to states at zero energy at $\Delta\varphi = \pi$. For imperfect NS interfaces a gap in the Andreev bound state spectrum is also present at this phase point.

Situation for imperfect NS interface

Let's consider for now the situation of a short JJ. In contrast to the previous case, we assume that the transparency (t) of the NS interface is not perfect, i.e. $t \neq 1$. In the presence of normal reflection at the contacts it can be shown, that E^{ABS} depends on t [34] and given by

$$E^{ABS} = \pm\Delta[1 - t\sin^2(\Delta\varphi/2)]^{1/2}. \tag{2.8}$$

A channel with $t \ll 1$ only varies slightly its energy as a function of $\Delta\varphi$ and sticks to the gap edge, while a channel with $t \approx 1$ shows a strong phase dependence (see Fig.2.4 a). The spacing between the Andreev bound states can be probed with tunneling spectroscopy [39, 40] or by microwave spectroscopy [41, 42], from which the number of Andreev bound states, their transparency and sources of dissipation in the system can be measured [43, 44]. The phase dependent Andreev bound states and the supercurrent carried by them are directly related to each other, which is the subject of the next section.

The current phase relation

The supercurrent in a SNS junction is carried by the Andreev bound states, which energies depend on $\Delta\varphi$. During one cycle including two Andreev reflections one Cooper pair is transported from one superconductor to the other. The supercurrent, which is carried by the bound states in a short Josephson junction, is given by

$$I_s = \frac{2\pi}{\Phi_0} \sum_n \frac{\delta E_n^{ABS}}{\delta \Delta\varphi} = \frac{e\Delta}{2\hbar} \sum_n \frac{t_n \sin(\Delta\varphi)}{\sqrt{1 - t_n \sin^2(\Delta\varphi/2)}}, \tag{2.9}$$

where Φ_0 is the flux quantum and t_n the transparency of the nth channel [34]. This expression determines the dependence of I_s with respect to the phase difference between the superconductors known as the current phase relation (CPR). Note, that the CPR is 2π periodic in the phase and is an odd function in $\Delta\varphi$ with respect to 0. Only if the chiral and time reversal symmetry are broken a supercurrent was observed even at $\Delta\varphi = 0$ [45]. In the case of $t \ll 1$ as for a tunnel junction we find the equation for the dc-Josephson effect, $I_s = I_c \sin(\Delta\varphi)$, which was proposed by Josephson [30]. If $t \gg 0$ the E^{ABS} depends strongly on $\Delta\varphi$ as mentioned. The current phase relation is then not longer sinusoidal but contains higher harmonics, i.e. $\sin(j\Delta\varphi)$, where j is an integer number. This leads to a deviation of the CPR's maxima from $\pi/2$ to a value between $\pi/2$ and π. How much this maxima is shifted away form $\pi/2$ can be either measured by the relative contribution of the higher harmonics to the CPR or by the skewness $S = \frac{\Delta\varphi_{max} - \pi/2}{\pi/2}$, where $\Delta\varphi_{max}$ is the position of the maximum of the CPR in the phase. Therefore, S characterizes the contribution from high transmissive channels.
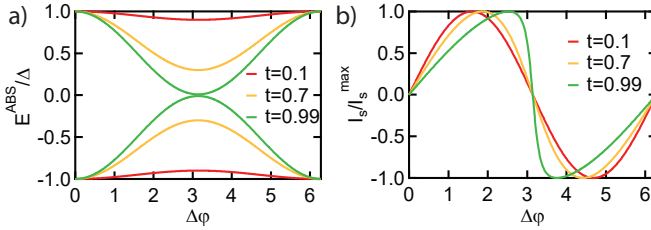

Figure 2.4. a) Andreev bound state energy normalized to the superconducting gap as a function of phase difference. E^{ABS} was calculated for three different transparencies using Eq.2.8. b) Normalized supercurrent as a function of phase difference for a single channel calculated from Eq.2.9 for three different transparencies.

Ambegaokar-Baratoff relation

Ambegaokar and Baratoff derived the relation between the normal state resistance (R_N) and I_c for a superconducting tunnelling junction [46], which also immediately follows form Eq.2.9

$$I_c = \frac{\pi\Delta}{2eR_N},\tag{2.10}$$

where $R_N = \sum_n t_n 2e^2/h$. In the long junction regime E_{th}, which becomes the relevant energy scale, will replace Δ in Eq.2.10, such that $R_N I_c = \alpha E_{th}$. The prefactor α depends on the diffusive or ballistic nature of the JJ [47–50].

In the following we will discuss the influence of a magnetic field on the Josephson effect and how it can be used to measure the CPR or the supercurrent distribution in a JJ.

2.1.2. Magnetic field interference effects

The magnetic field dependence of the superconducting phase is a fundamental property and also shows its effect in the supercurrent carried by a JJ or in a superconducting quantum interference device (SQUID). In the previous discussions we referred to the phase difference across a JJ by $\Delta\varphi$. This quantity is not gauge-invariant meaning that it can not determine I_s for a general situation like in a magnetic field, while I_s is actually gauge-invariant. Therefore, $\Delta\varphi$ has to be redefined as a gauge-invariant, which can be done by replacing the original expression of $\Delta\varphi$ with $\Delta\varphi = (\varphi_L - \varphi_R) - \frac{2\pi}{\Phi_0}\vec{A}(\vec{r},t)$, where ϕ_L is the phase of the left and ϕ_R the phase of the right superconductor. The gauge-invariant form is needed to investigate the influence of magnetic fields on the supercurrent, since it introduces the vector potential $\vec{A}$ with $\vec{B} = \vec{\nabla}\times\vec{A}$. For the magnetic field being equal to zero we obtain the original expression, which was used in the previous discussions.

We will start the description of the magnetic field dependence of I_s by considering a superconducting loop intersected by two tunnelling junctions, i.e. a SQUID as shown in Fig.2.5. If a magnetic field is applied a magnetic flux (Φ) penetrates though the area enclosed by the loop. We assume that the dimensions of the superconductor is larger than $2\lambda_L$. The total supercurrent carried by the device is equal to $I_c^1 \sin(\Delta\varphi_1) + I_c^2 \sin(\Delta\varphi_2)$, where $I_c^{1/2}$ denotes the critical current of JJ number 1, respectively 2, and $\Delta\varphi_{1/2}$ the phase difference across the individual JJs. By integrating the magnetic field over the enclosed area, it follows that [28]

$$\Delta\varphi_1 - \Delta\varphi_2 = \frac{2\pi\Phi}{\Phi_0}\ [mod\ 2\pi].\tag{2.11}$$
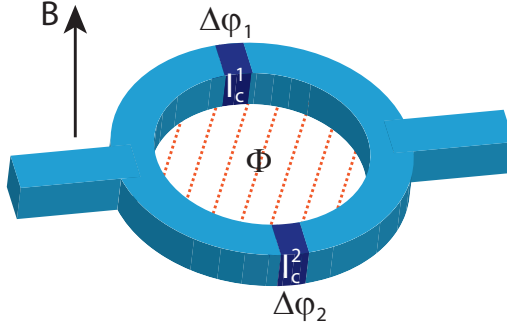
Figure 2.5. Schematic drawing of a SQUID. The superconductor is indicated by light blue and the Josephson junctions by dark blue. If a magnetic field is applied perpendicular to the loop, a magnetic flux is induced in the SQUID's area given by the orange dashed lines.

Therefore the phase difference between the two JJs is given by the induced Φ. The total critical current carried by the device is given by

$$I_c(\Phi) = \max_{\Delta\varphi_1} \left\{ I_c^2 \sin\left(\Delta\varphi_1 - \frac{2\pi\Phi}{\Phi_0}\right) + I_c^1 \sin(\Delta\varphi_1) \right\}. \qquad (2.12)$$

If $I_c^1 = I_c^2$ it follows that $I_c = 2I_c^1 |\cos(\pi\Phi/\Phi_0)|$ as shown by blue in Fig.2.6 b. Note, that if the two junctions are not tunnel junctions, but junctions with high transmission, that the critical current does not reach zero at $\Phi = \Phi_0(j + 1/2)$, where j is an integer number.
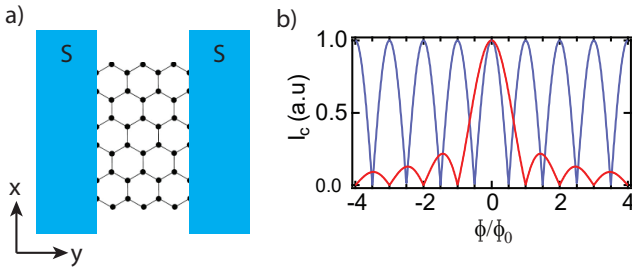
Figure 2.6. a) Schematic drawing of a graphene based JJ. b) Interference pattern for a symmetric SQUID (blue) and a JJ with a constant supercurrent density (red).

With the same principle one can derive the maximum supercurrent that can be carried by a single JJ in a magnetic field. In an extended JJ the current is carried by several trajectories. The critical current density (j_c) is here assumed to be homogeneous along the x-direction (see Fig.2.6 a). Given by Eq.2.11, a phase difference will be induced between two superconducting paths given by the flux enclosed. For a sinusoidal CPR this leads to a dependence of the local supercurrent density, $j_s = j_c \sin(\Delta\varphi(x))$, where $\Delta\varphi(x) = \Delta\varphi(x = 0) + \frac{2\pi\Phi(x)}{\Phi_0}$. Here, $\Phi(x)$ is equal to the product of the magnetic field times the area $S(x) = (L + 2\lambda_L) \times x$. By integrating now the obtained expression over the JJ's width and maximizing the expression for $\Delta\varphi(x = 0)$ one obtains

$$I_c(B) = I_c \left| \frac{\sin(\pi\Phi/\Phi_0)}{\pi\Phi/\Phi_0} \right|, \tag{2.13}$$

the so called Fraunhofer interference pattern. Note, that the obtained result depends on the chosen critical current distribution and CPR. In contrast one would obtain a SQUID-like interference pattern if the supercurrent transported via two channels localized at the edges of the JJ. Therefore, the dependence of I_c in B gives an insight into the supercurrent distribution, which can be calculated from $I_c(B)$ via a Fourier transformation as proposed by Dynes and Fulton [51] and explained in Sec.3.3.3.

All the previous discussion are under the constrain that the voltage across the junction is zero. Some of the effects, when a finite voltage is applied, are described in the following.

ac-Josephson effect

Besides the dc-Josephson effect, Josephson predicted that if a voltage (V) is applied over a Josephson junction the phase difference evolves in time resulting in an ac-supercurrent across the junction. This is called ac-Josephson effect:

$$\frac{d\Delta\varphi}{dt} = \frac{2eV}{\hbar}. \tag{2.14}$$

The oscillation frequency is given by $\nu_J = 2eV/h$, where $2eV$ is the energy change of a Copper pair transported across the junction and h the Plank constant. The tunnelling of a Cooper pair with finite energy can experimentally observed by measuring Shapiro steps or the radiation of a JJ [52, 53]. Another phenomenon called multiple Andreev reflection can be observed in dc measurements of the resistance, which is described in the next section.

Multiple Andreev reflection

Here, we discuss the appearance of multiple Andreev reflections, which arise due to applying a finite voltage V at the JJ. If $eV \geq 2\Delta$ the current is carried

by quasi-particles from one superconductor to the other, because of free states in the DoS_q of the superconductor as shown in Fig.2.7 a. When $eV < 2\Delta$ the quasi-particle's energy is below the gap where the DoS_q is zero, but still a current is observed. Note, that this is not a supercurrent, which appears only at $V = 0$. This phenomenon is explained by multiple Andreev reflections [54]. An electron, which is crossing the junction, gains an energy equal to eV. As explained previously, the electron is then Andreev reflected at the superconducting gap as an hole, which travels the opposite direction and gains again eV in energy. Also the hole undergoes an Andreev reflection, if it does not have enough energy to enter the quasi-particle continuum, and so forth (see Fig.2.7 a). As soon the electron or hole acquired an energy of $neV \geq 2\Delta$, where $(n-1)$ is the number of Andreev reflections, the electron or hole will be transmitted from the normal conductor into the superconductor as a quasi-particle. If now the differential resistance is measured as a function of V one observes decreased values in differential resistance whenever $eV = 2\Delta/n$. This is due to the transmission of a quasi-particle after $(n-1)$ Andreev reflections into the coherence peaks at the gap edge of DoS_q. During the process n charges are transported across the junction and the probability of such a process scales with t^n, which means that the observation of higher order multiple Andreev reflections indicates transparent NS interfaces. From the positions of these dips in bias voltage one can extract Δ as will be discussed in Sec.3.2.2.

As mentioned in the beginning graphene JJ were studied though out this thesis, therefore the next section will give an overview of its intrinsic properties.

2.2. Properties of graphene

Graphene is a 2D material, i.e. one atom thick layer of carbon (C). The C atoms are arranged in a honeycomb lattice (see Fig.2.8 a). The most common isotope in nature is ^{12}C, with six protons and six neutrons in the nucleus. Its proportion is 99%, while the deposit is only 1% for ^{13}C. The six electrons of the C-atom are in the configuration $1s^2 2s^2 2p^2$ for the atomic ground state. The inner shell 1s is close to the nucleus with its two electrons and irrelevant for chemical reactions, whereas the 2s and the 2p orbitals mix in the present of other atoms. In the case of graphene this leads to three valence electrons in the sp^2 orbitals forming σ-bonds to neighbouring C atoms and therefore defining the graphene plane. The fourth valence electron is in the unperturbed p_z orbital, which is perpendicular to the graphene plane and yields a delocalized π-bond.

2.2.1. Band structure of Graphene

In the following we discuss the band structure of graphene at low energy under the scope of a tight-binding approximation, where it is assumed that the atomic
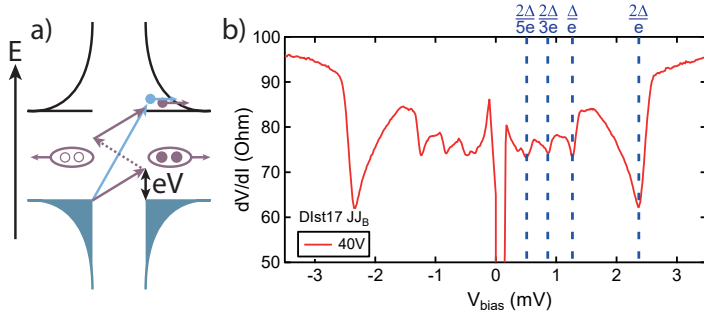
Figure 2.7. a) Schematic drawing of two electron transport processes at finite voltage bias across a JJ. The black lines indicate free quasi-particle states, whereas the dark blue area shows the filled quasi-particle states in the superconductor. The blue arrow corresponds to a transmission of an electron from one superconductor to the other for a bias voltage larger then 2Δ. The purple arrows show a multiple Andreev process when the bias voltage is equal to $2\Delta/3e$. The solid lines correspond to electrons and the dashed ones to holes. During this process three charges (solid circles) are transported via the JJ. b) Differential resistance as a function of voltage bias for a graphene JJ. Dips in the differential resistance are observed at $V_{bias} = 2\Delta/ne$ up to n=5.

orbitals remain intact and the electron wave function of a particular band is given by a linear combinations of degenerate states located on the atoms of the graphene lattice.

Crystal structure of graphene

The unit cell spanned by the basis vectors $\vec{a_1}$ and $\vec{a_2}$ of the graphene crystal lattice contains two carbon atom as shown in Fig.2.8 a. Therefore, graphene can be described as a hexagonal Bravais lattice with two basis atoms (A and B). Here, the basis vectors are chosen as

$$\vec{a}_1 = \frac{a_0}{2}\begin{pmatrix} 3 \\ \sqrt{3} \end{pmatrix} \qquad \text{and} \qquad \vec{a}_2 = \frac{a_0}{2}\begin{pmatrix} 3 \\ -\sqrt{3} \end{pmatrix}, \qquad (2.15)$$

where $a_0 = 1.4\,\text{Å}$ is the inter-atomic distance between the A and B in the basis. Each A atom sits at the sites $\vec{R} = n_1\vec{a_1} + n_2\vec{a_2}$, with n_1 and n_2 being integer numbers. The same is true for the sublattice given by the B atoms, such that $\vec{R}$ is just shifted by $\vec{d_1}$. The positions of the nearest neighbours of an A atom are given by
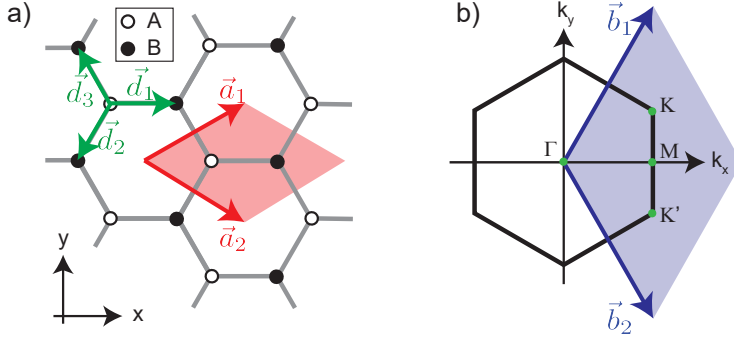
Figure 2.8. a) Schematic drawing of a graphene lattice. The solid (empty) circles correspond to carbon atoms in the B (A) sublattice. The vectors $\vec{d_1}$, $\vec{d_2}$, and $\vec{d_3}$ point to the nearest neighbours in the A sublattice. The unit cell (red area) is spanned by $\vec{a_1}$ and $\vec{a_2}$, which are the unit vectors. b) Schematic drawing of the first Brillouin zone given by the reciprocal lattice vectors $\vec{b_1}$ and $\vec{b_2}$. Two inequivalent points, K and K', exists at the corners of the Brillouin zone corresponding to different valleys. Figure adapted from Ref.[55]

$$\vec{d_1} = a_0 \begin{pmatrix} 1 \\ 0 \end{pmatrix} \quad \text{and} \quad \vec{d_2} = \frac{a_0}{2} \begin{pmatrix} -1 \\ -\sqrt{3} \end{pmatrix} \quad \text{and} \quad \vec{d_3} = \frac{a_0}{2} \begin{pmatrix} -1 \\ \sqrt{3} \end{pmatrix}. \quad (2.16)$$

These three vector as illustrated in Fig.2.8 a point from the A atom at the origin to the three closest B atoms surrounding it.

The reciprocal lattice is spanned by is primitive lattice vectors given as

$$\vec{b_1} = \frac{2\pi}{3a_0} \begin{pmatrix} 1 \\ \sqrt{3} \end{pmatrix} \quad \text{and} \quad \vec{b_2} = \frac{2\pi}{3a_0} \begin{pmatrix} 1 \\ -\sqrt{3} \end{pmatrix}, \quad (2.17)$$

which fulfill the relation $\vec{a_i}\vec{b_j} = 2\pi\delta_{ij}$ by definition. Further they define the Brillouin zone (BZ), which includes a set of inequivalent points, that are not connected by a reciprocal lattice vector. After the definition of the relevant lattice vectors, the electron wavefunction can be written as a linear combinations of the atomic orbitals. A simplified solution can be found by the tight binding approximation.

Tight binding model

In the following section we derive the dispersion relation of graphene using the tight binding model and taking only nearest-neighbour hopping into account.

Higher order contributions like next nearest-neighbour hopping are usually neglected, since they mainly contribute to corrections at high energies. In this model the atoms of the lattice are only weakly interacting, such that the p_z orbital of graphene stays intact. We write then the electron wave function as

$$\psi_k(\vec{r}) = \frac{1}{\sqrt{N}} \sum_{\vec{R}} e^{i\vec{q}\vec{R}}[a\phi_A(\vec{r}) + b\phi_B(\vec{r})], \qquad (2.18)$$

where N is the number of lattice sites, $\vec{q}$ is the wave vector, $\vec{R}$ denote the positions of the A, respectively the B, atoms in the lattice, and a & b are the unknown amplitudes of ϕ_a and ϕ_b. The wave function $\phi_A = \phi(\vec{r} - \vec{R})$ and $\phi_B = \phi(\vec{r} - \vec{R} + \vec{d_1})$ are equal to the wave function ϕ corresponding to the p_z-orbital of sp^2 hybridized carbon atoms at the locations of A and B atoms in the graphene lattice. Note that $\psi(\vec{r})$ fulfills the Bloch theorem. For the crystal lattice of graphene with two basis atoms, we can write the Hamiltonian as

$$H = \frac{\vec{p}^2}{2m_e} + \sum_{\vec{R}}[V_{at}(\vec{r} - \vec{R}) + V_{at}(\vec{r} - \vec{R} + \delta_1)], \qquad (2.19)$$

where $\vec{p}$ is the momentum operator, m_e is the electron mass, and V_{at} the atomic potential. By applying now $\phi_A(\vec{r})$ on the H, we obtain

$$\begin{aligned} H\phi_A(\vec{r}) &= \left[\frac{\vec{p}^2}{2m_e} + V_0(\vec{r})\right]\phi_A(\vec{r}) \\ &+ V_{at}(\vec{r} + \delta_1)\phi_A(\vec{r}) + \sum_{\vec{R}\neq 0}[V_{at}(\vec{r} - \vec{R}) + V_{at}(\vec{r} - \vec{R} + \vec{\delta_1})]\phi_A(\vec{r}) \\ &:= \epsilon\phi_A(\vec{r}) + \Delta V_A\phi_A(\vec{r}). \end{aligned}$$
$$(2.20)$$

Here, ϵ stands for the on-site energy and can be set to zero without loss of generality. The similar result is obtained, when H is applied to $\phi_B(\vec{r})$.

$$\begin{aligned} H\phi_A(\vec{r}) &= \Delta V_A\phi_A(\vec{r}) \\ H\phi_B(\vec{r}) &= \Delta V_B\phi_B(\vec{r}), \end{aligned} \qquad (2.21)$$

where $\Delta V_B = V_{at}(\vec{r}) + \sum_{\vec{R}\neq 0}[V_{at}(\vec{r} - \vec{R}) + V_{at}(\vec{r} - \vec{R} + \vec{\delta_1})]$. To solve now the eigenvalue problem of $H\psi_q(\vec{r}) = E\psi_q(\vec{r})$, we calculate the projection onto $\phi_A(\vec{r})$ and $\phi_B(\vec{r})$. By considering only nearest neighbour hopping, one can rewrite the two obtained equations as shown in Ref.[56] to

$$\begin{pmatrix} \sigma - E & \alpha^*(\vec{q})(\gamma - Es) \\ \alpha(\vec{q})(\gamma - Es) & \sigma - E \end{pmatrix} \begin{pmatrix} a \\ b \end{pmatrix} = \begin{pmatrix} 0 \\ 0 \end{pmatrix} \text{ with}$$

$$\sigma = 3 \int d^3r \phi_A^*(\vec{r}) V_{at}(\vec{r} + \vec{\delta_1}) \phi_A(\vec{r})$$

$$\alpha = 1 + e^{i\vec{q}(\vec{d_2} - \vec{d_3})} + e^{i\vec{q}(\vec{d_1} - \vec{d_3})} \tag{2.22}$$

$$\gamma = \int d^3r \phi_A^*(\vec{r}) V_{at}(\vec{r}) \phi_B(\vec{r})$$

$$s = \int d^3r \phi_A^*(\vec{r}) \phi_B(\vec{r}).$$

The solution for the eigenvalue of the energies are then given by setting the determinate of the matrix in Eq.2.22 to zero. By assuming further that the overlap integral s is small, one obtains the dispersion relation

$$E(\vec{q}) = \sigma \pm \gamma |\alpha(\vec{q})|$$
$$= \sigma \pm \gamma \sqrt{3 + 2\cos[\vec{q}(\vec{d_2} - \vec{d_3})] + 2\cos[\vec{q}(\vec{d_1} - \vec{d_3})] + 2\cos[\vec{q}(\vec{d_1} - \vec{d_2})]}. \tag{2.23}$$

The value of σ is constant and corresponds to a energy shift due to the influence of the neighbouring atoms and can be absorbed by a redefinition of the energy offset. Now we use the definition of $\vec{d_1}$, $\vec{d_2}$, and $\vec{d_3}$ to obtain the final result

$$E(\vec{q}) = \pm\gamma\sqrt{1 + 4\cos[3/2 q_x a_0]\cos[\sqrt{3}/2 q_y a_0] + 4\cos^2[\sqrt{3}/2 q_y a_0]}. \tag{2.24}$$

The dispersion relation $E(\vec{q})$ given by Eq.2.24 is plotted as a function of q_x and q_y in Fig.2.9. The conduction and the valance band touch at zero energy in the K and K' points, the so called Dirac points, which are located at the edge of the BZ. Sometimes graphene is also called a zero band-gap semiconductor, since the conduction and valance band are touching at the K-points, where E_F lies at zero temperature for charge neutral graphene, such that the valence band is fully filled and the conduction band is fully empty. Therefore, this point is also called charge neutrality point (CNP). Further, it reveals a linear dispersion relation at low energies as can be seen in Fig.2.9.

19
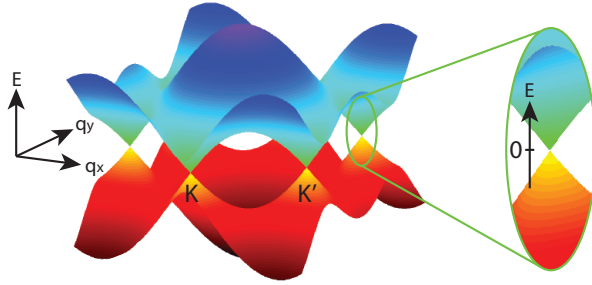
Figure 2.9. Dispersion relation calculated with the tight binding model and nearest neighbour approximation. The conduction and valance band touch at K and K'. On the right side a magnification of the dispersion relation at low energy is shown.

Valleys and linear dispersion relation

As mentioned, the K and K' points are two distinct different points of the reciprocal lattice, since they can not be connected with a reciprocal lattice vector $\vec{G} = n\vec{b_1} + m\vec{b_2}$, where n and m are integer numbers. In general, one refers to this degeneracy as the valley degree of freedom. As we see in Fig.2.9 the dispersion relation around the K-points can be described by a linear relation. This can be seen by Taylor expanding Eq.2.24 and replacing $\vec{q}$ with the quasi momentum $\vec{k}$, where $\vec{q} = \vec{K} + \vec{k}$, one obtains

$$E_{\pm}(\vec{k}) = \pm \hbar v_F |\vec{k}|, \tag{2.25}$$

The plus and minus signs stand for the valence and the conduction band. The DoS in graphene is then given by

$$\text{DoS} = \frac{g_s g_v E}{2\pi (\hbar v_F)^2}, \tag{2.26}$$

where $g_s = 2$ and $g_v = 2$ are the spin and valley degeneracy. The linear relation of the DoS and the energy is a direct consequence of the dispersion relation and the 2D nature of graphene (see Eq.2.25).

Interestingly, the above described bandstructure can change drastically when the graphene is placed on a hexagonal boron-nitride (hBN) substrate by aligning the crystallographic axis of the materials forming a superlattice.

2.3. hBN-graphene moiré superlattice [1]

If graphene is placed in contact with hBN a moiré superlattice can form by aligning their crystallographic axes. This is due to the similarity in the graphene's and hBN's hexagonal lattices and lattice constants (see Fig.2.10 a). This induces a periodic potential of wavelength λ of the order of 10 nm, leading to the modification of the bandstructure of graphene [58] (see Fig.2.10 a). λ defines new Brillouin zone boundaries, where satellite Dirac points (sDPs) may appear [59, 60]. In addition, van Hove singularities (vHSs) emerge in the DoS at saddle points in the bandstructure due to the flattening of the minibands. These vHSs appear at much lower energy than in standard graphene, where they are only reachable by chemical doping [61]. In Ch.4 we will discuss how these vHSs can be probed in long diffusive JJs by measuring R_N and I_c [57]. Because the DoS diverges and charge carriers of different sign coexist, rich physics is expected, such as the formation of charge/spin-density waves [62, 63] or unconventional superconducting pairing mediated by electron-electron interaction [61]. Moreover, the Chern number is predicted to change from subband to subband [64], leading to valley Hall effect and topological edge current when the DoS is gapped at the CNP [65, 66].

2.3.1. Superlattice bandstructure

As mentioned above the additional periodic potential leads to a modification of the graphene's band structure. The band structure of pristine graphene was discussed in Sec.2.2.1. The exact modification of the band structure depends on the interplay of different parameters such as the potential modulation, 2D charge modulation, graphene-hBN hopping and point charge lattice [67]. An example for a possible band structure is shown in Fig.2.10 b. With the change in the band structure also the DoS changes, which is plotted in Fig.2.10 b. A well pronounced vHS and sDP are observed for negative energies. At the vHS as well as at the sDP the charge carrier type in the superlattice changes, which has been shown in a transverse magnetic focusing experiment [68]. As we will discuss in Ch.4, this change of the charge carrier type at the vHS can be observed in Fabry-Pérot resonances in I_c, when the superlattice acts as a ballistic weak link. From the position of the sDP in n one can extract the value of λ and the misalignment angle. The procedure will be discussed in Sec.3.3.2 of this thesis.

Since we studied the electron transport in graphene and hBN-graphene superlattices, some of the important quantities are introduced in the next section.

---

[1]This section is partially adapted from Ref.[57]

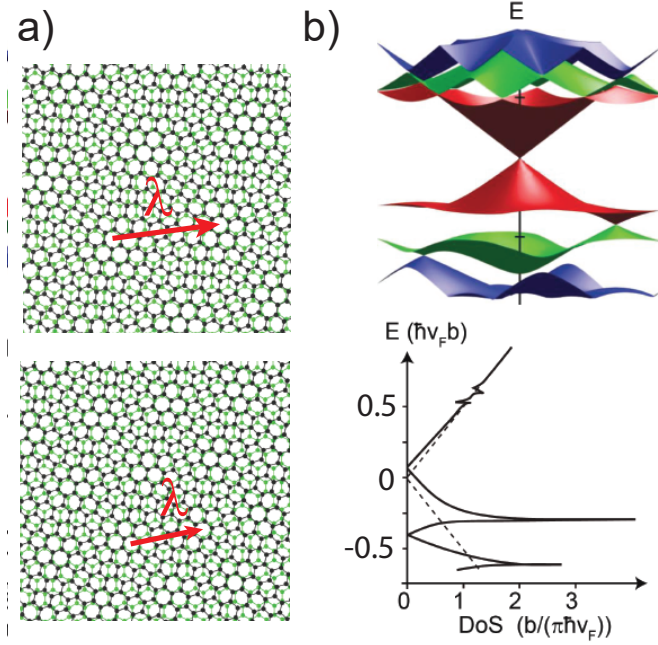**Figure 2.10.** a) hBN-graphene superlattices are sketched with a periodic modulation in the order of the wavelength λ for two different angles. The hBN lattice is shown in green and the graphene lattice in black. b) Numerically calculated moiré minibands (top) and the corresponding DoS (bottom). The dashed lines in the DoS indicate the DoS of pristine graphene. The figure is adapted from [67].

2.3.2. Charge transport in graphene

In the following we discuss the diffusive and ballistic electron transport in the scope of graphene. The relevant scales for the description are the dimensions of the 2D conductor, i.e. the width (W) & length (L), and the mean free path (l_{mfp}), which gives the distance a charge carriers travels before momentum scattering takes place. If $l_{mfp} \ll W, L$ the transport regime is called diffusive, since the charge carriers scatter many times during the transport in the conductor. In the case of $l_{mfp} \gg W, L$ the electrons are carried ballistic, without any scattering events across the junction and keep their original momentum.

Diffusive transport, Drude model and Einstein relation

In the diffusive regime the conductivity (σ) given by the Drude model can be expressed as,

$$\sigma = \frac{ne^2\tau}{m_e}, \tag{2.27}$$

where τ is the average scattering time and n the electron density per unit area. This equation can be derived from the assumption, that two forces act on the free electrons in a conductor. These are on one hand an applied electric field and on the other the scattering of electrons in the material by phonons, charged impurities and random strain fluctuations [69–74]. The mobility of the charge carriers is then defined by $\mu = e\tau/m_e$. Therefore the conductivity can be expressed as

$$\sigma = ne\mu. \tag{2.28}$$

Experimentally, the mobility can be extracted by measuring the conductivity as a function of n. In the case of a two terminal junction a contact resistance (R_c) has to be added in series with the device resistance. This additional resistance leads to a saturation of the device's conductivity at large doping. To obtain a value for μ and R_c assuming them to be constant in n the conductivity can be fitted by

$$\sigma^{-1} = \frac{1}{en\mu + \sigma_0} + \rho_c, \tag{2.29}$$

where σ_0 is the residual conductivity at the CNP and ρ_c the contact resistivity. An example is shown in Fig.2.11.

An other important relation for diffusive transport is the Einstein relation. This relation describes the connection between the diffusion constant D, σ and the DoS. This relation is a consequence from the cancellation of the drift current given by an electric field and the diffusion current coming from a difference in n in thermodynamic equilibrium, when the electro-chemical potential is equal to zero. One can write

$$\sigma = e^2 \, \mathrm{DoS}(E_F) D, \tag{2.30}$$

23
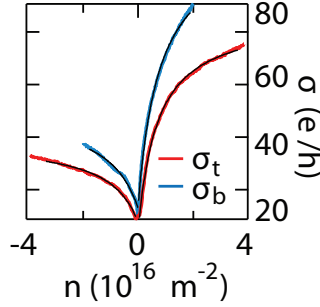
Figure 2.11. Conductivity as a function of charge carrier density for two different two-terminal graphene junctions (red and blue). The black lines correspond to a fit with Eq.2.29.

where $D = \frac{1}{2}v_F^2\tau$ for a two dimensional conductor [56]. In the following we switch to the case of ballistic electron transport and will discuss certain phase coherent transport effects in more detail.

Ballistic transport

As mentioned above, the device enters the ballistic regime when l_{mfp} exceeds the length and the width of the transport channel. In this case scattering takes only place at the contacts and the sample edges, which is distinctly different form the diffusive transport described above. For a ballistic graphene junction every mode carries, due to the valley and spin degeneracy, a conductance (G) of $4e^2/h$. Whereas the number of modes is given by the width of the junction and the Fermi wavelength ($\lambda_F = 2\pi/k_F$) as shown in Eq.2.31.

$$G = \frac{4e^2}{h}\frac{W}{\lambda_F/2} = \frac{4e^2}{h}W\sqrt{n/\pi} \qquad (2.31)$$

Quantized conductance has been shown for ballistic graphene devices with a narrow constriction [75, 76] or for gate defined quantum point contacts in bilayer graphene [77]. In the following we will discuss another phenomenon, which appears due to phase coherent, ballistic transport, namely Fabry-Pérot oscillations.

Fabry-Pérot oscillations

Similar as in optics, Fabry-Pérot (FP) interferometers can be build out of graphene, but instead of light, the electrons interfere. A cavity can be induced

by varying doping within the graphene layers using multiple electrostatic gates [78, 79]. In the bipolar regime, when one region is hole (p) doped and another electron (n) doped, the interface of the pn-junction acts like a partially transparent mirror meaning that electrons can be transmitted or reflected with a certain probability. This probability depends on the angle (θ) of the incident electron and shows a dependence proportional to $\cos^2(\theta)$ for a step like potential [80]. At zero angle the transmission is perfect, which is known as Klein tunnelling [81, 82]. Therefore, a FP cavity can be created in graphene by using two pn-junctions. In such pnp-doped and npn-doped graphene clear signs of FP oscillation were observed manifested in an oscillation of the junction resistance as a function of electron density [79]. Note, that besides electrostatically defined pn-junctions also contact doping can lead to the formation of FP cavity [83–86].

An example of FP resonances in graphene is shown in Fig.2.12. The graphene was contacted by normal metal. The electron density in the outer regions (n_{out}) and the inner region (n_{in}), which is cover by the top gate, could be adjusted separately to form a bipolar FP cavity ($n_{in} > 0$ and $n_{out} < 0$) using a global back gate and a local top gate. An additional oscillation was observed in the unipolar regime when both regions were p-doped due to pn-junctions at the contacts arising because of the contact doping.

An important condition to observe FP oscillation is that the phase coherence length (l_ϕ) is larger than the sample dimensions L and W. If the electrons travel from one contact to the other, their wave functions pick-up a phase given by $\phi = k_F L$. Therefore, the phase difference between different trajectories can be expressed as $\Delta\phi = k_F(L_1 - L_2)$, where L_1 and L_2 are the length of the first and second trajectory, respectively. In the simplest case one can assume for ballistic transport and small angles such that the electron's path, which is reflected once back and forth, differs by $2L$. For constructive interference $\Delta\phi$ has to be equal to 2π, which leads to the condition that

$$k_F 2L = 2\pi \ [mod \ 2\pi]. \tag{2.32}$$

In graphene the wave vector at the Fermi energy is given by $\sqrt{\pi n}$. Therefore, the resonance condition depends directly on the electron density and a increased conductance is observed whenever $\sqrt{\pi n}L = \pi \ [mod \ 2\pi]$. It is possible to extract the cavity length from the position of the maxima in conductance by

$$L = \frac{\sqrt{\pi}}{\sqrt{n_{i+1}} - \sqrt{n_i}}, \tag{2.33}$$

where n_i denotes the position of the ith maxima in n.

In the next section we turn towards the transport behavior in a 2D material at large out-of-plane mangetic fields and discuss the quantum Hall effect discovered by Klitzing et al. in 1980 [87].

25

2. Theoretical background
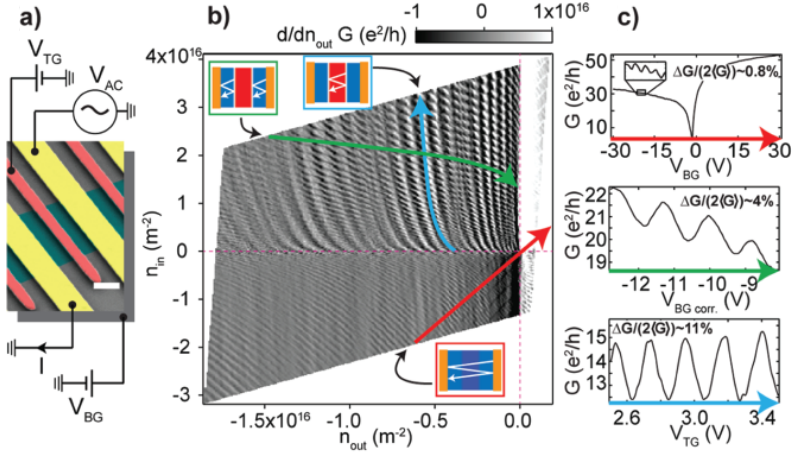
Figure 2.12. a) A false colored SEM image of the device. Yellow indicates the normal metal contacts, red the local top gates and cyan the graphene encapsulated in hBN. The white scale bar is equal to 500 nm. b) Numerical derivative with respect to n_{in} of the conductance as a function of n_{in}, the electron density in the top gate covered graphene, the electron density in the top gate uncovered graphene and n_{out}. The arrows show the densities dependence of the oscillations in different electrostatic and contact doping created FP cavities, which are sketched in the insets. c) Conductance as a function of gate voltage along the red, blue and green arrow in b). This figure is adapted from Ref.[83].

2.3.3. Quantum Hall effect in graphene

When electrons are moving through a magnetic field, they experience a deflection from their straight trajectory due to the Lorenz force. It was found, that this leads to the Hall voltage (U_H), which appears in the direction perpendicular to the magnetic field and the current flow.

$$U_H = R_H B I, \tag{2.34}$$

where R_H is the Hall coefficient, B the magnetic field, and I the current. Therefore, U_H/I is proportional in B, while the longitudinal voltage does not show any magnetic field dependence for small values of B. Using the Drude model, one can derive [56], that R_H for a 2D conductor as graphene is related to n by

$$R_H^{2D} = \frac{1}{en}. \tag{2.35}$$

When the magnetic field is increased the states become quantized in high mobility 2D conductors due to the cyclotron motions of the electrons in closed loops as soon $\omega_c \tau > 1$, where $\omega_c = \frac{eB}{m_e}$ is the cyclotron frequency. If the phase picked up during one cycle is equal to 2π the particle interferes with it self constructively, which leads to a quantization of the energy spectrum. In this, so called quantum Hall state, the states in the bulk of the conductor are localized and the bulk is gapped, while a discrete numbers of edge channels are carrying the dissipationless current. In this regime the longitudinal resistance R_{xx} vanishes, whereas $R_H = R_{xy} = h/(e^2\nu)$ shows a quantized behavior with $\nu = 1, 2, 3, ...$, which is called the filling factor. The filling factor is given by n/n_L, where $n_L = eB/h$ is the number of allowed states per unit area. Further one refers to the value of h/e^2 as the resistance quantum.

The energies of the quantized states in graphene can be calculated by finding the Hamiltonian's eigenvalues and eigenstates of graphene in a perpendicular magnetic field. These states are called Landau levels (LL) with

$$E_N = \text{sgn}(N)v_F\sqrt{2e\hbar B|N|}, \tag{2.36}$$

where N is an integer number. Each of these states is fourfold degenerate due to valley and spin. As a consequence one observes quantized conductance at low temperatures, namely when the thermal broadening of the states given by $k_B T$, with k_B the Boltzmann constant and T the temperature, is smaller than the LL gap ($\omega_c \tau \gg 1$ as mentioned above). From Eq.2.36 one can see that a LL at zero energy exists, which is a consequence of the graphene's band structure. Half of its states belong to the conduction band and half to the valence band, respectively. This means, when starting from zero energy, that the first plateau in conductnce is observed as soon as $2n_L$ electrons are in the conduction band. This leads to the half integer quantum Hall effect and to conduction plateaus of

$$\sigma_{xy} = \frac{4e^2}{h}\left(i + \frac{1}{2}\right), \tag{2.37}$$

with i an integer number. While the Hall conduction is constant, the value of R_{xx} goes to zero and appears only during the transition from one LL to another, i.e. when the bulk is not gapped.

In a two terminal device the R_{xy} and R_{xx} can not be measured separately. Depending on the aspect ratio one observes an oscillation behavior of the resistance. Plateaus are only expected for a junction width to length ratio of around $L/W \approx 1$ [88].

In the following section we will focus on the 0th LL and its possible ground states. Especially, the case of a helical QH ground state will be discussed and how it was realized in various expermiments.

Helical edge states in graphene

At high magnetic fields a lifting of the LL's degeneracies was observed [89, 90], which is attributed to exchange interactions [91–93] that lead to valley and spin polarized LLs. The order of the LLs is then determined by the influence of the interactions on the spin and valley degeneracy. As mentioned before the 0th LL has electron and hole like states. When the valley splitting is larger than the Zeeman energy [90, 93, 94] the electron like states are hosted by one valley and the hole like by the other valley [95], which opens a gap at charge neutrality. A schematic drawing of this situation is shown in Fig.2.13 a. While valley polarization is linked to the charge carrier type, each valley hosts a spin-up and spin-down state. If instead the Zeeman energy dominates, it is possible to change the ground state. This results on one side in a conductance of $2e^2/h$, due to counter propagating edge channels and on the other hands in a ferromagnetic ordering in the bulk of the graphene [91, 96, 97]. Note, that the counter propagating edge states form a 1D helical state given by their opposite spin polarization.
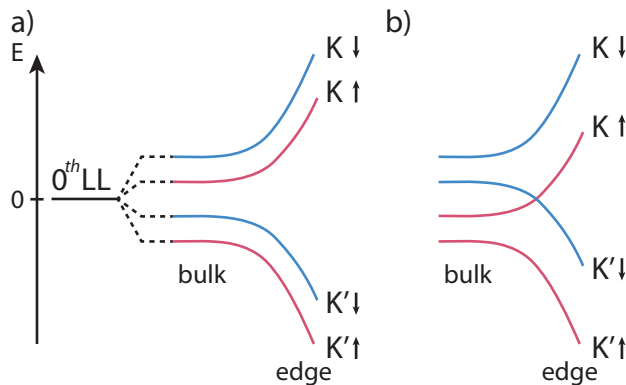
Figure 2.13. a) Schematic drawing of the lifting of the 0th LL degeneracy. The states in the K' valley are hole like and the one in the K valley electron like. The red and blue color indicate spin-up and spin-down polarized bands. b) Schematic drawing of the LL ordering if the Zeeman energy exceeds the valley splitting. In this case the edge conducts and the bulk has a ferromagnetic ordering.

Regarding this phenomena, the 0th LL attracted great interest due to the proposition of creating Majorana zero modes, when graphene is in electrical contact with a superconductor, while it is gapped and hosts a helical QH state [100]. The helical QH state at $\nu = 0$ has been experimentally observed in large
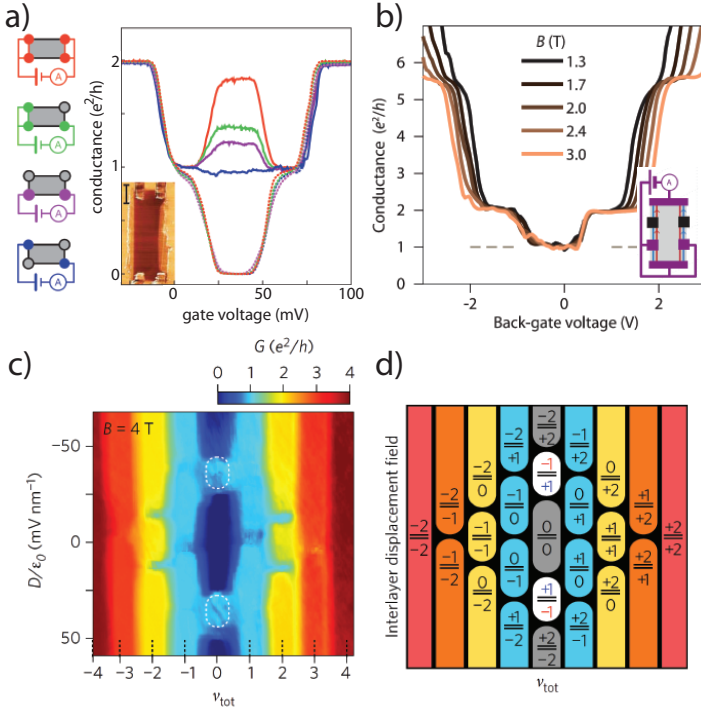
Figure 2.14. a) Observation of helical QH state in large magnetic fields. Left: Schematic diagram of four distinct two-terminal measurement topologies available in a four-terminal device. Open circles indicate floating contacts whereas filled, coloured circles indicate measurement contacts. Each variation probes two parallel conductance paths between the measurement contact with a variable number of segments on each path, indicated by black edges. Right: Two-terminal conductance measurements , colour-coded to match the four different measurement configurations. Dashed curves correspond to an applied out-of-plane magnetic field of $1.4\,\mathrm{T}$ and solid curves to magnetic field in-plane of $34.5\,\mathrm{T}$ with an out-of-plane component of $1.4\,\mathrm{T}$. Inset: Atomic microscope picture of the device. The scale bar is equal to $1\,\mu\mathrm{m}$. This figure is adapted from Ref.[97]. b) Two terminal conductance as a function of back gate voltage at different magnetic fields for graphene placed in proximity with $SrTiO_3$. The first conductance plateaus of the quantum Hall effect at $2e^2/h$ and $6e^2/h$ are well defined. The helical quantum Hall plateau of conductance e^2/h clearly emerges at the charge neutrality point ($V_{bg} = 0\,V$) for the measurement configuration shown in the inset. This figure is adapted from Ref. [98]. c) Two-terminal conductance as a function of ν_{tot} and displacement field D for a large angle twisted bilayer graphene. The conductance is given by $\nu_{tot} \times e^2/h$ for all configurations except for $(\pm1, \mp1)$ state, indicated by the dashed white circles. d) Schematic map of possible filling factor combinations. The figures c) & d) are adapted from Ref.[99].

in-plane magnetic fields of about $30\,\mathrm{T}$ [97] (see Fig.2.14 a), when the Zeeman energy exceeded the valley splitting as shown in Fig.2.13 b.

A different route to establish a ferromagnetic ground state is to screen the long-range Coulomb interaction in the graphene, which was realized by using a $SrTiO_3$ substrate. This substrate has a large dielectric constant at low temperatures. When the graphene is brought in close proximity with it, i.e. below the magnetic length $l_B = \sqrt{\hbar/eB}$, long-range interactions are screened and a helical ground state establishes as shown in Fig.2.14 b [98].
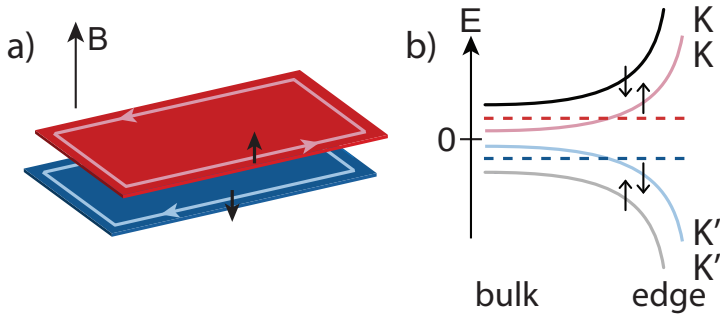
Figure 2.15. a) Schematic drawing of two decoupled graphene layer at large out of plane magnetic field hosting each one QH edge channel. The top (red) layer's chemical potential is set to $\nu = 1$, while the bottom (blue) layer is set to $\nu = -1$. The edge states are counter-propagating and have opposite spin polarization. b) Schematic drawing of the valley and spin degeneracy lifted 0th LL. The chemical potential of the top layer (red dashed line) is placed to be at $\nu = 1$ and the chemical potential of the bottom one (blue dashed line) to $\nu = -1$. Since the electro-chemical potential will be the same for both layers the red and the blue solid line will cross in energy at the edges.

In this thesis we will discuss in more detail a third way to realize helical states in graphene, which uses two decoupled graphene layers tuned to opposite filling factors of $\nu = \pm 1$. It has been shown by Sanchez-Yamagishi et al. [99], that the QH state assigned to $\nu = -1$ in one and $\nu = 1$ in the other graphene layer form a helical state. This state was engineered by stacking two graphene layers with a large twist angle together, which decouples the two graphene layers, due to a large momentum mismatch. The electron densities of the individual layers can be controlled by two gates, namely a global top and a global bottom gate. This makes it possible to tune the layers independently to different filling factors within the 0th LL. At opposite sign but same magnitude of the filling factor. It was observed that a conductance plateau establishes with a conductance value between 1 and 2 e^2/h for $\nu = \pm 1$ and ∓ 1, whereas the conductance vanishes

for other values of the filling factors (see Fig.2.14 c). This was attributed to the fact, that the states assigned to $\nu = \pm 1$ are spin polarized with opposite spins, which prohibits backscattering from one QH edge state to the other. Since the decoupling is not perfect due to the direct contact of the two layers, one still observes backscattering for higher magnitudes of ν, when a counter flowing channel with the same spin is available in the other graphene layer leading to insulating states.

We applied the same principle to engineer a helical quantum Hall (hQH) states in a double layer graphene heterostructure, where the graphene layers are decoupled by a thin hBN spacer inserted between the layers [101]. In contrast to previous works, the graphene layers are fully electrically decoupled in the bulk and the edges, while they are shorted at the contacts. By tuning the chemical potential individually to different filling factors one observes therefore every combinations of conductance plateaus, since backscattering from one to the other layer is absent, as will be discussed in Ch.5 of this thesis. Still the full lifting of the degeneracy in clean devices leads to the formation of helical states at $\nu = \pm 1$ (Fig.2.15 a) when the chemical potentials are set as shown in Fig.2.15 b.

Coupling of these helical QH states ot a superconductor could lead to the formation of Majorana zero modes in graphene, as proposed by San-Jose et al. [100]. In the past several experiments were carried out to investigate the coupling of the QH edge channels to superconducting electrodes. In the next section an overview of the latest study is given.

2.4. Superconducting correlations in the quantum Hall regime

A key ingredient towards Majorana zero modes in graphene is the coupling of the helical edges states, which were discuss in Sec.2.3.3, by a superconductor. This would couple a forward moving electron in one channel to a hole moving backwards in the other by Andreev reflection within the layer or crossed Andreev reflection between the layers. Majorana zero modes similar to the ones in 1D semiconducting nanowires are then expected [102–105]. Superconducting correlations in the QH regime were observed in various graphene based structures, which will be discussed in the following section and the coupling has to be carried by a hybrid electron-hole state long the superconductor.

2.4.1. Observation of superconducting correlations

Recently it was observed by Lee et al.[106], that a superconducting correlation can be induced in the QH edge states of graphene. The device, which was fabricated for this experiment is shown in Fig.2.16 a. It is a Hall bar with several normal metal contacts and one narrow superconducting contact extending into the Hall bar. The width of the superconducting electrode made

of NbN is kept smaller than the its coherence length, such that the counter propagating QH states along the electrode can be coupled by crossed Andreev reflection. By measuring the downstream resistance (R_D) between the super-conductor and a normal electrode at the bottom edge, a negative resistance value was detected for $\nu = 1$ and 2 at low temperatures (see Fig.2.16 b). This negative resistance is attributed to a conversion of an incoming electron into a outgoing hole at the superconductor-graphene interface and demonstrates the possibility of coupling QH edge channels in graphene by a superconductor.
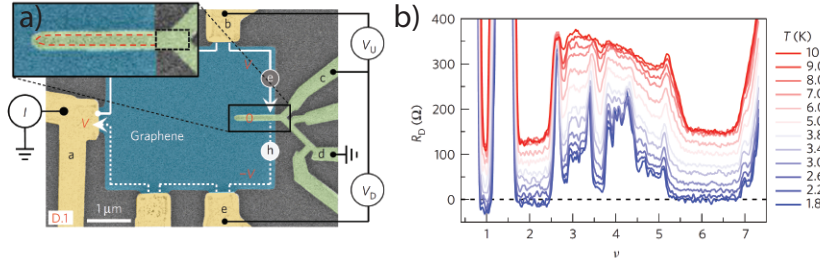
Figure 2.16. a) False color SEM image of the device with the measurement configuration. Ti/Au electrodes are indicated by yellow, the superconducting electrode made of NbN in green and the graphene in blue. The inset show the 1D NbN side contact, which has a width of approximately 50 nm. V_u is the upstream chemical potential; V_D the downstream chemical potential and I the current. b) Filling factor dependence of the downstream resistance (R_D) at different temperatures with $B = 14$ T. The figure is adapted from Ref.[106].

2.4.2. Reduced resistance of graphene JJ in the QH regime

It was reported by Refs.[107, 108], that so called superconducting pockets randomly appear as a function of gate voltage and magnetic field in the QH regime for graphene based JJs. These pockets manifest themselves as reduced resistance at zero bias current (see Fig.2.17 a & b). Note, that no helical states are expected for graphene on a SiO_2/hBN substrate at several Teslas [99]. Due to the chirality of the edge states the Andreev reflected hole has to be carried by the opposite edge given by the propagation direction of the edge states. Since the Andreev reflection takes place within ξ_s, the direct Andreev reflection is not possible.

Device geometry

To exclude bulk contributions and show that both edges are involved in observation of superconducting pockets, further investigations towards the enlightenment of the nature of this novel Andreev process were done by Finkelstein et al. The strength of the superconducting effect in the QH regime was studied in dependence of the length and width of the JJ. While a dependence was observed with the length of the junction, namely a disappearance of the superconducting pockets when L exceeds $2\,\mu$m [109], a change of the junction's width seems to have no influence, even when the graphene channel was etched down to 30-40 nm [109, 110], where one would expect a stronger coupling of the edges due to the similar order of magntiude of the width compared to the coherence length of the superconductor. Further, it was found that the JJ do not carry any supercurrent if one edge is extended out of the region of the superconducting contacts, which lead to the conclusion that both edges has to be involved in the Andreev process. This points in the direction that the perimeter of the device plays a significant role for the strength of the supercurrent and the placement of the superconducting electrodes is irrelevant as proposed by Refs.[111–113]. Recently, it has been shown by Seredinski et al. [114] that supercurrent can be induced at each edge of JJs individually using a side gate to control the filling factor at the edges, which can be different from the bulk. In this case the Andreev reflected hole can be carried by the counter propagating state at the same edge, which leads as well to superconducting pockets in the QH regime. This results differs from the previous ones, since the Andreev reflection can take place within the coherence length of the superconductor and does not need a coupling of the Andreev pair at opposite edges.

Hybrid electron-hole state

As mentioned, the coupling of the edges is attributed to a hybrid electron-hole state arising from several Andreev reflections at the contact, which mediates the hole to the other side of the junction as pictured in Fig.2.17 c. The existence of this state was shown by Refs. [115, 116]. In their experiment they measured the non-local voltage in a three terminal measurement, for which they observe positive and negative voltages attributed to the probability to inject a hole or an electron in the edge states at the end of the superconductor.

Interference of the superconducting pockets

Surprisingly, the interference pattern in magnetic field of the supercurrent in the QH regime, showed the same $h/2e$ periodicity as the Fraunhofer pattern at small magnetic fields [108]. This points rather in the direction of supercurrent flowing at both edges individually, which interfere. Because, a h/e periodic

2
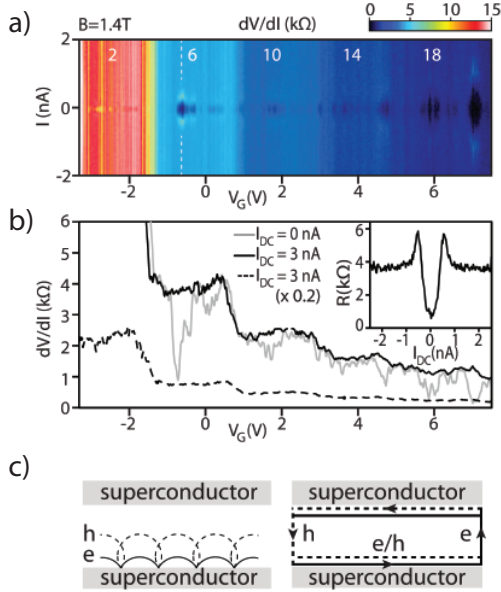
Figure 2.17. a) Differential resistance dV/dI measured at 45 mK as a function of bias current I and gate voltage V_G at constant $B = 1.4$ T. Filling factors are indicated in bold white font on top of the map. QH plateaus are clearly visible as stripes of different colors around filling factors $\nu=4(n+1/2)$ with integer n. Pockets of superconductivity appear as dark regions close to zero current. b) Line cuts of dV/dI, measured in the same range of V_G at zero DC current (gray) and 3 nA (black). The dashed curve is obtained by scaling the black curve by a factor 0.2 to demonstrate the $\nu =2$ plateau. Inset: dV/dI versus I for a prominent superconducting pocket, which is indicated in a) by a vertical dashed line. c) Right: Schematics of the Andreev bound states, made of counter propagating electron and hole states on the opposite sides of the sample, which couple through the hybrid electron-hole modes running along the superconductor-QH interfaces. Left: these chiral hybrid modes are made of electron and hole edge states mixed through the Andreev processes [108].

modulation would be expected, if the hole is indeed reflected into the other edge [117–119]. Therefore, the observations are sill not conclusive and need further investigations. Instead of narrow tranches to increase the coupling of the edges, one can use a double layer graphene structure, in which the two graphene layers are separated by a hBN thinner than ξ_s. It has been recently shown in a double bilayer graphene system that crossed Andreev reflections take place [120]. By inducing opposite charge carriers in the graphene layers the edge channels on the same edge counter propagate in the different layers and could be couple directly by a crossed Andreev process, such no hybrid electron-hole like state is needed. This may increase the coupling and leads to supercurrent in the QH regime due to the direct coupling of the edge channels.

2

3 Device Fabrication and Experimental Methods
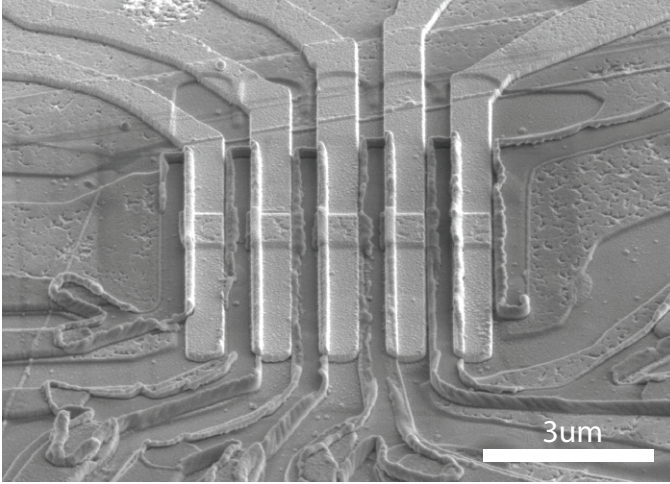
In the following chapter the basics of the device fabrication and data treatment are described. It starts from the ex-foliation of the different 2D materials and the stacking of van der Waals heterostructures and ranges to the establishment of superconducting contacts to graphene. Then, the basic properties of graphene Josephson junction with molybdenum-rhenium side-contacts are summarized. We describe different methods, which were applied through out the thesis, for the data processing, e.g. electrostatic models. In the end the measurement of the critical current using a counter is described in detail.

3.1. Fabrication of van der Waals heterostructures

The assembly of so called van der Waals heterostrucures (vdWh), which consist of layers of different 2D crystals, is the basic fabrication step for all devices discussed in this thesis. The variety of 2D materials is huge and expands from insulating materials like hBN to 2D superconductors such as $NbSe_2$ [15], from WTe_2 a topological insulator [12–14] to graphene a zero-band gap semiconductor [6]. The combination of crystals with different electronic and physical properties can be used to engineer new materials with their own intrinsic and novel features [17–20, 22–25, 121–123]. In this section we describe the principle of extracting and stacking 2D materials into wdWh.

3.1.1. Exfoliation

Thin crystals even down to an atomic level, e.g. graphene, can be extracted from their bulk material using mechanical exfoliation [6]. This method is based on the cleaving of a bulk crystal, e.g. graphite, along single crystal planes. Therefore, the vdW interaction between two layers has to be overcome by the applied mechanical force to separate the planes. To obtain single layers and thin flakes we proceeded as described in the following.

In a first step the bulk crystal is placed on the tape and pressed down until it is well in contact. Then the crystal is removed and thick pieces remain on the tape as shown in Fig.3.1 a. By folding and unfolding the tape several times the crystals are cleaved and their thickness is reduced. This step is repeated 4-10 times until a homogeneous coverage is obtained (see Fig.3.1 b). With a new strip of tape, we create a copy of the first tape. In the ideal case all the crystals cleave again, such that their surfaces are clean, since they were never in contact with the exfoliation tape. In the end the copy tape is cut into pieces and brought in contact with a silicon wafer as can be seen in Fig.3.1 c. This wafer is covered with silicon oxide, which thickness was optimized for the optical contrast of the different materials [65, 124]. Then the tape is removed, which cleaves the crystals again and leave back flakes of different thicknesses on the silicon oxide. The monolayer graphene can then be identified by its contrast of 4% in the green channel of an optical image. Further informations about the used tape and the crystal sources are given in App.A.

3.1.2. Stacking of vdW heterostructures

In this section we describe the fabrication of vdW heterostructures consisting out of layers of different materials. It has been shown, that the encapsulation of graphene in various materials enhances its electronic quality [22, 125] and further that the close proximity to other crystals influences its intrinsic properties like inducing spin-orbit coupling [19, 20, 121, 123, 126] or exchange

Figure 3.1. a) Bulk material is placed on the low adhesion tape and is cleaved for the first time. b) The bulk crystal is cleaved several times, which covers the tape homogeneously by thin flakes. c) The thinned down crystal is brought in contact with a silicon wafer, which leaves back crystals of various thicknesses.

3

interactions [17, 18]. Not only the stacking order of the different layers matter, but also the alignment of the crystal axes of the materials. For different angles between different materials and graphene it was reported that the band structure changes drastically [23, 127, 128].

In this thesis we will discuss vdWh made from hBN and graphite, respectively graphene. In the following, the stacking process is described, where we followed the recipe of Wang et al. [125] and Zomer et al. [129]. Further, the procedure for fabricating twisted graphene structures is summarized [25, 127, 130].

Preparing of the stamp

To pick up the different vdW materials a stamp is used, which consists out of a thin (1-3 mm) PDMS pillow covered with a polycarbonate (PC) film. While the glass slide is used as a carrier for the PDMS/PC pillow and to mount the stamp into transfer setup, the PC with its strong adhesion is used to pick up the different 2D materials from the silicon oxide covered wafer.

The PDMS/PC pillow is fabricated as now described. A solution of PC is applied on a glass slide (see App.A), which is then partially removed with an adhesive tape having a window in its center as shown in Fig.3.2 a. The PC film, which is suspended in the window, is placed in contact with the PDMS pillow (Fig.3.2 b) and fixed with additional tape at the edges. The stamp is now mounted in to the transfer set-up, which has movable stage in xyz, that can be heated up to 180 °C.

Pick-up procedure

As shown in Fig.3.2 c, the substrate with the crystal is placed below the PDMS/PC pillow. After identifying a clean area of the PC interface, it is brought in contact with the desired crystal, here hBN. It will be picked-up by a thermal cycle. The details of the procedure are sketched in Fig.3.2 d1 to d3.

To describe this procedure we start from the situation, where a hBN flake is already attached to the PC film and a graphene flake has to be picked up in the next step. The hBN is aligned optically with the graphene on the silicon wafer. The PC is brought in contact with the silicon substrate at 40 °C, but such that the flakes do not touch yet. Then, the stage is heated to 80-90 °C. This leads to a thermal expansion of the PDMS such that the PC interface starts to move towards the graphene (see Fig.3.2 d1) and the hBN goes slowly in contact with it. The flakes are kept in contact for ∼5 min at 80 °. By setting the temperature back to 40 ° the PDMS contracts and the PC interface moves again over the location of the graphene flake (see Fig.3.2 d2), which is picked-up due to the vdW forces, respectively due to the adhesion of the PC, which is stronger than the adhesion to the SiO_2 (see Fig.3.2 d3). This procedure is repeated for every layer of the heterostructure.

Deposition of the stack

If the assembly of the heterostructure is completed, it has to be placed on the desired substrate. To do so we adapted a procedure proposed by Purdie et al. [131]. Before the stamp is in contact with the substrate, the later is heated to 160 °C. While lowering the stamp, the PC interface get in contact with the substrate and will move again due to the thermal expansion of the PDMS, which brings the heterostructure into contact with the substrate. Because of the high temperature enclosed dirt between different layers of the heterostructure can move and is pushed at the edges of the stack while the PC interface creeps over the vdWh. This leads to large flat and clean areas. As soon as the entire stack is in contact with the substrate, we heat the stage to 180 °C. The PC tears off at the edges of the PDMS and detaches from it, such that the PC covers the stack on the substrate. After removing the glass slide with the PDMS, the substrate is backed for another 5 min at 180 °C to relax potential stress in the PC film. It was observed, that stacks were lifted off the substrate during the removal of the PC, if the additional backing was not done.

Removal of PC and annealing

The PC was dissolve in dichlormethane for 1 h. To remove remaining polymer residues, the stacks were annealed in forming gas at 300°C. The recipe is given in App.A.1.2.

3.1.3. Fabrication of twisted bilayer graphene

Twisted bilayer graphene (tBLG) are two layers of graphene in contact with each other under a certain misalignment of their crystallographic axes given by the twist angle. To control this angle during the stacking process we followed
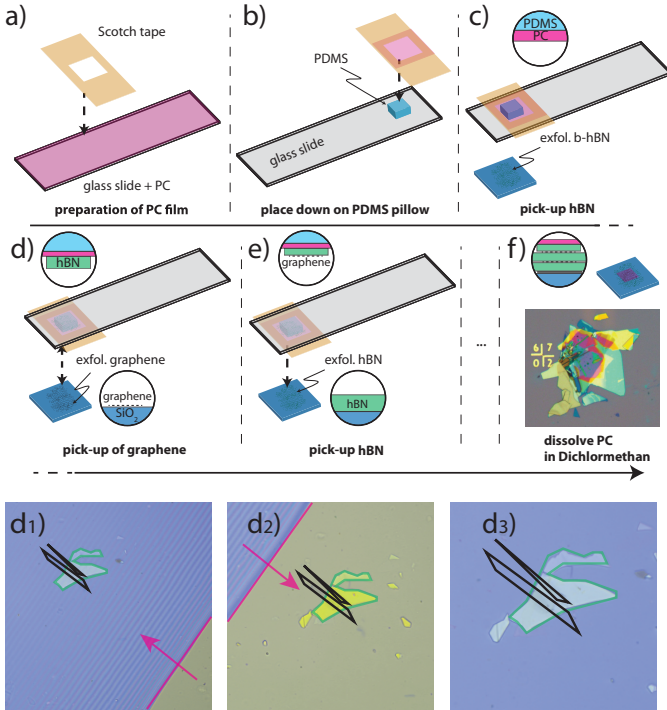
Figure 3.2. a) PC film (pink) on a glass slide, which is locally lift-off by an adhesive tape. b) The suspended PC film is placed on a PDMS pillow (blue). c) Set-up before picking-up the first hBN layer. d) Set-up to pick-up graphene: d1)-d3) microscope images of the pick-up process. The graphene is shown in black, the hBN in green. The light brown (light blue) area corresponds to the regions, where the PC is in contact (out of contact) with the silicon wafer. e) Set-up before picking-up an additional hBN layer. f) Finalised stack, which is placed on the substrate. This figure was adapted from [55]

the ansatz from Rickhaus et al.[130]. The idea is to fabricate the tBLG from the same graphene flake by tearing it apart and stack the two pieces together. Since the two pieces have *a priori* the same orientation of the crystal axis, the twist angle can be controlled by a rotation of the transfer stage between the pick up of the individual pieces.

Tearing graphene

To tear the graphene the PDMS/PC stamp is prepared as describe in the previous section. After a hBN was picked-up, the stage temperature is set to 30° and the substrate with the graphene is placed below the stamp. Now the PC is brought in contact with the substrate, until the hBN covers the half of the graphene flake. The movement of the PC is stopped at the hBN edge as shown in Fig.3.3 a & b. If done like this, the transfer remains polymer free since the neither half of the graphene layer gets in contact with the PC, which protects them from contaminations. Now the stage is heated to 40 °C. The stamp has to be continuously lifted to keep the PC interface in place, because of the thermal expansion of the PDMS. As soon as the temperature is reached, the stamp is fully retracted and the graphene tears apart. This is schematically shown in Fig.3.3 c. Now the stage can be rotated by the desired angle and the second half of the graphene can be picked-up as described in Sec.3.1.2.

With these different procedure we realized the vdW heterostructures, which build the bases of the studies discussed in this thesis. The electronic devices were then further completed by electron lithography defined electrodes of normal metal or superconductor and placing different gate structures. The details of the fabrication are summarized in the App.A.

3.2. 1D MoRe contacts

One key element of this thesis are the one-dimensional superconducting side contacts out of MoRe, which were used to fabricate graphene based Josephson junctions. Here, we summarize the basic properties of a superconducting MoRe film, like critical temperature (T_c), critical magnetic field (B_c), the kinetic inductance (L_k), and the London penetration depth (λ_L). Further we give an overview of some basic properties of graphene base Josephson junction with MoRe electrodes.

3.2.1. Fabrication of MoRe thin films

Before we start with the physical properties of superconducting MoRe thin films, the fabrication of those is briefly described. The shape and the dimensions were controlled by standard electron beam lithography. PMMA 950k
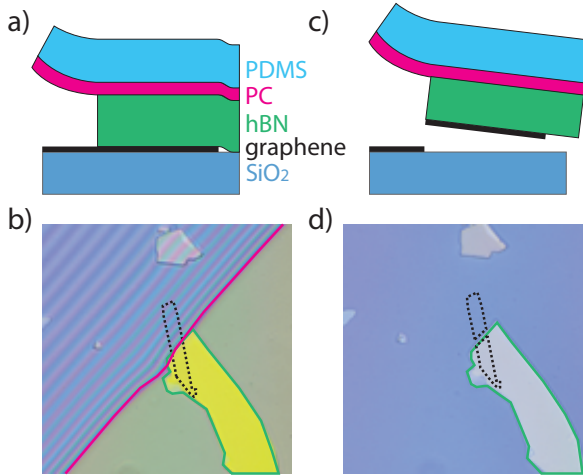
Figure 3.3. a) Schematic drawing during the pick-up process for twisted bilayer graphene. The hBN is in contact with one half of the graphene flake. b) Microscope image of the situation shown in a). The PC interface is kept at the edge of the hBN flake. The graphene is encircled by a black dashed line, the hBN in green and the PC interface is indicated by the pink line. c) Schematic drawing of tearing the graphene in two pieces by retracting the stamp. d) Microscope image of the situation sketched in c) after the graphene was torn.

was employed for the evaporation mask with a varying thickness between 300-450 nm. The details can be found in App.A.3.1.

Sputtering of MoRe

The MoRe films were sputtered in a AJA ATC Orion system. In this system it is possible to sputter not only from one target but multiple ones at the same time. For the fabrication of the superconducting films we used two approaches. One approach is to co-sputter the film from separate Mo and Re targets. This allows us study some of the basic physical properties as a function of the Mo and Re ratio. For the other, we sputtered from a single target with a one to one Mo:Re composition, which was mainly applied for the superconducting contacts to graphene. The exact recipe is given in App.A.4.1.

3.2.2. MoRe characterization

The results in this section are a summary of the main findings of my project work supervised by Dr. Markus Weiss [132], where the superconducting properties of Mo_xRe_{1-x} was studied for various compositions, where the index x denotes the percentage of Mo in the alloy. As priorly mentioned these films were fabricated by co-sputtering the Mo and the Re from different targets. The investigated structures were 50 nm thick, 10 μm long and 1 μm wide metal stripes.

Critical temperature and magnetic field

We found that the T_c varies between 6 and 9 K before it decreases below 1.8 K for higher Mo concentration (see Tab.3.1). The critical field B_c^2 at which the superconductivity fully breaks down was usually larger than 8 T at 1.8 K and therefore above the maximal field reachable by the measurement set-up. By applying the Slisbee rule [133], which describes the relation between the applied magnetic and the critical current density we extrapolated the values for B_c^2. The results are shown in Tab.3.1. This fields are larger compared to previous published results of ∼8 T [85, 134]. The difference of serveral teslas is maybe a consequence that MoRe is a type-2 superconductor, that hosts vortex of one flux quantum in the film above a certain magnetic field, which is not taken into account in the model of Slisbee [133].

Kinetic inductance and London penetration depth

The kinetic inductance (L_k) of a superconducting material originates from the kinetic energy of the Cooper pairs and can be seen as energy invested to create a magnetic field. Its value given by $L_k = ml/(nAe^2)$, where m is the charge

Mo_xRe_{1-x}	0	0.05	0.1	0.2	0.3	0.4	0.5	0.6	0.7	0.8	1
T_c (K)	1.7-2.4 [134, 135]	6	8.3	8.8	8.3	7.7	7.3	8.5	8.3	<1.8	0.92 [136]
B_c^2 (T)	0.25 [137]	5.2	11.3	11.9	12.1	16.5	11.8	9.9	8.9	-	0.01 [136]

Table 3.1. Critical temperature and critical magnetic field for different ratios of Mo and Re thin films with a thickness of 50 nm.

carrier mass, n the charge carrier density, l the lengths of the conductor, A the cross section of the conductor, and e the elementary charge.

To determine L_k, we fabricated a $\lambda/4$-resonator out of MoRe (1:1), where λ is the wavelength. The coplanar wave-guide had a thickness of 70 nm, a length of $l=12\,\mu m$, and the width of the central conductor respectively the gap between the central conductor to the ground plane were $12\,\mu m$ and $6.5\,\mu m$. It was fabricated on a intrinsic silicon wafer with an silicon-oxide thickness of 170 nm. The resonance frequency (f_{res}) is given by,

$$f_{res} = \frac{1}{4l\sqrt{(L_m + L_k^s)\,C_m}}, \tag{3.1}$$

where L_m is the geometrical inductance per unit length [138], L_k^s the kinetic inductance per unit length, and C_m the resonators capacitance per unit length [139]. The kinetic inductance is varying with temperature and its dependence is given by $L_k(T) = \frac{L_k^0}{1-(T/T_c)^4}$, where L_k^0 is the kinetic inductance at zero temperature. By measuring the temperature dependence of f_{res}, L_k^0 can be estimated by a fit with Eq.3.1. We obtain a value of 355.2 nH/m.

London penetration depth

From the L_k^0 we can calculate λ_L. It is shown in Ref.[138] that for a superconducting co-planar waveguide with a thickness smaller than twice λ_L

$$L_k^0 = \mu_0 \frac{\lambda_L^2}{dw} g(s, w, d), \tag{3.2}$$

where μ_0 is the vacuum permeability and $g(s, w, d)$ a geometrical factor depending on s, w, and d, which are defined in Fig.3.4. The geometrical factor is further given as

$$g(s,w,d) = \frac{1}{2k^2 K(k)^2}\left[-\ln\left(\frac{d}{4w}\right) - \frac{w}{w+2s}\ln\left(\frac{d}{4(w+2s)}\right) + \frac{2(w+s)}{w+2s}\ln\left(\frac{s}{w+s}\right)\right], \tag{3.3}$$

where $k = \frac{w}{w+2s}$ and $K(k)$ is the complete elliptic integral of the first kind. For the dimensions of the resonator $d = 70$ nm, $w = 12\,\mu m$, and $s = 6\,\mu m$ and the extracted kinetic inductance of 355 nH/m, we obtain that $\lambda_L = 180\,nm$ for MoRe.
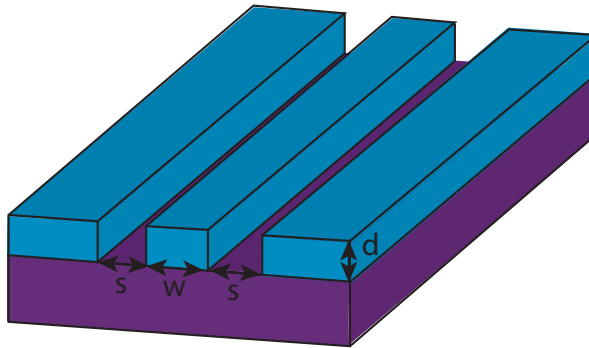
Figure 3.4. Schematic drawing of a segment of a co-planar wave guide. Blue indicates the superconducting material forming the wave guide and purple the dielectric substrate. The width of the central conductor is given by w. The gap between the central conductor and the ground plane by s and the thickness of the film by d.

1D MoRe contacts

If the MoRe is used as a contact material for in hBN encapsulated graphene, the hBN has to be first etched away in the contact regions before the MoRe deposition. After the writing of a PMMA mask by electron beam lithography the hBN is etched with a CHF_3/O_2 plasma using reactive ion etching. Afterwards the MoRe is sputtered, which leads to self aligned, one-dimensional MoRe side contacts [125].

Long or short junction?

It is important to know if our junctions are in a short or a long junction regime regarding the superconducting proximity effect. In a short junction, one can neglect the phase acquired by the Andreev pair during the propagation through the junction in the calculation of the Andreev boundstate energy, since its value is much smaller than the phase acquired in the Andreev reflection. This short junction regime corresponds in the ballistic case for graphene to

$$L \ll \xi_S = \frac{\hbar v_F}{\pi \Delta} \approx 170 \text{ nm} \tag{3.4}$$

with $\Delta = \Delta_{MoRe} = 1.25 \text{ meV}$ and $v_F = 1 \times 10^6 \text{ m/s}$. In the long junction regime ($L \gg \xi_S$) one finds that the phase acquired during the propagation can not be neglected and several solutions for the Andreev boundstates exist

(see. Sec.2.1.1). Further the induced superconducting gap is reduced to the Thouless energy. In the diffusive limit, the coherence length is actually given by $\xi_S = \sqrt{\hbar D/\Delta}$.

Multiple Andreev reflection and Δ_{MoRe}

The superconducting gap of MoRe was measured in a different graphene stacks. To do so, the differential resistance was measured with a standard lock-in technique as a function of voltage bias (V_{bias}). A clear decrease of the differential resistance is observed at eV_{bias}=2.4 meV, that we attribute to twice Δ_{MoRe}. Additional dips of the differential resistance inside the gap arise due to multiple Andreev reflection (MAR) at V_{bias} equal to Δ/e, $2\Delta/3e$ and $2\Delta/5e$. These positions are indicated by the dashed dark blue line in Fig.3.5. The gap size is determined by taking the average over all extracted values of the gap including the MAR. We obtain that $\Delta_{MoRe} = 1.25$ meV, which is similar as measured by Borzenets et al. [50] (Δ_{MoRe}=1.2 meV). In the region around V_{bias}=0, the dV/dI drops to 0 because of a supercurrent flowing through the JJ as soon as $V_{bias}/R_L < I_c$, where R_L is the line resistance. This effect is caused by the finite value of R_L (R_L=137 Ω) leading to an effective current bias of the sample.
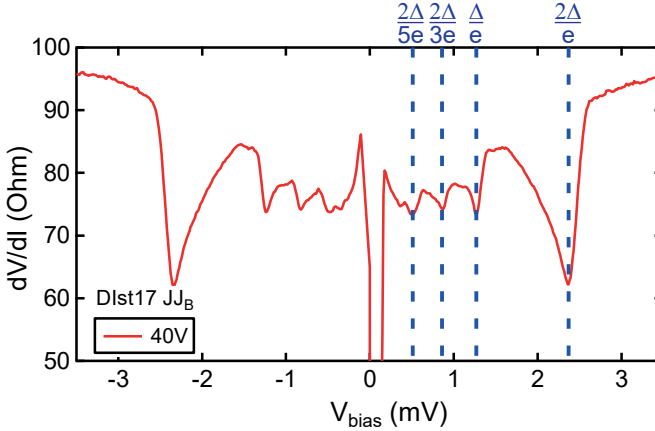

Figure 3.5. Differential resistance as a function of V_{bias} at a V_{bg}=40 V measured with an ac-voltage amplitude of 20 μV at 377 Hz. The vertical blue dashed lines are indicating the positions of the gap edge and the MAR at $V_{bias} = \Delta/e, 2\Delta/3e$ and $2\Delta/5e$.

3.3. Data processing
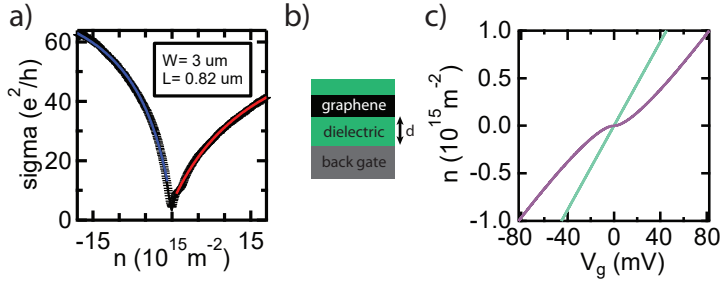
Figure 3.6. a) Two terminal conductivity of a graphene junction as a function of charge carrier density. The curve was fitted with Eq.2.29, once for the electron side ($n > 0$) shown in red and once for the hole side ($n < 0$) shown in blue. The values of the mobilities and contact resistance were $\mu_e = 11000\,\text{cm}^2/\text{Vs}$ and R_c^e=92 Ohm for electrons and $\mu_h = 30000\,\text{cm}^2/\text{Vs}$ and R_c^h=80 Ohm for holes. b) Schematic of a encapsulated graphene stack. The back gate is indicated by gray, the graphene by black and the hBN by green. The distance between the back gate and the graphene is given by the bottom hBN's thickness d. c) Calculation of n as function of gate voltage. As gate dielectric we assumed a hBN crystal with a thickness of 10 nm. The green line is calculated by Eq.3.5 with V_{DP} to be zero. The purple line is obtained by Eq.3.7 and therefore includes c_q.

3.3.1. Electrostatic models - How to convert gate voltage to density

From many applications it is important to know the dependence of a quantity with respect to n, which is usually tuned by electrostatic gates. This section summarized the various gate structures used for the measurements in this thesis and explains the electrostatic models, which were used to convert the gate voltages into charge carrier densities.

Plate capacitor model

If a single back- or topgate is used to gate the graphene transport channel, a plate capacitor model can be assumed to convert the applied gate voltage (V_g) to n. The carrier density can then be calculated by

$$n = \frac{c_{tot}(V_g - V_{CNP})}{e},\tag{3.5}$$

where V_{CNP} is given as the position of the CNP in V_g, which can differ from zero due intrinsic or external doping [6, 140], i.e. absorbed solvents, and c_{tot} is the total capacitance per unit area. In the simplest case $c_{tot} = \epsilon_r \epsilon_0/d$, where ϵ_r (ϵ_0) is the relative (vacuum) permittivity of the dielectric material and d the distance between the gate and the graphene, i.e. the dielectric's thickness (see Fig.3.6 b). If a layered structure is used, e.g. hBN encapsulated graphene on a silicone gate, the capacitors have to be successively added in series:

$$\frac{1}{c_{tot}} = \frac{1}{c_{SiO_2}} + \frac{1}{c_{hBN}}, \tag{3.6}$$

where $c_{SiO_2} = \epsilon_0 \epsilon_{SiO_2}/d_{SiO_2}$ and $c_{hBN} = \epsilon_0 \epsilon_{hBN}/d_{hBN}$ with $\epsilon_{SiO_2} \approx 3.9$ / $\epsilon_{hBN} \approx 4$. The limit in charge carrier density by electro static gating is in the order of $10^{16}\,\mathrm{m}^{-2}$ and is given by the dielectric constant and the breakdown voltage of the dielectric, which was measured to be .95/1.2/0.5 V/nm for SiO$_2$, hBN and aluminium oxide [141–143]. We could reproduce the breakdown field of 0.5-0.6 V/nm for the aluminium oxide grown by atomic layer deposition (see A.5). Empirically, the hBN obtained from Taniguchi et al. (A.1.1) can sustain safely 0.5 V/nm without the observation of any leakage current. For the 300 nm thick SiO$_2$, which was used for some the applications, the voltage was limited by the maximum voltage the measurement lines can sustain ($\sim$80-100 V). But sometimes leakage currents at much lower values then 0.3 V/nm were observed. This observation is attributed to a damage of the SiO$_2$, during wire bonding to connect the sample.

Nevertheless, the plate capacitor model is a simplification, since it is assumed that only the electric potential changes. In reality the change of n induces also a change in the chemical potential. This effect has to be taken into account for materials with a small DoS. Therefore, the charge carrier density in monolayer graphene depends on the gate voltage as

$$e(V_g - V_{CNP}) = \frac{e^2 n d}{\epsilon_0 \epsilon_r} + \mu_c(n), \tag{3.7}$$

where $\mu_c = \pm\sqrt{\pi n}\hbar v_F$ is the chemical potential of graphene, $\hbar$ the reduced Plank constant, and v_F the Fermi velocity of graphene. By expressing μ_c by the DoS of graphene and use the relation $k = \sqrt{\pi n}$, we obtain

$$(V_g - V_{CNP}) = q\left(\frac{d}{\epsilon_0 \epsilon_r} + \frac{1}{e^2\,\mathrm{DoS}}\right) = q/c_{tot}, \tag{3.8}$$

where $q = n * e$ the charge density. From Eq.3.8 we see, that this effect can be taken into account by adding a capacitance with a value of e^2DoS, the so called quantum capacitance (c_q), in series with the gate capacitance given by $c_g = \epsilon_0 \epsilon_r/d$. This quantum capacitance comes into play when the DoS is especially small, i.e. at the CNP, or c_g is large. In Fig.3.6 c, we calculated n as a function of V_g with and without taking c_q into account. hBN was assumed

as a gate dielectric with a thickness of 10 nm. A clear deviation between the two curves is observed, which shows the importance of taking the full picture into account, especially around the CNP and for thin dielectrics.

Extract charge carrier density for a single graphene with top- and backgate

If a single layer of graphene is partially cover by a local top gate (see Fig.3.7) the charge carrier density in the top gate covered inner region (n_{in}) can be tuned independently form the outer regions, which is uncovered (n_{out}). But both carrier densities depend on the applied top (V_{tg}) and back gate voltage (V_{bg}), due to a finite cross capacitance between the gates. Instead of calculating the exact electric fields, which also depend on the geometry of the sample, we chosed a different, simpler ansatz to obtain the values of n_{in} and n_{out} as a function of V_{bg} and V_{tg}.

In first step the lines of charge neutrality of the inner and outer regions were extracted. These lines are given by clear maxima in the resistance since one or the other region is at the CNP. Note that these lines are depending on both gate voltages and are an expression for n_{in} or n_{out} equals to zero. Therefore, we obtain the ratio between the lever arms given by the slopes of the gray and black dashed lines, since the effect of one gate has to be compensated by the other to stay at charge neutrality. Assuming that we can neglect the quantum capacitance, the charge carrier density as a function of V_{bg} is given by Eq.3.5. Then we can multiply the value by the ratio of the lever arms to obtain the charge carrier density as a function of V_{tg}. We take the back gate as a starting point for this estimation knowing the thickness of the SiO$_2$ and its dielectric constant, since it can be modelled by a plate capacitor. For the top gate and especially the outer regions, one would have to take the distance dependence as well as direction of the electric field into account. This two reasons are also the cause of the imperfection of the described procedure. Since we only obtain an average lever arm for the top gate, the local charge carrier density variation in the inner and outer regions are unknown. Nevertheless, it gives a good first estimation of n_{in} and n_{out}.

Double layer graphene with top- and backgate[1]

The structure, which we consider is a double layer graphene (see Fig.3.8), consisting of the following layers listed from bottom to top: 1) graphite bottom gate 2) bottom hBN 3) bottom graphene layer 4) middle hBN 5) top graphene layer 6) top hBN 7) aluminium oxide 8) metal top gate. The charge carrier density in the top (n_t) and the bottom (n_b) graphene were calculated from V_{tg} and V_{bg} using the electrostatic model described in the following section.

---

[1]This section has been published in the SI of [101]
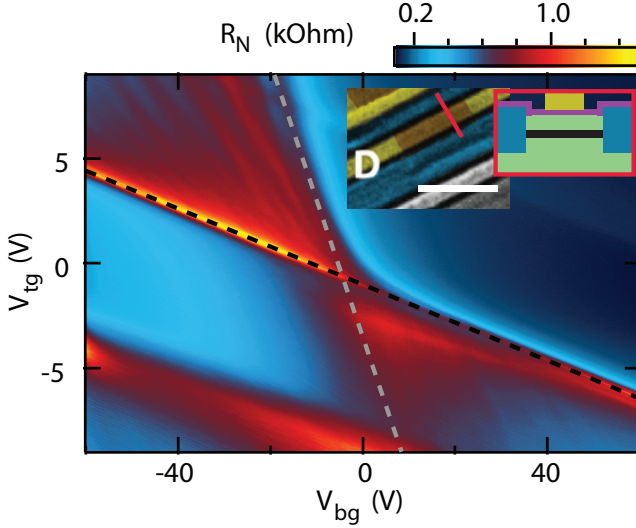
Figure 3.7. Normal state resistance of a graphene based JJ as a function of a local top and global bottom gate. The black (gray) dashed line indicates the position of zero charge carrier density of the graphene covered (uncovered) by the top gate. Inset: right: A false coloured SEM picture show the measured JJ (scale bar $1.5\,\mu$m). The superconducting contacts are blue, the local top gate yellow and the location of the graphene is indicated by brown. left: A schematic drawing of a cut along the red line. The hBN is coloured green, aluminium oxide lilac and graphene black.

The top gate is electrically separated from the top graphene by an aluminium oxide layer with a thickness of $d_{Al_2O_3}$ and a dielectric constant $\epsilon_r^{Al_2O_3} = 8.5$ and the top hBN with a thickness of d_t and $\epsilon_r^{hBN} = 4$. A hBN with a thickness of d_{gg} between the two graphene sheets electrically disconnects the two layers, which are shorted at two common 1D edge contacts. hBN was also used as a dielectric material between the bottom graphene plus electrodes and the bottom gate. The thickness of the bottom hBN layer is given by d_b. Since the two graphene layers, which are connected in parallel, are electrically shorted at the contacts, they are at the same electro-chemical potential, which is chosen to be equal to zero, i.e. ground, for the following calculation. From this follows that,

$$\mu_c^t - eV_t = \mu_c^b - eV_b = 0, \tag{3.9}$$
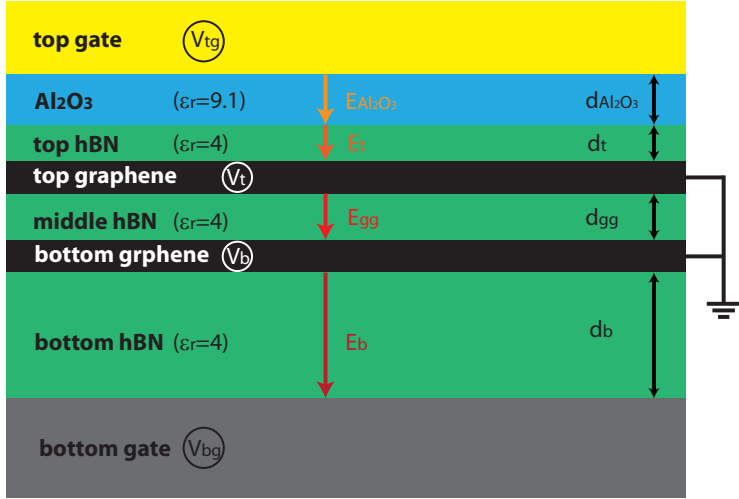
Figure 3.8. Schematic side view of the double layer graphene stack.

where μ_c^t, μ_c^b are the chemical potential and V_t, V_b are the electrical potential of the top, respectively the bottom graphene and e is the elementary charge. For graphene the chemical potential is given as,

$$\mu_c^i = \text{sgn}(n_i)\hbar v_F \sqrt{\pi |n_i|}, \tag{3.10}$$

where $\hbar$ is the reduced Planck constant, $v_F = 10^6\, m/s$ the Fermi velocity of graphene and n_i the charge carrier density in the i-th graphene layer. The $\text{sgn}(n_i)$ function is such that it is positive for electron doped and negative for hole doped graphene.

To describe the electrostatic situation we look carefully at the electric fields E_i, where the index i denotes the different dielectrics, which are a consequence of applied gate voltages, quantum capacitance and charge carrier density on either graphene. The electric fields are defined as shown in Fig.3.8. In a first step we express $E_{Al_2O_3}$ in terms of E_t. If we consider the interface between the two dielectric materials to be charge free, it follows directly from the Maxwell equations that normal components of the two electric fields times their dielectric constant have to be the same at the interface. In this case $E_{Al_2O_3}$ is given by,

$$E_{Al_2O_3} = \frac{\epsilon_r^{hBN}}{\epsilon_r^{Al_2O_3}} E_t. \tag{3.11}$$

Using Gauss law we can write down n_t and n_b as a function of the electric fields.

$$-en_t = \epsilon_0 \epsilon_r^{hBN}(E_{gg} - E_t) \tag{3.12}$$

$$-en_b = \epsilon_0 \epsilon_r^{hBN}(E_b - E_{gg}) \tag{3.13}$$

where the vacuum permittivity is given as $\epsilon_0 = 8.854 * 10^{-12}\, F/m$. Further the electric fields are given by the voltage differences between the layers and leads to the following sets of equations:

$$E_b d_b = V_b - V_{bg} \tag{3.14}$$

$$E_{gg} d_{gg} = V_t - V_b \tag{3.15}$$

$$E_t d_t + E_{Al_2O_3} d_{Al_2O_3} = V_{tg} - V_t. \tag{3.16}$$

The magnitude of the electric field between the two graphene sheets follows from Eq.3.15 and 3.9,

$$E_{gg} = \frac{V_t - V_b}{d_{gg}} = \frac{\sqrt{\pi}\hbar v_F}{e d_{gg}}\left(\operatorname{sgn}(n_t)\sqrt{|n_t|} - \operatorname{sgn}(n_b)\sqrt{|n_b|}\right). \tag{3.17}$$

From Eq.3.14 we obtain that $V_{bg} = V_b - E_b d_b$, while E_b can be expressed as a function of n_b and E_{gg} using Eq.3.13. Therefore it follows that $V_{bg}(n_t, n_b)$ is given as,

$$\begin{aligned}
V_{bg} &= V_b + d_b\left(\frac{en_b}{\epsilon_0 \epsilon_r^{hBN}} - E_{gg}\right) \\
&= \frac{\operatorname{sgn}(n_b)\sqrt{\pi}\hbar v_F}{e}\sqrt{|n_b|} + \frac{en_b d_b}{\epsilon_0 \epsilon_r^{hBN}} \\
&\quad - \frac{\sqrt{\pi}\hbar v_F d_b}{e d_{gg}}\left(\operatorname{sgn}(n_t)\sqrt{|n_t|} - \operatorname{sgn}(n_b)\sqrt{|n_b|}\right).
\end{aligned} \tag{3.18}$$

The same can be done for $V_{tg} = V_t + E_t d_t + E_{Al_2O_3} d_{Al_2O_3}$ starting from Eq.3.16. By using the relation between the two electric fields one obtains that,

$$V_{tg} = V_t + E_t\left(d_t + \frac{\epsilon_r^{hBN}}{\epsilon_r^{Al_2O_3}} d_{Al_2O_3}\right) \tag{3.19}$$

For simplification we define $d_t^{eff} = d_t + \frac{\epsilon_r^{hBN}}{\epsilon_r^{Al_2O_3}} d_{Al_2O_3}$. Again we can replace E_t with Eq.3.12 and in the and we obtain the result,

$$V_{tg} = \frac{\text{sgn}(n_t)\sqrt{\pi}\hbar v_F}{e}\sqrt{|n_t|} + \frac{en_t d_t^{eff}}{\epsilon_0 \epsilon_r^{hBN}}$$
$$- \frac{\sqrt{\pi}\hbar v_F d_t^{eff}}{ed_{gg}}\left(\text{sgn}(n_b)\sqrt{|n_b|} - \text{sgn}(n_t)\sqrt{|n_t|}\right). \tag{3.20}$$

Eq. and 3.19 are giving the relation between the gate voltages and the charge carrier densities. To obtain now the charge carrier densities for two given voltages the equations were inverted numerically.

3.3.2. Determination of the superlattice twist angle [2]

As described in Sec.2.3 the alignment of the crystallographic axis of graphene and hBN leads to a moiré superlattice (see Fig.3.9 a). This new lattice has a wavelength λ, which corresponds to a wavevector of $|G| = \frac{4\pi}{\sqrt{3}\lambda}$ [23] gives rise to a modification of the graphene's bandstructure, e.g. secondary Dirac points (sDP), due to an additional periodic potential. The sDPs manifest themselves as resistance peaks at densities away from the charge neutrality point of graphene as shown in Fig.3.9 b). From the position of the sDPs in density we can determine the twist angle between the hBN and graphene, since they are expected to appear at the edges of the new Brillouin zone. The edge is given for $k = |\vec{k}| = |G|/2$, while $\vec{k}$ is related to the density n by $k = \sqrt{4\pi n/(g_v g_s)}$, where g_s and g_v are the spin respectively valley degeneracy. In the case of graphene, g_s and g_v are both equal to two. Therefore,

$$\lambda = \sqrt{\frac{4\pi}{3n_{sDP}}}. \tag{3.21}$$

where n_{sDP} is the density at which the sDP is appearing. Further, $|G|$ can be determined geometrically [67].

$$|G| = \frac{4\pi}{\sqrt{3}a}\sqrt{\delta^2 + \theta^2}, \tag{3.22}$$

where a=0.246 nm is the lattice constant of graphene, δ=1.8% is the mismatch of the lattice constant of graphene and hBN [58], and θ is the misalignment angle between the two crystals. From Eq.3.22 it follows that $\lambda = a/\sqrt{\delta^2 + \theta^2}$, which then can be used to solve Eq.3.21 with respect to θ. This leads to

$$\theta = \sqrt{\frac{3a^2 n_{sDP}}{4\pi} - \delta^2}. \tag{3.23}$$

---

[2]This section is similarly published in Ref.[57]
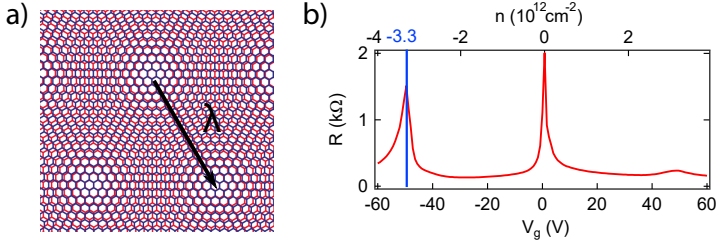
Figure 3.9. a) Schematic drawing of a moirée superlattice for a rotation angle of 0° and a lattice mismatch of 6%. λ is determining the typical wavelength of the appearing hexagonal lattice. b) Two terminal resistance of a graphene-hBN superlattice junction as a function of gate voltage. From the gate voltage the carrier density was calculated using an simple plate capacitor model. One peak in resistance is observed at the charge neutrality point ($n=0$) and two others at around $\pm 3.3 \times 10^{12} \, \text{cm}^{-2}$ (blue line).

3.3.3. Analysis of interference patterns: extraction of the current distribution

In this section, we describe the procedure used to extract the current distribution $j_s(x)$ from the interference pattern of the critical current I_c as a function of magnetic field B, following [51, 144, 145]. We choose the graphene sheet to lie in the x-y plane with contacts along x from -W/2 to W/2, a length of L and an out of plane magnetic field in z-direction.

Figure 3.10. Model of a graphene based Josephson junction with contacts in x direction, a supercurrent flowing in y. To measure the interference pattern, a perpendicular magnetic field in z direction is applied.

3.3.4. Extracting j from interference pattern

We assume that the supercurrent in graphene can be described approximately with a sinusoidal current-phase relation (CPR), i.e.

$$j_s(x) = j(x)\sin(\varphi(x)), \tag{3.24}$$

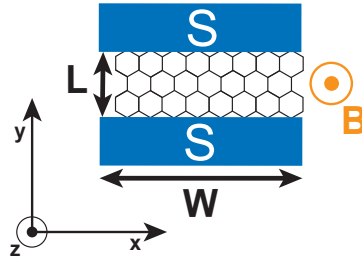where j is the maximum supercurrent density and φ the superconducting phase difference between the two superconductors.

If a perpendicular magnetic field is applied, two supercurrent paths flowing through the junction pick up an additional relative phase with respect to each other, which depends on the enclosed flux by the two paths. Therefore, the superconducting phase at position x is given by the integration of the perpendicular magnetic field B over the penetrated area S added to a reference phase $\varphi_0 = \varphi(x = 0)$ and is expressed as

$$\varphi(x) = \varphi_0 + \frac{2\pi}{\phi_0} \int_S B ds = \varphi_0 + \frac{2\pi\Phi(x)}{\phi_0}, \tag{3.25}$$

where $\phi_0 = h/2e$ is the flux quantum and $\Phi = B * S(x)$ the magnetic flux. The area is given by $S(x) = (L + 2\lambda_L) * x$, where λ_L is added twice to the junction length to take the magnetic focusing of the contacts in to account.

Therefore the total mediated supercurrent J_s can be calculated by the integration along the junction width W.

$$\begin{aligned} J_s(\beta, \varphi_0) &= \int_{-W/2}^{W/2} dx\, j(x)\sin(\varphi_0 + \beta x) \\ &= Im\left[e^{i\varphi_0} \int_{-W/2}^{W/2} dx\, j(x) e^{i\beta x} \right], \end{aligned} \tag{3.26}$$

with $\beta = 2\pi B(L + 2\lambda)/\phi_0$. Note that $j(x)$ is in general a sum of the even part $j_e(x)$ and the odd part $j_o(x)$ of the current distribution. For a fixed magnetic field, one can vary φ_0 to obtain the maximum current J_c known as critical current of the JJ. We assume now an even current distribution, such that the problem simplifies and the measurable quantity I_c can be express as

$$I_c(\beta) = \left| J_c(\beta) \right| = \left| \int_{-W/2}^{W/2} dx\, j_e(x) e^{i\beta x} \right|. \tag{3.27}$$

The measurement, represented in blue in Fig.3.11 a, is actually $|J_c|$, such that we have to reconstruct J_c. This is done by inverting the sign of every second lobe of I_c (see Fig.3.11 a). To prevent discontinuities, we subtracted a constant background from I_c to shift its value to 0 nA for magnetic fields
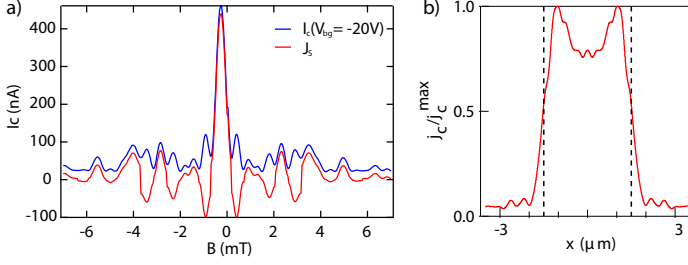
Figure 3.11. a) Measurement of critical current (blue) and reconstructed supercurrent (red) as a function of magnetic field. b) Calculated and normalized current density as a function of x. The black dashed lines are indicating the position of the junction edges along the contacts.

of 6 mT. This background arises partly due to the used measurement method described in Sec.3.4.

By calculating the inverse Fourier transform of J_c the current density in real space can be determined as

$$j(x) \approx \int_{\beta_{min}}^{\beta_{max}} d\beta J_c(\beta)e^{i\beta x}.$$ (3.28)

The result of the described procedure is shown in Fig.3.11b.

3.4. Measure I_c with a counter

To measure the critical current or to be more precise the switching current of a JJ is an important task in various experiments. The switching current is defined as the current where a JJ undergoes the transition from its superconducting state to the normal state. Due to thermal fluctuations and the junction dynamics the switching current has a stochastic behavior [146] and is smaller than the critical current. Here, we describe a method to measure the switching current fast and to take care of its stochastic nature by employing a counter.

Through out this thesis we used a FCA 3100 counter. With this instrument one can measure the time intervals and obtain their mean value, the standard deviations, the minimum and maximum value, as well as the histogram of the time intervals.

To measure the switching current one can proceed as the following. A saw tooth ac-current is created using a signal generator, which applies an ac-voltage

(V_{bias}) with a certain peak-to-peak voltage (V_{pp}) and frequency (f) on a pre-resistor (R_{pre}) in series with the JJ. Then the voltage across the junction is measured and fed to the counter. The time is detected between t_0, the starting time where V_{bias} is at 50% of the falling slope, and t_{meas}, where a voltage equal to V_{trig} arises over the junction (see Fig.3.12). The average of several hundred switching events is taken resulting in t_{mean}. From t_{mean} the critical current can be calculated since the shape of the applied current is known. I_c is given by

$$I_c = \frac{1}{R_{pre}} \left(V_{off} + \frac{V_{pp}f}{z}(t_{mean} - \frac{1}{2f}) \right), \qquad (3.29)$$

where V_{off} is a dc-offset voltage and z is the ratio of the rising slope of one period $T = 1/f$.
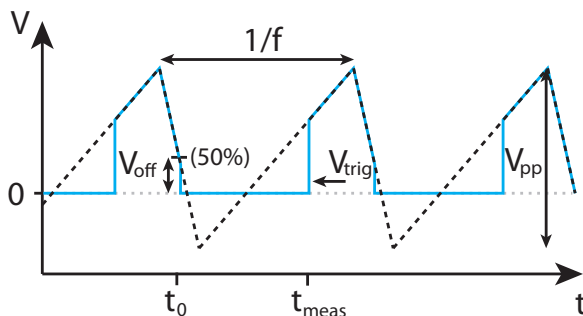
Figure 3.12. Applied (black dashed line) and measured voltage across at the JJ. t_0 denotes the starting time of the measurement.

In general, this sounds like an easy task, but there are some important details to consider to prevent measurement errors. To apply the counter method one has to use a quasi-four terminal measurement meaning that each superconducting contact has to be connected by two electrodes. Like this it is possible to measure zero voltage over the junction when it is in the superconducting state. If the measurement would be only two terminal the line resistance (R_L) in series with the JJ would lead to a finite slope in the superconducting state. As soon as $R_L I_{bias} = V_{trig}$ the counter would stop the measurement even tough $I_{bias} < I_c$. Another important point is to have a sharp switching behavior from the superconducting to the normal state, such that the switching is clearly detectable. By filtering the measurement setup the noise level for $V_{meas} = 0$ can be reduced and therefore V_{trig}, which has to be placed well

above the noise level to minimize the number of wrong trigger events, that appear when the voltage noise exceeds V_{trig}. The smallest switching current that can be measured is then given by V_{trig} divided by the sample resistance in the normal conducting state. An important point is to check the measurement setup with an oscilloscope to check the applied voltage and measured voltage across the junction. By doing so, one can set in first place the right value of V_{pp}, which has to be larger than $2R_{pre}I_c$, such that the junction actually switches to the normal state with in one period. Further, f has to be set such that there is no phase shift between V_{bias} and V_{meas} or any other disturbance of the signal caused by the filtering of high frequency signals. Nevertheless the frequency should be set as high as possible to average as many switching events as possible in a short time. The frequencies used in this thesis were typically between 177-277 Hz. As indicated by Eq.3.29, one can set a dc off-set voltage to shift the saw-tooth like V_{bias} with respect to zero. The important condition is that V_{off} has to be smaller than $V_{pp}/2$, such that the bias current turns negative at the minima to ensure that the junction switches into the superconducting state.

3

4 Signatures of VHS probed by supercurrent in graphene-hBN moiré Josephson junctions[1]
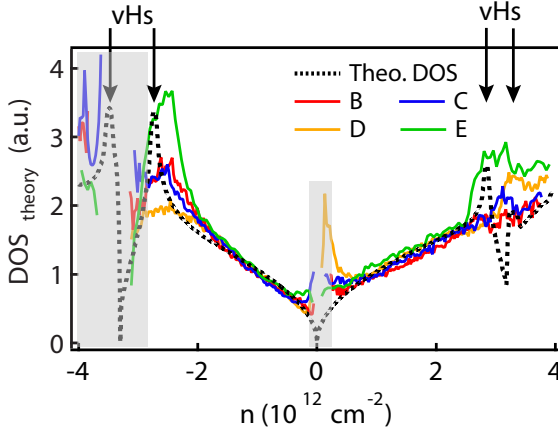
Graphene placed on hexagonal boron-nitride can form a moiré superlattice, if the twist angle between their crystallographic axis is small because of the only slight mismatch of their lattice constant. This additional periodic potential strongly modifies the graphene's bandstructure and manifests itself by new minibands and additional Dirac points accompanied by van Hove singularities. In this chapter we summarize the results of probing the van Hove singularities by supercurrent measurements in long diffusive and ballistic Josephson junctions. Clear signs of these singularities were observed in the density of states calculated from the normal state resistance and the critical current, an appearance of increased edge current due to a reduced Fermi velocity in the bulk, as well as in the Fabry-Pérot oscillations in a electrostatically formed cavity.

---

[1]Parts of this chapter were published in a similar form in Ref.[57]

4.1. Introduction

The combination of graphene with other 2D materials is a powerful means to engineer its electronic properties as described in the introduction and Sec.3.1.2. In particular, if graphene is placed on top of a hexagonal boron-nitride (hBN) substrate, by aligning their crystallographic axes, a moiré superlattice is formed as described in Sec.2.3 & 3.3.2. This superlattice gives rise to new minibands forming satellite Dirac points (sDP) and van Hove singularities (vHSs).

Graphene-hBN superlattices [23, 24, 83] and the induced vHSs [63, 147, 148] have been widely studied with normal metal leads, but only few experiments have focused on the consequences of this rich physics for the Josephson effect. The investigation of the non-dissipative current induced in a non-superconducting system using a Josephson junction (JJ) geometry is a powerful tool to investigate its physical properties, since the supercurrent is sensitive to the transport regime (ballistic/diffusive) [48–50, 84, 149], interactions [150, 151] and to the current distribution within the sample. For example, Josephson interferometry has been used recently to detect the presence of edge current in quantum spin Hall systems [117, 145] and in graphene where an edge current was observed close to the charge neutrality point (CNP) due to guided wave states [144] or, in bilayer graphene, due to the opening of a gap in the bulk using an electric field [66]. In Ref.[66], edge current in a graphene/hBN superlattice at the CNP is reported, where it is claimed that a gap opens due to sublattice symmetry breaking [24, 152]. In contrast to these previous works, we investigate the supercurrent over the full range of energy, in order to probe the superlattice bandstructure.

We investigate the superconducting transport in long, diffusive as well as in a long, ballistic JJs made from graphene/hBN superlattice and show that the supercurrent carries, in this transport regime, the signature of its very specific bandstructure, in particular of the vHSs. First, by measuring both the normal state resistance (R_N) and the critical current (I_c), we estimate the density of states (DoS) of the diffusive JJs. It is then compared to theoretical calculations for a moiré superlattice. Further, we extract the current distribution in the sample as a function of the charge carrier density from the magnetic field dependence of I_c and show that edge currents appear at the vHSs, where the DoS diverges. We show that this edge current corresponds to a suppression of the supercurrent in the bulk, associated with the reduction of the Fermi velocity at the singularity that globally localizes the electrons. This suppression is not observed in the edges probably because of edge defects or doping, which reduce the influence of the superlattice. Second, we measured the charge carrier dependent oscillations of R_N and I_c of a gate defined Fabry-Pérot (FP) cavity in a long, ballistic JJ. The sudden appearance of an oscillation in I_c close to the sDP is indicating a change of the charge carrier type in the FP cavity, namely from holes to electrons, when the vHS is crossed.

4.2. Fabrication

The measured samples are hBN-graphene-hBN stacks, where the crystal axis of one hBN is aligned with the one of graphene. The heterostructures are contacted with superconducting edge-contacts [125]. We fabricated the electrodes by co-sputtering of MoRe (1:1) from separate molybdenum and rhenium targets for device one. For device two the sputtering was performed using a single MoRe (1:1) alloy target (A.4.1). Several JJs are realized in both stacks and the overall charge carrier density can be tuned by a global doped silicon backgate using 300 nm of SiO_2 as a dielectric. In the following we refer to the i-th JJ on device one by JJ_i^1, respectively by JJ_i^2 for the second device. Multiple junctions of device one were studied with different lengths L ranging from 0.45 to 1 μm and a width of $W=3\,\mu$m (see Fig.4.1 a). For device two we focus on JJ_D^2 with $L=550$ nm and $W=1.5\,\mu$m. For this junction a local metal topgate, which extends about 350 nm, was placed over the entire width of the graphene transport channel (see Fig.4.3 a) to electrostatically define a FP cavity. Aluminium oxide was used as the dielectric material between the top gate and the device grown by atomic layer deposition. Details of the fabrication are described in Ch.3 and in the App.A. All measurements are performed in a dilution refrigerator at a base temperature of $\sim$70 mK.

4.3. Normal state resistance

R_N as a function of the back gate voltage (V_{bg}), i.e. charge carrier density (n), can be used to determine the transport nature, e.g. ballistic or diffusive, in the graphene junction. In a superlattice, the sDPs are appearing as a peak in resistance [23, 152] and the misalignment angle between the hBN and graphene can be calculated from their position in n. Since the critical magnetic field of MoRe (8-9 T) is too large to suppress the superconductivity in the leads without tuning the graphene into the quantum Hall regime, we estimate R_N at $B=0$ T from the quasiparticle current, measured when the JJ is voltage biased with $|eV| > 2\Delta_{MoRe}$, with $\Delta_{MoRe}=1.25$ meV the superconducting gap of MoRe (see Sec.3.2.2). The measurement was performed in a two terminal configuration, such that R_N contains the resistance of the graphene channel R_G together with twice the contact resistance R_c ($R_N=R_G+2R_c$). The line resistance of the measurement setup was subtracted.

4.3.1. Device one: long and diffusive JJs

In the four junctions investigated on device one, we observe an enhancement of resistance around the CNP ($V_{bg}=0$ V) and in addition around $V_{bg}=\pm50$ V, corresponding to a charge carrier density $n_{sDP}=\pm3.3\times10^{12}$ cm^{-2} (see Fig.4.1 b).
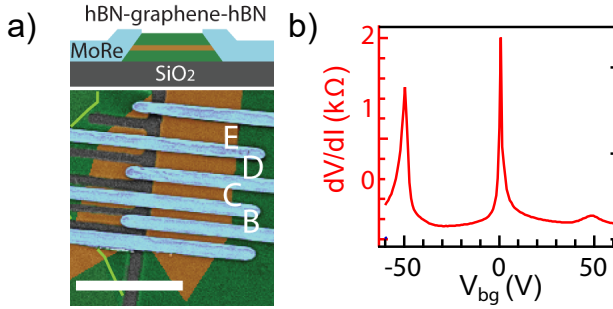
Figure 4.1. a) Top: Schematic side view of the device. Bottom: False colored SEM image. The graphene (brown) is encapsulated between hBN (green) and contacted with MoRe (blue). The white scale bar corresponds to 5 μm. b) Normal state resistance as a function of gate voltage V_{bg} for JJ$_D^1$.

These additional resistance maxima are attributed to sDPs in the bandstructure. From n_{sDP}, we estimate the misalignment angle between the graphene and the hBN lattice to be around 0.7° (see Sec.3.3.2). Further, the resistance for positive gate voltages is significantly larger than for negative voltages, which is attributed to the formation of a hole doped (p) region of the graphene close to the contact, i.e. contact doping. This leads to a reduction of the contact transparency if the graphene is electron doped (n), due to the formation of a pn-junction. Note that in previous works and also device two (see Sec.4.3.2) the reverse behavior was observed, namely an electron doping of the graphenes contact region [50, 85]. This difference may be attributed to the similar work functions of graphene and MoRe [153, 154] and that the MoRe was co-sputtered from individual targets for device one, which gives rise to the possibility, that the contact layer has a different composition, i.e. not 1:1.

The gate dependence of the resistance is one way to determine if the electron transport in the junction is ballistic or diffusive. The mean free path (l_{mfp}) of the electrons is given by $l_{mfp}=2D/v_F$ for a diffusive system, where D is the diffusion coefficient and v_F is the Fermi velocity. Together with the Einstein relation, $\sigma=De^2\,\mathrm{DoS}(E_F)$, where σ is the conductivity, e the electron charge and E_F the Fermi energy, we can express the l_{mfp} as a function of n and R_N for the DoS of graphene as shown in Eq.4.1.

$$l_{mfp} = \frac{2D}{v_F} = \frac{L\sqrt{\pi}\hbar}{R_N W e^2 \sqrt{n}}. \tag{4.1}$$

The l_{mfp} in Tab.4.1 was calculated at $n=\pm 1 \times 10^{12}\,\mathrm{cm}^{-2}$, where we assume

that the bandstructure of graphene close to the CNP is only slightly affected by the superlattice. At higher electron densities the DoS is not linear in energy such that this assumption breaks down [67] and Eq.4.1 does not hold any more. For device one the l_{mfp} is smaller than L for all junctions, from which we conclude that they are in the diffusive regime. As discussed in Sec.2.1.1, the superconducting coherence length of a diffusive JJ is given by $\xi_s = \sqrt{\hbar D/\Delta_{MoRe}}$. The calculation of ξ_s for $n = \pm 1 \times 10^{12}$ cm^{-2} leads to the conclusion, that all JJ of device one are in the long regime ($\xi_s < L$). Note, that l_{mfp} and ξ_s are smaller than L for every value of n, if no change of the bandstructure and the Fermi velocity is assumed. Further, the mobility (μ) and R_c were obtained from the fitting parameters using Eq.2.29. The results are summarized in Tab.4.1.

junction	L (nm)	$l_{mfp}(nm)$	$\xi_s(\mu m)$	$2R_c(\Omega)$	$\mu(cm^2/Vs)$
JJ$_B^1$	450	60/35	0.1	315/350	7'500/4'000
JJ$_C^1$	640	115/85	0.15	137/193	14'000/12'000
JJ$_D^1$	820	190/120	0.2	80/92	30'000/11'000
JJ$_E^1$	1000	230/150	0.2	102/137	37'000/22'000

Table 4.1. Summary of the transport properties of the four junctions on device one. The mean free path was calculated by Eq.4.1 at a charge carrier density of -10^{12} cm^{-2}/+10^{12} cm^{-2}. The coherence length was then estimated from l_{mfp} assuming the Fermi velocity of 10^6 m/s. μ and R_c are the resulting fitting parameters, when the charge carrier dependent conductivity is fitted with Eq.2.29.

Thermally activated gap?

In some monolayer graphene hBN superlattice works, a gap opening has been predicted and observed at the CNP [24, 67, 155], leading presumably to edge currents [66]. In order to determine if there is a gap opening in the DoS of our sample, we measure the resistivity as a function of temperature, represented in Fig. 4.2 a. One can see that, below 100 K, the resistivity only slightly varies. Note as well that the value of the resistivity is not as high as one would expect if there would be a gap [24].

If there is a gap, it should be equal to twice the thermal activation energy E_A extracted from an Arrhenius plot [155]. Namely, by plotting the logarithm of the resistivity as a function of $1/T$, where T is the temperature, one expects a linear behavior as soon the electron transport is thermally activated with a slope of E_A/k_B, with k_B the Boltzmann constant. From Fig.4.2 b, this linear behavior is not observed in our sample, except at large temperature ($T > 100$ K) corresponding to an activation energy of 110 K, and thus a gap of 220 K
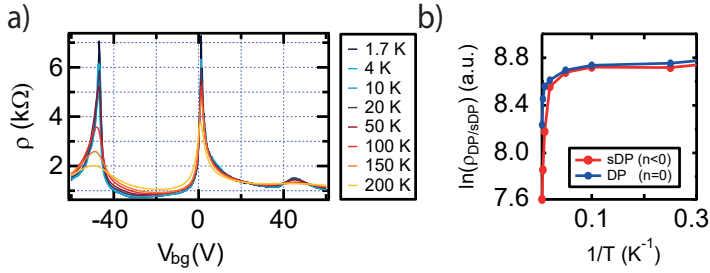
Figure 4.2. a) Temperature dependence of the resistivity as a function of V_{bg} measured for JJ_C^1. b) Arrhenius plot: resistivity at the sDP for $n<0$ (red) and at the CNP (blue) as a function of $1/T$.

($\sim 19\,\mathrm{meV}$). The extracted energy has to be compared with the disorder energy at the CNP. This disorder is caused by electron and hole charge puddles and manifests itself in a finite region close to the DP [156, 157], where the resistance can not be tuned any more by the gate voltage. This appears in device one at charge carrier densities smaller than $3 \times 10^{10}\,\mathrm{cm}^{-2}$, corresponding to a energy of $20\,\mathrm{meV}$. It is thus possible that there exists a gap at the DP induced by the superlattice, but it would not be observed at low temperature due to disorder. Therefore, it will not affect the results discussed in the following parts, since the measurement were taken at around 70-100 mK.

4.3.2. Device two: long and ballistic JJ

Device two has, besides a global back gate, a local top gate on JJ_D^2 (see Fig.4.3 a). If the junction is in the ballistic regime, one can study the dependence of R_N on electrostatically induced Fabry-Pérot cavities as we will show in the following. Further, we will show that also device two carries the typical signature of a superlattice, i.e. the appearance of sDP.

In Fig.4.3 b the normal state resistance of JJ_D^2 is shown as a function of top gate (V_{tg}) and back gate voltage (V_{bg}). The black dashed line corresponds to a configuration where the middle region of the graphene below the topgate is at the CNP and the gray dashed line corresponds to a situation, when the top gate uncovered regions of the sample is at the CNP. The dependence of both CNP with respect of the two gates is given by the cross capacitance. We calculated the charge carrier density below the top gate (n_{in}) and of the outer, uncovered regions (n_{out}) using the procedure described in Sec.3.3.1. R_N is plotted as a function of these densities in Fig.4.4. Four different quadrants, which are separated by the charge neutrality points of the inner and outer
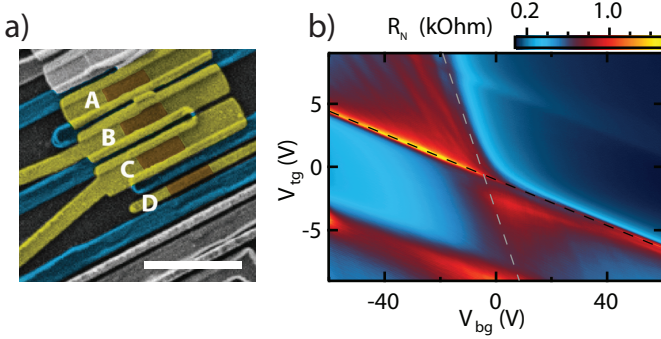
Figure 4.3. a) False colored SEM image of device two (scale bar $3\,\mu$m). The superconducting electrodes are shown in blue, the topgate in yellow, which is insulated by Al_2O_3 from the hBN-graphene-hBN stack in brown. b) Normal state resistance as a function of top- and back gate voltage of JJ_D^2. The black (gray) dashed line corresponds to charge neutrality in gate-gate voltage of the top gate covert (uncovert) graphene. Two lines of increased resistance are observed for positive and negative gate voltages.

regions, are labelled by pnp, nn'n, np'n, and pp'p. The first and the third letter indicate whether the outer regions n or p doped, while the middle letter stands for the doping of the inner region. The apostrophe on the middle letter indicated that the magnitude of the doping may vary to the outer ones. We observed that the resistance is significantly higher in the pp'p regime compared to the nn'n regime, which is due to contact doping and the formation of a pn junction as discussed in Sec.4.3.1 and observed by Refs. [77, 83].

Two lines of increased resistance exist for large $|n_{in}|$ extending parallel to $n_{in} = 0$ and correspond to sDPs (see Fig.4.4). Note that the range of n_{out} is too small to observe the sDPs in the outer regions. The twist angle between the hBN and graphene was determined from the position of the sDP for positive and negative n_{sDP}. Since their absolute value was slightly offset with respect to zero density, the average of the obtained angles was taken. We obtained a misalignment angle between $1.3°$ to $1.4°$. The difference in n_{sDP} can be attributed to the uncertainty of the exact position of the charge neutrality lines and the simplified electrostatic picture to convert the gate voltages in to n_{in} and n_{out}.
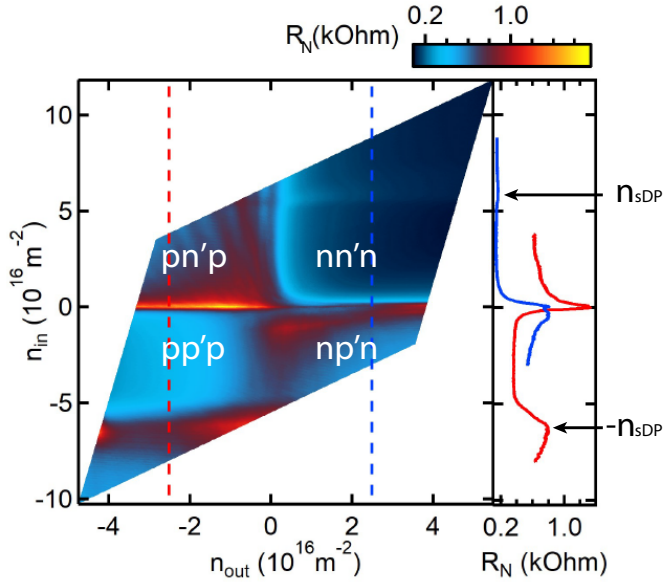
Figure 4.4. Normal state resistance of JJ_D^2 as a function of n_{in} and n_{out}. Two line cuts at $n_{out} = \pm2.5\times10^{16}\,\text{m}^{-2}$ are shown in the right part of the figure. Two peaks in resistance at large values of $n_{in} = \pm n_{sDP}$ are indicated by black arrows.

Investigation of Fabry-Pérot oscillations

In Fig.4.5 we plot R_N as a function of n_{in} and n_{out} for $n_{out} < 0$. Several sets of oscillations of R_N with different frequencies and dependencies in charge carrier densities were observed, which are due to the coherent, ballistic transport inside different FP cavities 2.3.2 formed between pn-junctions induced by gating and contact doping.

The FP oscillations in graphene-hBN superlattice was studied extensively by Refs. [83, 158], where they showed, that FP oscillations also take place, when the pn junction is created by the low energy band and the first miniband. Here, we will focus only at oscillations appearing at energies below the sDP and when $n_{out}<0$, namely p doped. Three sets of FP oscillations are observed and shown in Fig.4.5. Each set corresponds to a different cavity, which can be determined by the different dependence of n_{in} and n_{out}. In the pn'p regime two distinct oscillations were observed. The finer oscillation (green) depends mainly on the change of n_{in}, which we attribute to the cavity formed between

the two gate induced pn-junctions. Whereas, the appearance of the resistance maxima of the more prominent oscillation (blue) depends on both densities and arise due to reflections between the n-doped contact region and pn-junction created by gating. The fact that this oscillation depends not only on n_{out}, can be explained by the finite cross capacitance between the top gate and the outer graphene region, which was not taken into account when the gate voltages were converted to density. Further we observe an oscillation (purple), when both layers are p doped. This variation of R_N is due to a finite reflection possibility at the n doped contact regions. Since the coherence has to be preserved over twice the junction length to observe this effect in the pp'p regime, it leads us to the conclusion of ballistic electron transport in JJ_D^2.

From the period in density one can estimate the different cavity lengths using

$$L_c = \frac{\sqrt{\pi}}{\sqrt{n_{i+1}} - \sqrt{n_i}}, \tag{4.2}$$

where n_i is the position of the i-th maxima of the FP oscillation. For every set of oscillations we estimate L_c by taking an average of the results for several pairs of n_{i+1} and n_i. For the purple oscillation we obtained a length of $L_c^{tot} \approx 550$ nm, for the blue ones $L_c^{out} \approx 75$ nm, and for the green ones $L_c^{in} \approx 350$ nm. The dimensions of this cavities fit roughly the dimensions of the sample (L=550 nm, width top gate 350 nm, and width outer regions 100 nm).

4.4. Probing of DoS in a long, diffusive JJs

Now we will focus on the supercurrent measurements of device number one. We measure I_c, defined as the maximal current that can be passed through the junction before a voltage appears and the junction becomes resistive. To do so, we current bias the sample and measure the differential resistance as a function of bias current I and V_{bg} as shown in Fig.4.6 for JJ_D^1 (see 4.A for junctions JJ_B^1, JJ_C^1, and JJ_E^1). The switching from the zero resistance state to the normal resistance state is detected as a sharp transition at $I = I_c$, as presented in the right panel of Fig.4.6 and plotted as a function of V_{bg} on Fig.4.15 c. No hysteresis was observed between the retrapping and switching current (see Fig.4.6 right), therefore the junction is in the overdamped regime. At the first order, I_c is inversely proportional to R_N, and is thus strongly reduced at the CNPs, beyond the resolution of the measurement. For device one I_c is globally smaller for electron doping ($V_g > 0$) than for hole doping. This reduction of I_c can be attributed to a p-doping of the graphene by the MoRe as previously discussed, which reduces the contact transparency.

All the junctions of both devices we investigated are rather in the long junction limit since the superconducting coherence length $\xi_S < 200$ nm$< L$
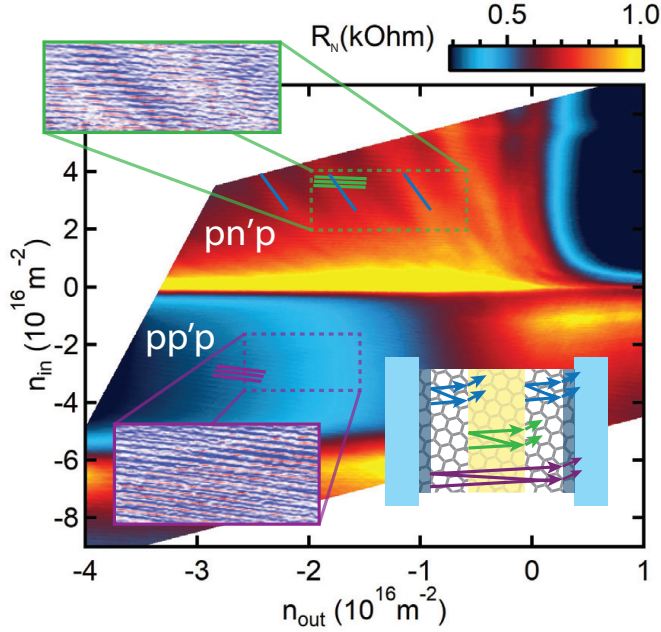
Figure 4.5. Normal state resistance as a function of the densities n_{in} and n_{out}. Three sets of distinct oscillations in R_N are observed. Some of their maxima are indicated by coloured lines. To enhance the visibility of the green and purple oscillations, the derivative of R_N with respect to n_{in} is shown for two different regions in densities. The inset on the bottom right shows a schematic drawing of the device, where the superconducting electrodes are light blue, the topgate position is indicated by yellow and the dark blue region is indicating the n doped contact regions. The coloured arrows relates the interference in each cavity to the oscillation in the density-density map.

(see Sec.2.1.1). Combining the expression of the Thouless energy of a diffusive JJ, $E_{th} = \frac{\hbar D}{L^2}$, with the Einstein relation, $L/W R_G = De^2 \times \text{DoS}$, we find that the DoS as a function of the charge carrier density n can be determined from the measurement of both R_N and I_c:

$$\text{DoS}(n) = \alpha \frac{\hbar}{R_N(n) R_G(n) e^3 L W I_c(n)}. \tag{4.3}$$

Note that this formula involves R_G, the graphene resistance, which is obtained by subtracting the contact resistance R_c from the measured resistance
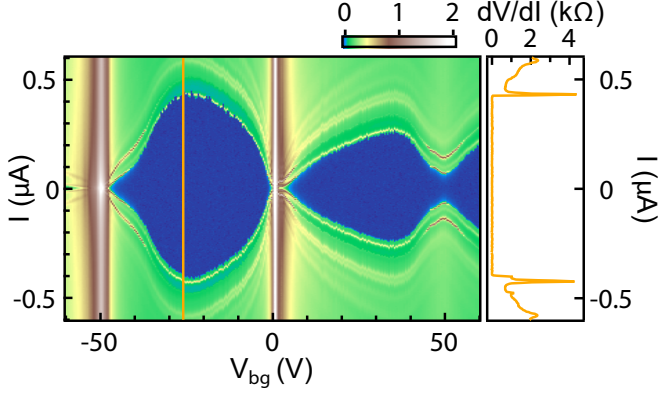
Figure 4.6. Differential resistance as a function of V_{bg} and dc current bias I for JJ_D^1. Right: line cut at V_{bg}=-26 V.

R_N and α is a proportionality factor. In agreement with Refs. [48, 49], we assume that the finite reflection probability at the contacts leads to an increase of τ, the time spent by the particle in the junction, and therefore a reduction of the Thouless energy. This can be observed as a reduced value of α, which is expected to be 10.82 for a diffusive junction [47].

The DoS expected in the graphene-hBN superlattice was calculated in collaboration with J.R. Wallbank using the method described in Ref. [67]. The DoS on the hole side vHS is quite robust to small changes of the moiré parameters used in the theoretical model, while on the electron side it depends significantly on their choice. We chose here parameters similar to those extracted in Ref. [68], adapted to $\theta = 0.7°$, but slightly modified to produce a vHS on the electron side similar to previous measurements [60].

To compare our data with the theoretical calculated DoS, we have to make several assumptions: (i) the measurement of I_c is not affected by the finite temperature, (ii) the coefficient α is constant over the investigated gate range and (iii) R_c is constant respectively for electron and hole doping. For the electronic temperature $T = 100$ mK, we estimate that hypothesis (i) is correct for measured critical currents higher than 30 nA 4.A, which excludes the gate regions around the CNP and the sDP at the hole side from the analysis (see App.4.A). Concerning (ii), Refs. [48] and [49] have shown that α is indeed constant for a long diffusive graphene JJ, even if the measured value of 0.1-0.2 is substantially lower than the one expected for an ideal SNS junction [47]. (iii) is the strongest hypothesis, since R_c can actually depend on V_{bg} and vary within a factor of two around the CNP [159, 160], but since our observation

is stated at high charge carrier density a gate dependent contact resistance would not change the qualitative picture outlined below.
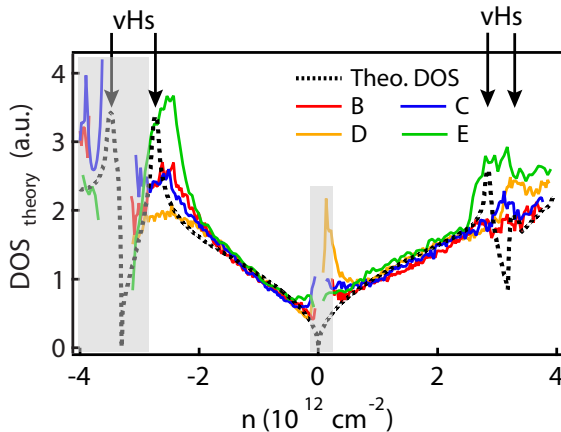

Figure 4.7. Density of state estimated from measured R_N and I_c (Eq.4.3) (in red, blue, yellow and green respectively for JJ_B^1, JJ_C^1, JJ_D^1 and JJ_E^1) compared to a calculation for $\theta = 0.7°$ (black), as a function of the charge carrier density. The moiré superlattice parameters (defined in Ref [68]) used to produce the theoretical DoS are U_0^+=8.5 meV, U_1^+=-8.5 meV, U_3^+=-14.7 meV. The gray shaded areas correspond to regions where the critical current was too small to be reliable extracted due to the finite temperature of the measurement.

Then, by taking R_c and α as fitting parameters, we are able to reproduce the calculated DoS using Eq.4.3 for $\alpha \in [0.3, 0.8]$ and $R_c \approx 40 - 160 \ \Omega$. The result is plotted in Fig.4.7. For the four junctions, this analysis matches qualitatively with the calculated DoS over a large gate range and reproduces well the vHs. As theoretically expected, the superlattice features are less pronounced on the electron side. As a whole, despite some strong assumptions and some uncertainty in the precise value of the contact resistance, we show that the combined measurement of I_c and R_N allows to estimate the DoS, providing information about the specific bandstructure of the superlattice. In particular, we see a clear signature of the vHSs, which was not explicitly present in either R_N or I_c.

The values of R_c are consistent with the contact resistance estimated from the gate dependence of the resistivity (see Tab.4.1). The values of α are consistent as well with the ones that can be found in Refs. [48, 49].

It can be noted that the vHS at negative V_{bg} is more pronounced for junction

Junction	L (μm)	$2R_c(\Omega)$	α
JJ_B^1	0.45	275-320	0.75-0.7
JJ_C^1	0.64	115-150	0.4
JJ_D^1	0.82	80-100	0.45
JJ_E^1	1	75-110	0.3-0.27

Table 4.2. Values of α and of the contact resistance R_c, the fitting parameters used to adjust our data to the calculated DoS (see Fig.4.7). These values are known with an uncertainty of the order of 10%.

JJ_B^1, JJ_C^1 and JJ_E^1 than for junction JJ_D^1. In order to understand this discrepancy, we look now into the current distribution in junction JJ_D^1 (see Sec.4.4.1 for junction JJ_C^1) by measuring the interference pattern of I_c in magnetic field [66, 144].

4.4.1. Device 1: Supercurrent density distribution

As discussed in Sec.3.3.4, I_c as a function of magnetic field reveals the current distribution in the weak link, e.g. graphene, of a JJ. This method is widely used to detect edge currents of JJ established various systems [117, 144, 145, 149].

Edge current at vHSs in JJ_D^1

Here, we discuss a different kind of edge current appearing around the vHSs instead of the CNP as described in Refs.[24, 67, 155], which we attribute to localization of the electrons in the bulk due to a reduced Fermi velocity at the vHS and the simultaneously presence of disorder at the edges.

Typical interference patterns of JJ_D^1 are represented in Fig.4.8 a and compared to the Fraunhofer interference pattern, expected for a homogeneous current distribution [161] and a sinusoidal CPR. Note that, in a ballistic graphene JJ, high transparent channels can lead to a non-sinusoidal CPR [38, 84]. But since we do not expect this high transparency for a long, diffusive junction, we conclude, that the assumed sinusoidal CPR is reasonable for our evaluations. At $V_{bg} = -20\,\text{V}$ ($n_1 = -1.4 \times 10^{12}\,\text{cm}^{-2}$), between the CNP and the vHS, the interference pattern matches a Fraunhofer pattern for the first few lobes, with a periodicity consistent with the junction dimensions taking the finite field penetration into the superconductor into account [144]. At slightly higher fields ($B > \pm 1.5\,\text{mT}$), one can see some missing lobes and a non-vanishing supercurrent, indicating that the current is not perfectly homogeneous. The pattern at $V_{bg} = -40\,\text{V}$ ($n_2 = -2.7 \times 10^{12}\,\text{cm}^{-2}$), close to the vHS, is strikingly different, since the first lobes and the central peak are of comparable amplitude, which is an indication of enhanced edge current [145].
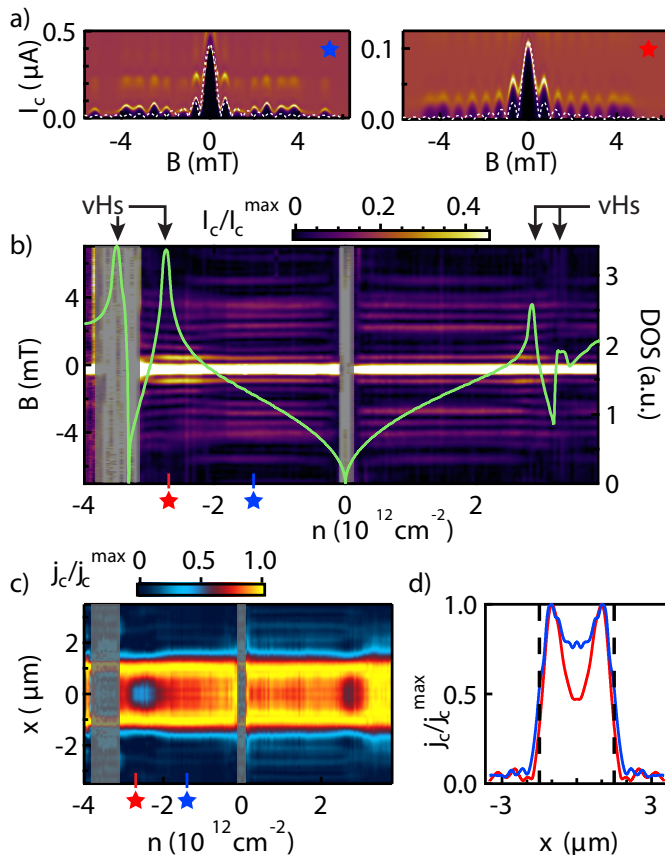
Figure 4.8. a) Differential resistance as a function of current bias and magnetic field at $n_1 = -1.4 \times 10^{12}\,\mathrm{cm}^{-2}$ (blue star) and $n_2 = -2.7 \times 10^{12}\,\mathrm{cm}^{-2}$ (red star). White dashed line: expected Fraunhofer pattern for a homogeneous current density. b) Normalized critical current as a function of magnetic field B and carrier density n measured in junction D, superimposed with the calculated DoS in green. c) Calculated current density as a function of n and position along the contacts. d) Linecuts of panel c) at n_1 and n_2. The black dashed lines indicate the junction edges.

In order to understand the gate dependence, we measure the interference pattern between $V_{bg} = \pm 60\,\mathrm{V}$. We bias the sample with a linearly increasing

current, at a rate $0.17\,\mathrm{mA/s}$. I_c is obtained from the time at which the junction turns normal, averaged 200 times (Sec.3.4). The interference pattern can then be plotted as a function of gate voltage (Fig.4.8 b). In order to compare the shape of the interference patterns, for each V_{bg} the critical current is normalized by its maximum value, $I_c(B = 0)$ for each gate voltage. Note that this kind of measurement cannot detect currents smaller than a few tens of nA, given by V_{trig}/R_N with V_{trig} the threshold voltage for the switching to normal conducting state.

We can distinguish two different regimes for the interference pattern: far from the vHSs, the interference pattern is gate independent and similar to the one described in Fig.4.8 a left. In contrast, around both vHSs, the pattern is similar to Fig.4.8 b right, where the side lobes become more prominent. The effect is stronger for hole doping, where the vHS is more pronounced.

To be more quantitative, we calculate the current distribution in the junction by the inverse Fourier transformation of the interference pattern for each point V_{bg}. The exact procedure is described in Sec.3.3.3 and follows the ansatz given in Refs. [51, 144, 145]. The full map of the current density j_c as a function of n is shown in Fig.4.8 c, where j_c was normalized by the maximal current density of each trace similar to Fig.4.8 b. Two representative distributions are plotted in Fig.4.8 d for n_1 (blue) and n_2 (red), showing that in the whole junction the current partially accumulates on the edges, and that the proportion of edge to bulk current is significantly larger at the vHSs. This change in the proportion is attributed to disorder at the junction edges, which affect the periodic superlattice, such that the electrons are less localized at the edges compared to the bulk at the vHSs.

Adding an odd component to the current distribution

The previous calculation was done by assuming an even current distribution along the contacts. The non vanishing critical current at the minima of the interference pattern indicates, that also an odd part exists in the current distribution $j_o(x)$. Therefore, the expression for $J_c(\beta)$ has to be written as,

$$
\begin{aligned}
J_c(\beta) &= \int_{-W/2}^{W/2} dx j(x) e^{i\beta x} \\
&= \int_{-W/2}^{W/2} dx j_e(x) cos(\beta x) + i \int_{-W/2}^{W/2} dx j_o(x) sin(\beta x),
\end{aligned}
\tag{4.4}
$$

where $\beta = 2\pi B(L + 2\lambda_L)/\phi_0$. The critical current can now be written as $I_c = |J_c| = \sqrt{J_e^2 + J_o^2}$, where J_e and J_o are calculated from even and odd part of the current distribution. From the measured interference pattern we see the even part dominates most of the time, since the overall dependence of $I_c(B)$

follows the Fraunhofer interference pattern expected for a constant $j(x)$. But, from Eq.4.4, it follows that the odd part dominates where J_e vanishes, i.e. at the minima of the Fraunhofer pattern. Since only the absolute value of $J_c(\beta)$ is measured, the J_o has to be reconstructed. To obtain its contribution we followed the Ansatz in Ref.[145] by interpolating between the minima of $I_c(B)$ and flipping the sign between each lobe (see Fig.4.9 a). $J_c(\beta)$ is then equal to $J_e + iJ_o$ and the current distribution is calculated from

$$j(x) = |\frac{1}{2\pi} \int_{-b/2}^{b/2} d\beta J_c(\beta) e^{-i\beta x}|, \tag{4.5}$$

where b is the measured range of β. The result of $j(x)$ is shown in Fig.4.9 b. We observe that one edge is contributing more to the supercurrent transport than the other.

In the next section we will discuss the overall gate dependence of I_c at the edges and the bulk of JJ_D^1 and the influence on the DoS. For this evaluation we focus on the result obtained by assuming only an even current distribution, since no qualitative difference of $j(x = 0)$ was observed between the calculation with or without the odd component j_o. Since the analysis with j_o contains even more assumptions, especially the determination of J_o, we rather limit ourselves to the even component, as describe in Sec.4.4.1.

Recalculation of DoS for subtracted edge current

From the non-normalized map of the supercurrent distribution, we are able to extract separately the gate dependence of I_c on the edges of the junction (I_c^{edge}) and in the bulk (I_c^{bulk}) defined as shown in Fig.4.10. In order to elucidate the nature of the edge current, we use the same procedure as for the result shwon in Fig.4.7 to estimate the DoS of the bulk. For that, we use I_c^{bulk} instead of I_c and the same resistances R_N and R_c assuming that the normal state resistance is dominated by the bulk . The result is shown in Fig.4.10. We find a very good agreement between the DoS extracted from I_c^{bulk} (blue) with the theoretically determined DoS (dotted). In particular, the vHS is now better reproduced than using the total current I_c (plotted in yellow for comparison), meaning that the edge current doesn't carry the signature of the vHS. On the other hand, due to the flat band at the vHS, the Fermi velocity is expected to be globally reduced in the superlattice. This tends to localize the electron by increasing the traversal time τ of the electron in the junction and leads therefore to a reduction of the supercurrent. This localization acts weaker on the electrons at the edges, which leads to an increased edge to bulk current ratio at the vHS for JJ_D^1. Since the vHS is probed for the other junctions without separating the bulk and edge current, no increased edge to bulk current ratio is expected at the vHSs.
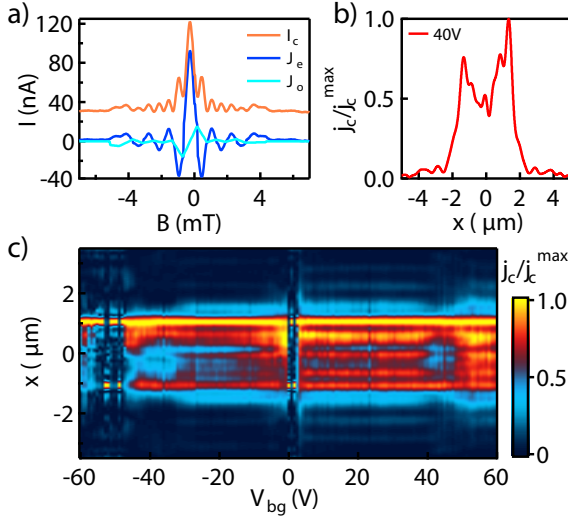
Figure 4.9. a) Measured critical current (green) as a function of magnetic field at a gate voltage of -40 V. In blue (red) the even (odd) part of the reconstructed supercurrent as function of B is shown. b) Current density at -40 V as a function of position. c) Calculated and normalized current density including the asymmetric part of J_c as a function of V_{bg} and position. An enhancement of the edge to bulk current density is observed around the van Hove singularities at $\approx \pm 40$ V.

Supercurrent distribution in JJ$_C^1$

We performed the same measurement and data analysis for JJ$_C^1$ as described in Sec.4.4.1. As discussed we do not expect any increase of the edge to bulk current ratio in this junction, since the DoS calculated from R_N and I_c already probes the vHS at negative V_{bg} without further data processing.

The interference pattern as a function of gate voltage and magnetic field was measured and normalized as described for JJ$_D^1$ (see Fig.4.11 a). It shows a similar behaviour over the entire gate range. Small changes appear at the sDPs at positive gate voltage, which are probably due to the strongly reduced amplitude of the critical current, such that small features can not be resolved anymore due to the limited measurement resolution. The calculation of the current density, which is shown in Fig.4.11 b, does not carry any indication of a increased edge to bulk current ratio around the vHs. This behaviour is consistent with the observation that the estimated DoS from $R_N I_c$ of JJ$_C^1$ probes
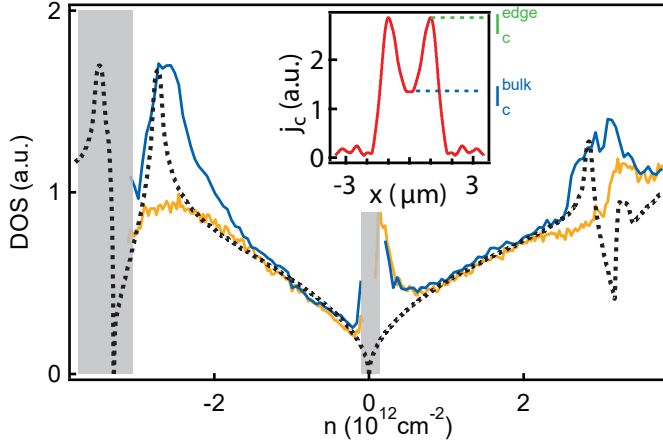
Figure 4.10. DoS as a function of charge carrier density n in junction D, estimated from the bulk current (blue, see inset) and the total current (yellow). Inset: current distribution at the vHS at negative charge carrier density.

the van Hove singularities without additional data processing like for JJ_D^1, where a finite current contribution by the edges had to be subtracted. This suggests, that in JJ_C^1 the edges are more affected by the superlattice potential than in JJ_D^1, and show that both measurements of current distribution and DoS from R_N and I_c are consistent and complementary.

Figure 4.11. a) Interference pattern of critical current of JJ_C^1 as a function of V_{bg} and magnetic field B. b) Calculated current density as a function of V_{bg} and position x for JJ_C^1. The white areas correspond to gates voltages, where the critical current was to small to be measured.

Origin of the edge current

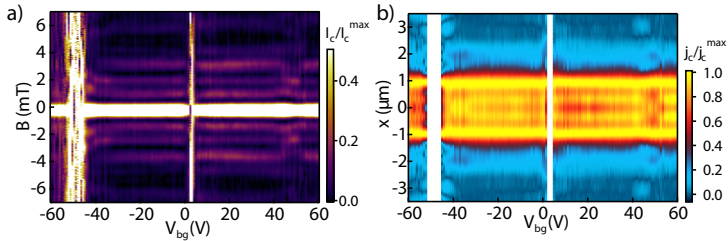It remains to understand why the edges behave differently from the bulk in JJ_D^1. One can rule out the hypothesis of topological edges states due to the valley Hall effect at a gap opening as proposed in Ref.[64] and measured in Ref.[162], because the current at the edges appears far from any band crossing. It has been shown that edge current can be induced as well by guided-wave electronic states due to the band bending at the sample edges [144], but only close to the CNP, where the edge potential is unscreened. Our measurement would be more consistent with previous works reporting edge current induced by electrostatic or chemical doping of the edges [66, 155, 157, 163]. This may induce disorder that can affect the superlattice potential, such that the vHS may be smoothed [164]. This alteration could originate from the exposure of the graphene edge to ambient condition during the fabrication or from contamination during the reactive ion etching used to shape the graphene sheet.

4.5. Signatures of charge carrier change at vHS

In this section we discuss the results of the supercurrent measurements of a long ballistic JJ with a global back gate and a local top gate used to electrostatically define FP cavities. Its normal state resistance as a function of the gate voltages, and the observation of different oscillations in R_N attributed to various FP cavities were described in Sec.4.2. Here, we show that I_c is inversely proportional to the normal state resistance as expected from the Ambegaokar-Baratoff relation [46]. Further, a new set of oscillations were observed in I_c, which was absent in R_N. This appearance of oscillations can be attributed to a change of the carrier type in the FP cavity, when the Fermi energy is tuned over the vHS.

To measure I_c over the entire gate-gate range we applied the counter technique described in Sec3.4. The ramping speed of the current was $2.124\,\mathrm{mA/s}$, the trigger voltage was set to $15\,\mu\mathrm{V}$. An average over 50 switching events was taken to determine I_c.

I_c as a function of n_{in} and n_{out} is shown in Fig.4.12 b. R_N and I_c are plotted as a function of n_{out} for $n_{in} = 3.5 * 10^{16}\,\mathrm{m}^{-2}$ in Fig.4.12c and as a function of n_{in} for $n_{out} = -2.5 * 10^{16}\,\mathrm{m}^{-2}$ in Fig.4.12d. In Fig.4.12c I_c shows further clearly an oscillation, which is shifted by half a period with respect to the one in R_N. Both originate from the FP cavity formed between the pn junction at the contact and the pn junction formed by electrostatic gating (see blue arrows in inset of Fig4.5). If we take now a closer look at the pnp regime, we observe also a set of finer oscillations indicated by the green lines in Fig.4.13b. As discussed in Sec.4.3.2, this modulation corresponds to FP interference effects in the central cavity formed by gating.
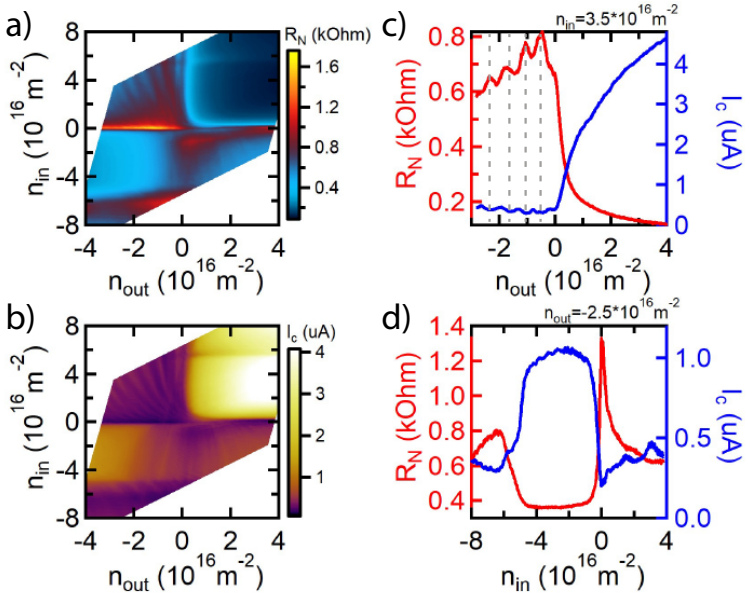
Figure 4.12. a) R_N of JJ_D^2 as a function of n_{in} and n_{out} measured at a V_{bias} of $4\,\text{meV}$. b) I_c of JJ_D^2 as a function of n_{in} and n_{out}. The value of I_c is given by the average of 50 switching events. c) R_N and I_c as a function of n_{out} for $n_{in} = 3.5*10^{16}\,\text{m}^{-2}$. The gray dashed lines indicate the minima of the oscillation in I_c. d) R_N and I_c as a function of n_{in} for $n_{out} = -2.5*10^{16}\,\text{m}^{-2}$.

Surprisingly, we noticed another set of oscillations close to the sDP in the unipolar p-doped region, which was not observed in the measurement of R_N. It appears right before the top gate covered region of JJ_D^2 is tuned to the sDP (see Fig.4.13c) and is accompanied by clear and sudden decrease of I_c. This decrease is observed on a line parallel to the sDP (white dashed line in Fig.4.13c) and defines together with the sDP the region in gate voltages, where the additional oscillations occurs. In Fig.4.13 c the oscillations extend form $0\,\text{V}$ to $-40\,\text{V}$ in back gate and blur for higher values. If we extract the cavity length form the maxima in n_{out} for $n_{in} = -5.25*10^{16}\,\text{m}^{-2}$ using Eq.4.2, we obtain $L_c \approx 60\,\text{nm}$. This length corresponds roughly to the dimension of the top gate uncovered regions. Therefore, we attribute the reduced critical current and the appearance of oscillations with a similar period as in the pnp regime to the change of charge carrier type, when Fermi energy is tuned above the vHS [165]. This leads to a n-doped region below the top gate, which forms

a FP cavity. In similarity, the change of the charge carrier type while crossing the vHs was observed by Lee et al. [68] in a transverse magnetic focusing experiment.
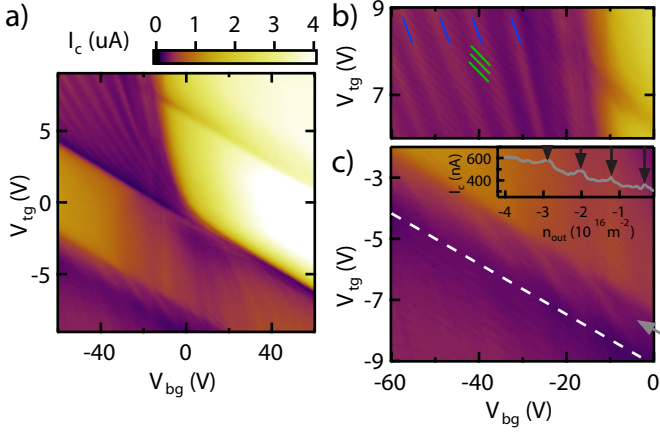

Figure 4.13. a) Critical current of JJ_2^D as a function of top and bottom gate voltage. b) Critical current as a function of top and back gate voltages in the bipolar regime. Two sets of oscillations were observed. The oscillation of I_c indicated by blue lines is due to a Fabry-Pérot cavity between the gate and contact doping induced pn-junctions. The green set corresponds to the central cavity (see Fig.4.5). c) Critical current measured around the sDP. The white dashed line indicated the position of the sDP in the normal state resistance. Inset: Line cut from Fig.4.12 b, which corresponds to the direction of the gray arrow and shows the critical current as a function of n_{out}. An oscillation in I_c is observed and its maxima are indicated by black arrows. The corresponding densities were used to calculate the FP cavity length.

4.6. $R_N I_c$ of a ballistic graphene JJ

In a last step we calculate the product of R_N and I_c for the long, ballistic junction. This value is expected to be proportional to the Thouless energy, which is given by $\hbar v_F/L$. If one simply assumes the junction's length for L=550 nm for JJ_D^2 and $v_F = 10^6$ m/s to be the Fermi velocity of graphene, the obtained value is $E_{th} \approx 1.2$ meV, which is comparable to Δ_{MoRe}. Therefore, the junction is in an intermediate regime between the long and the short junction limit. The measurements are shown in Fig.4.14. Nevertheless, the obtained

value from the measurements is at least a factor of two smaller than the value of E_{th}. This can be a result of a reduction of the Fermi velocity [166] by the hBN-graphene superlattice or that the effective trajectories contributing to the supercurrent transport are in average longer than L, due to reflections at the pn interfaces [86, 167]. The obtained value is not even reduced, but also depends on the doping of the different regions. For example the value of the Thouless energy in the nnn regime is around 0.5 meV and it shrinks to 0.25 meV in the pnp regime. This can be attributed to the finite normal reflection probability at each pn-interface leading to an increase of the trajectory length, exceeding L. Noticeably, the value is not constant in the pnp configuration, which would be expected. A possible explanation can be given by the fact, that R_N was measured at a finite voltage bias of 4 meV, while I_c is measured at zero bias. This voltage bias may lead to a decrease of the amplitude of the FP oscillations as shown in [83, 168], such that they are not fully compensated in the product of $R_n I_c$.
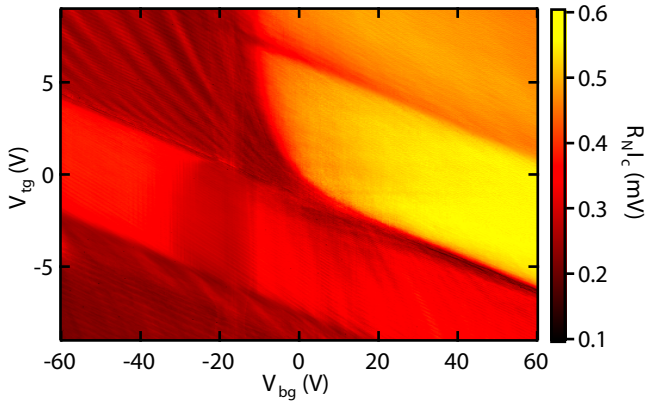
Figure 4.14. Product of R_N and I_c as a function of top and back gate voltage for JJ_D^2.

4.7. Summary

In conclusion, we demonstrate in this chapter that the supercurrent carries the signature of the graphene bandstructure modified by the moiré superlattice. First, from the combined measurement of the normal resistance and the critical current and taking advantage of the diffusive regime, we estimate the DoS in device one and find a very good qualitative agreement with the DoS calculated

theoretically. In addition, Josephson interferometry reveals the presence of a gate dependent edge current in JJ_D^1 and its proportion is strongly enhanced at the vHSs. By estimating the DoS for the supercurrent carried only by the bulk, we show a good agreement of it with the theoretical calculation. We conclude, that in this device the edges are less affected by the superlattice potential, probably due to edge disorder or chemical doping. We show further, that one can use electrostatically defined FP cavities to determine the charge carrier type in a two terminal configuration. Close to the sDP, reappearing of oscillations in the ppp regime similar to the ones observed in the pnp regime points into the direction of a change of the charge carrier type inside the cavity, namely form holes to electrons, when the Fermi energy crosses the vHs.

4

4.A. Supporting Informations

$R_n I_c$ for device one

Here, we show R_N and I_c as a function of backgate voltage for all four junctions of device one (see Fig.4.15 a-d).

Figure 4.15. Normal state resistance and critical current for junctions B,C,D,and E of device one as a function of backgate voltage.

Further we show the calculated product of $R_N I_c$, which is proportional to the Thouless energy. The results are plotted in Fig.4.16. A sudden change of $R_N I_c$ is observed around the vHSs.

This product was as well used in Eq.4.3 to calculate the DoS. As described above this is possible due to the long and diffusive character of the Josephson junctions. The a priory unknown proportionality factor α and R_c are taken as fitting parameters, which were adjusted to fit the theoretically calculated DoS. The obtained values are summarized in Tab.4.2.

Note that this calculated DoS is obtained by setting some parameters that we cannot determine experimentally and may be altered by the disorder in the sample. For these reasons, added to the fact that our measurement of I_c is not reliable close to the CNP, the agreement is more qualitative than quantitative.
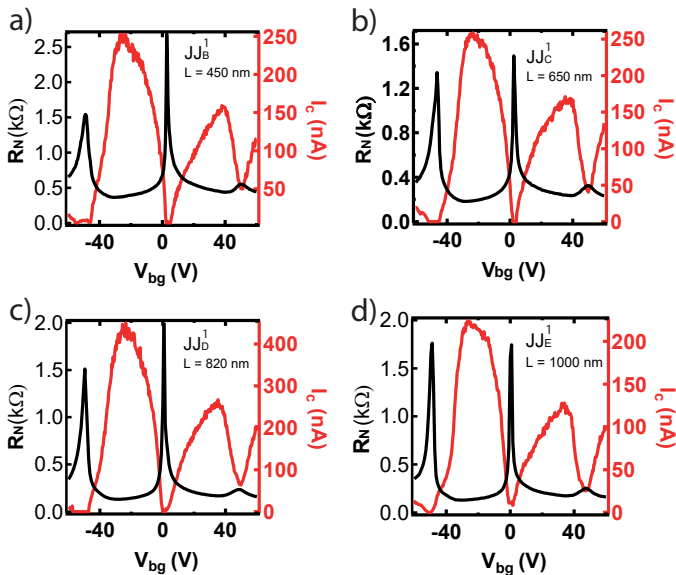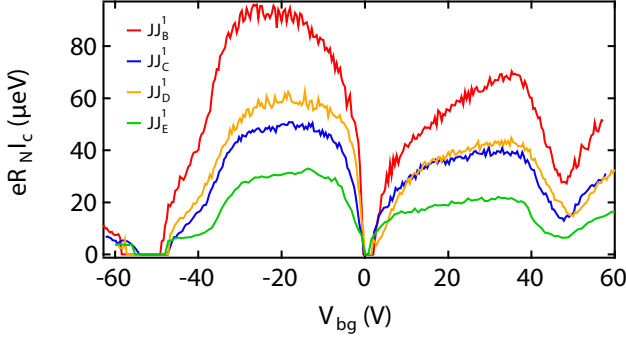
Figure 4.16. Normal state resistance and critical current for junctions B,C,D,and E of device one as a function of backgate voltage.

Consequently, we estimate the uncertainty on the given values of α and R_c to be of the order of 10%.

Switching/critical current

In a finite temperature measurement, one doesn't measure exactly the critical current of the Josephson junction but rather what is called a switching current, resulting from the thermal activation of the switching to the non-superconducting state. This point is important for the estimation of DoS as described in the main text, where we assumed that the measurement represented the real critical current. To quantify this thermal effect, we use the resistively and capacitively shunted junction (RCSJ) model. It consists in modelling the Josephson junction as a perfect Josephson element with a sinusoidal current-phase relation $I = I_c \sin(\varphi)$ (for diffusive graphene, this is a reasonable assumption), in parallel with a resistance and a capacitor. The whole system is biased by a current I and V is the voltage across it.

Using the Josephson relation $\frac{d\varphi}{dt} = \frac{2eV}{\hbar}$ and Kirchhoff's current law, we write [28]:

$$\frac{d^2\varphi}{dt^2} = -\omega_p^2 \sin(\varphi) + \omega_p^2 \frac{I}{I_c} - \frac{\omega_p}{Q} \frac{d\varphi}{dt} \qquad (4.6)$$

with $\omega_p = \sqrt{2eI_c/\hbar C}$ and $Q = \omega_p RC$. This is formally the equation of motion of a particle, whose position is given by φ, in an effective potential (Fig. 4.17):

$$U(\varphi) = -E_J \cos(\varphi) - \frac{\hbar I}{2e}\varphi \qquad (4.7)$$

and subjected to a frictional force $\frac{\hbar}{2e}^2 \frac{1}{R} \frac{d\varphi}{dt}$, with $E_J = -\frac{\hbar}{2e} I_c$.
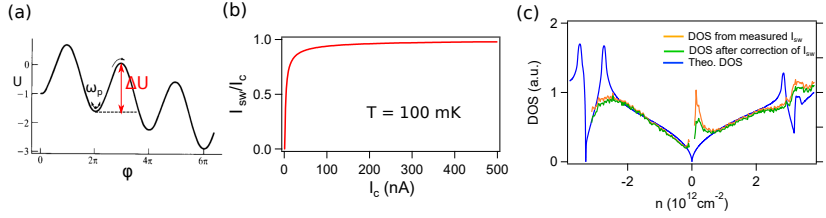
Figure 4.17. (a) The phase dynamics is equivalent to the movement of a particle in the effective potential U, and submitted to a frictional force (see text). This potential is a cosine, tilted proportionally to the current I. (b) Ratio between the estimated switching current and the critical current as a function of the critical current. This ratio corresponds to the current at which the switching probability reaches 0.5. (c) DoS extracted from the measurement of R_N and I_c for junction D (see main text). In orange, the value of I_c used is the one directly measured, the switching current I_{sw}. In green, the switching current has been corrected using the ratio plotted on fig. (b) to obtain the real I_c. In blue is recalled the DoS theoretically expected.

At zero temperature $T = 0$, while $I < I_c$, the phase is trapped in a local minimum of potential, where it oscillates at frequency ω_p. When the current is increased to $I = I_c$, there is no barrier preventing the phase from increasing leading to a rapid onset of voltage $V = \frac{\hbar}{2e}\frac{d\varphi}{dt}$ across the junction. The current becomes dissipative.

At finite temperature, thermal activation allows the fictitious particle to leave its local potential minimum for $I < I_c$. This current at which the particle tunnels across the barrier while increasing I is called the switching current I_{sw}, and is always lower than the critical current. To estimate the ratio between the measured switching current and the "real" critical current, we calculate the barrier [169]:

$$\Delta U = \frac{\hbar I_c}{2e}\left(\frac{I}{I_c}(2\sin^{-1}\frac{I}{I_c} - \pi) + 2\cos(\sin^{-1}\frac{I}{I_c})\right) \qquad (4.8)$$

According to Arrhenius law, the probability of switching (i.e. the probability of overcoming the barrier) is then $P_{sw} = e^{-\Delta U/k_B T}$ [170]. For each value of I_c, the value of the current needed to reach a switching probability of 0.5 has been extracted, and is plotted on Fig. 4.17 b for an estimated electronic temperature of 100 mK corresponding to our measurements. We see qualitatively that, if the critical current is higher than 30 nA, this ratio is roughly constant.

To figure out to what extent the temperature affects our conclusions, we plot on Fig.4.17 c a figure similar to Fig.4.7 of the Ch.4, where we compare the

DoS extracted from the measurement with and without taking into account the finite temperature. Far from the Dirac points, the difference between the two quantities is very tiny, below the uncertainty of the measurement. This is why, in the main text, we used the measured current without applying any correction and called it I_c. At the CNP, where the supercurrent cancels, temperature effect may explain the unexpected increase of the DoS, even though our simple model is not able to explain it fully.

Note that, in this qualitative estimation of the effect of finite temperature, we neglected the influence of quantum macroscopic tunnelling [171] and assumed that the sweep velocity of the bias current was infinitely slow.

4

5 **Helical states in graphene van der Waals heterostructures**[1]
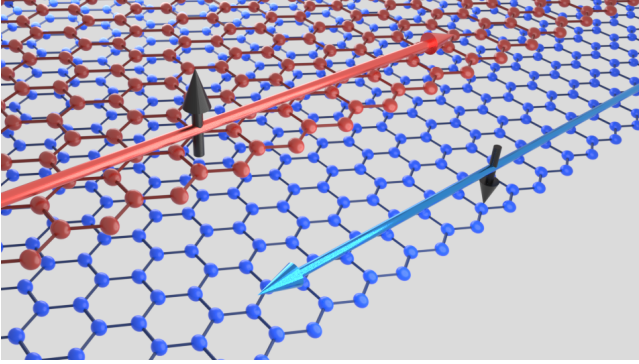
Two-dimensional systems that host one-dimensional helical states are a potential route for scalable topological quantum computation when coupled with a superconductor. Graphene is particularly promising thanks to its high electronic quality, versatility in van der Waals heterostructures and its electron and hole-like degenerate zeroth Landau level. In this chapter, we study two graphene based systems hosting helical quantum Hall states at their edges. These edge states were then tried to be coupled to superconductors in a Josephson junction geometry. Even though superconducting correlations in the quantum Hall regime could have been expected, we show that so far no signature of supercurrent at large magnetic fields was observed, which opens up the discussion for possible reasons and motivation for further investigations.

5.1. Introduction

The coupling of one-dimensional (1D) helical states to a superconductor is expected to generate zero energy Majorana bound states [100, 172, 173], which are potential candidates for topoligical quantum computation [172, 174, 175]. Currently, the most popular approach to engineer Majorana zero modes is to use 1D semiconducting nanowires with large spin orbit coupling in contact with a superconductor exposed to large magnetic fields [102–105]. However, braiding of Majorana fermions is a necessary component to perform quantum computation operations [176]. This exchange is usually difficult to realize in 1D system due to the constrain on the magnetic field direction and device dimension, such that special device geometries may be needed [177]. Therefore, 2D systems may be necessary to realise scalable architectures for topological quantum computation, and some efforts have been made in this direction using semiconducting quantum well structures [117, 145, 178, 179] hosting naturally a quantum spin Hall state. Nevertheless, these materials are difficult to fabricate and often suffer from a bulk contribution to the current transport [180, 181]. Graphene, on the other hand, exhibits extremely high electronic quality and can be assembled into versatile heterostructures along with other van der Waals (vdW) materials to create novel device characteristics [182].

Graphene, by itself, is neither a topological insulator nor does it posses helical states at zero magnetic field. However, engineering of helical states has been achieved by creating vdW heterostructures from graphene. Previous experiments have shown the manifestation of this state by applying large magnetic fields up to 30 T to increase the Zeeman energy [97], by gating large angle twisted bilayer graphene to opposite filling factors of ± 1 [99], or by using $SrTiO_3$ with its large dielectric constant as a substrate to screen the long range Coulomb interactions [98]. All these approaches rely on the electron and hole-like, four fold (spin and valley) degenerate 0th Landau level in graphene. In the quantum Hall (QH) regime, the ground state at charge neutrality is determined by the splitting of the four-fold degenerate Landau level into spin or valley polarised states, which depends on the details of the interaction terms [90, 91, 93, 183, 184] (see Sec.2.3.3). Another necessary component towards topological superconductivity is the coupling of the helical states to a superconductor in such a way, that an electron (hole) propagating forward in one state is reflected as a hole (electron) propagating backwards in the other. That superconducting correlations can exist in the QH edge states of a single layer graphene, has been recently reported [106, 108, 115].

Here, we follow the approach of two decoupled graphene layers tuned to opposite filling factors of ± 1 to create a helical state (see Fig.5.1 a). As we will discuss, this was realized in a double layer graphene (DLG) heterostructure, where a thin hBN spacer decouples the two layers electrically and in a large angle twisted bilayer graphene (tBLG), where a large momentum mis-

match in the Brillouin zone causes the decoupling of the layers [185]. The two graphene layers in both heterostructures are electrically shorted by common 1D molybdenum-rhenium (MoRe) side-contacts defining two terminal Josephson junctions (JJ). With a global top and a global back gate the electron density in both graphene layers can be controlled independently and therefore also their resistance. The interlayer capacitance is given by the thickness and the dielectric constant of the dielectric. In the case of the DLG heterostructure both quantities are know and therefore it can be calculated directly, while for the tBLG it can be extracted experimentally from the top (V_{tg}) and the back (V_{bg}) gate voltage dependence of the charge neutrality points (CNP) of the two graphene layers. At large magnetic field LL are formed and we observed a conductance plateau of $2e^2/h$ in the DLG and the tBLG device, where e is the elementary charge and h the Plank constant. This plateau corresponds to counter propagating edge channels with an opposite spin polarization. This helical state is realized by tuning the layers to opposite filling factors of ± 1.

We investigate the transport properties of this state in dependence of the bias current. If a superconducting correlation between the counter propagating QH states exists, the resistance around zero bias should be suppressed [108]. This behavior was not observed in none of the structures, even though the interlayer spacing is comparable or smaller [120] than the superconducting coherence length of MoRe (ξ_{MoRe}=10-20 nm [186]). In the end, possible reasons for the absence of superconducting correlations and potential device improvements are discussed.
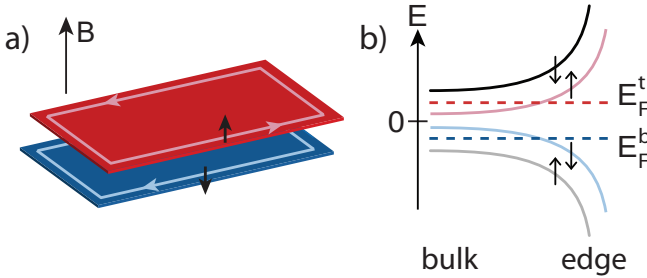
Figure 5.1. a) Schematic drawing of a double layer graphene device. The top graphene layer (red) carries a electron like edge channel with a spin up polarization. This corresponds to a filling factor of 1. The bottom layer (blue) hosts a hole like channel with a spin down polarization, which corresponds to $\nu = -1$. b) Schematic drawing of the 0th LL, when all the degeneracies are lifted. The E_F of the top (bottom) layer is drawn by a red (blue) dashed line. It crosses the state with ν=1 (-1) at the edge.

5.2. Device structure and fabrication

The DLG as well as the tBLG van der Waals (vdW) heterostructure was stacked using a standard polycarbonate assisted pick-up technique [129], which is described in Ch.3. The full encapsulation in hBN protects the graphene from contaminations during the fabrication. While in the DLG a hBN was stacked between the two graphene layers for their decoupling, a large angle between the graphene layers had to be created in the tBLG. This was realized by the so called tear and stack method [127, 130, 148]. This relies on the strong vdW forces between hBN and graphene. After the pick-up of the first half of the graphene the stage was rotated by ∼30° before the second half was picked-up as well (see Sec.3.1.3). Self-aligned 1D side-contacts were fabricated by etching the hBN away with CHF_3/O_2, before MoRe was sputtered (see App.A). Like this, JJs were realized with the DLG and tBLG as a weak link. After shaping the mesa, an aluminium-oxide (Al_2O_3) layer was grown over the entire structure in a atomic layer deposition process. This Al_2O_3 acts as an insulator between the global metal top gate and the rest of the device, e.g. the contacts (see Fig.5.4 a). The global top gate in addition to the global back gate allows to control the electron density (n) of both layers separately, as it will be shown in the next section, where the normal state resistance of both devices is characterized.

5.3. Normal state resistance

The resistance of single layer graphene as a function of gate voltage exhibits a peak around the charge neutrality point (CNP), where $n = 0$. In the case of DLG and tBLG we expect therefore a peak, when both layers are at their CNP, and two lines of increased resistance as a function of top (V_{tg}) and back gate voltage (V_{bg}), which correspond the CNP of one or the other graphene. The electron density of each layer is affected by both V_{tg} and V_{bg}, due to capacitance between the two graphene layers and between the gates. First we will show, that by knowing the interlayer capacitance the gate voltages can be converted into an electron density of the top (n_t) and the bottom (n_b) graphene layer using the electrostatic model described in Sec.3.3.1. From the density dependence we estimate the mobility and the contact resistance for the DLG JJs and show the appearance of Fabry-Pérot oscillations. In a second step we measure the resistance of the tBLG JJs. From the splitting of the CNPs as a function of gate voltages we estimate an interlayer capacitance of $7.5\,\mu F/m^{-2}$, which is similar to the previously found values [185, 187]. Furthermore, a line of increased resistance at large gate voltages indicates the existence of a moiré superlattice as discussed in previous chapters.
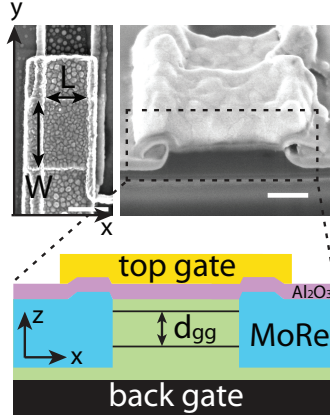
Figure 5.2. SEM images of a DLG SQUID with a schematic of the cross-section. The image on the top left shows the top view of J_1^{DLG} lying in the xy-plane with a length of 580 nm and a width 1 μm. Scale bar is equal to 500 nm. On the right a cross-section of the J_1^{DLG} with a d_{gg} of 12 nm. The sample is cut parallel to the x axis. Scale bar represents 200 nm. The schematics on the bottom shows a sketch of the cross-section. The thin (thick) black lines corresponds to the graphene (graphite gate), the green areas to the hBN, blue to the MoRe contacts, pink to the Al_2O_3 and yellow to the gold top gate.
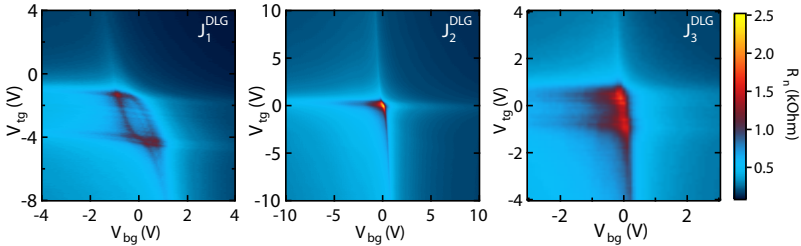
Figure 5.3. R_n as a function of top and back gate voltages for J_1^{DLG}, J_2^{DLG}, and J_3^{DLG}.

93

5.3.1. Characterization DLG device

Now we will characterize the transport properties of the DLG device. Since the DLG JJs are contacted by superconducting electrodes, R_n was measured at a constant voltage bias of 4 mV over the junctions, which is well above 2Δ, where Δ=1.25 meV is the superconducting gap of MoRe [57]. At this voltage bias the current is only carried by quasi particles and any influence of the superconductivity of the contacts can be neglected. The R_n for three junctions as a function of top gate voltage (V_{tg}) and back gate voltage (V_{bg}) is shown in the Fig.5.3. Lines of an increased resistance correspond to the CNPs of one of the layer. For J$_1^{DLG}$ and J$_3^{DLG}$ we observe two DPs in a cut along V_{tg} (see Fig.5.3 a and c), while for J$_2^{DLG}$ only one peak exists. We attribute this behavior to a laterally inhomogeneity of residual charge carriers in the top graphene layer in J$_1^{DLG}$ and J$_3^{DLG}$. Since the two lines of increased resistance have the same dependence on the gate voltages, we exclude the possibility of inhomogeneous gating, which would result in different lever arms, i.e. a different slope of the CNP lines. The splitting of the CNP as a function of the back gate voltage (V_{bg}) around charge neutrality (see Fig.5.3 a) can then be explained by the different offset doping, which results in a different screening of the top gates electric field. For J$_2^{DLG}$, this behavior is less pronounced, but the CNP of the top graphene is broadened in n_t compared to the CNP of the bottom graphene with respect to n_b. Since the V_{tg} dependence is the most homogeneous for J$_2^{DLG}$, R_n measured as a function of V_{tg} and V_{bg} is plotted as a function of n_t and n_b for this junction (see Fig.5.4 a) using the capacitance model described in Sec.3.3.1). We assumed the dielectric constant hBN to be 4 [188] and the one of Al$_2$O$_3$ to be 8.5 [189].

Two clear lines of enhanced resistance at n_t and n_b equal to zero, corresponding to the CNPs of the individual layers, split the $R_n(n_b, n_t)$ into four quadrants. The quadrant with the overall smallest resistance is the one when both layers are electron (n) doped (top right), while we observe an overall higher resistance in the quadrant, where both layers are hole (p) doped (bottom left). This is the result of the workfunction mismatch between graphene and MoRe, which dopes the graphene near the contacts to n-type [85]. This pn-junction at both electrodes, when the graphene layer is p-doped, also leads to a charge carrier dependent reflection probability, i.e. Fabry-Pérot oscillations, if the mean free path (l_{mfp}) is larger than the junction length (L)[79, 85]. For a higher visibility of the oscillations, the derivatives of R_n with respect to n_b and to n_t are shown in Fig.5.4 a. As described in Sec.4.3.2 the cavity length (L_c), i.e. the size of the p-doped region, at large n_t and n_b is extracted from the location of neighbouring resistance maxima in charge carrier density using Eq.4.2 [83]. We obtain a length of around 550 nm. The comparison to the designed junction length L=650 nm of J$_2^{DLG}$ indicates that the n doped region at each contact is of the order of 50 nm for large densities. To

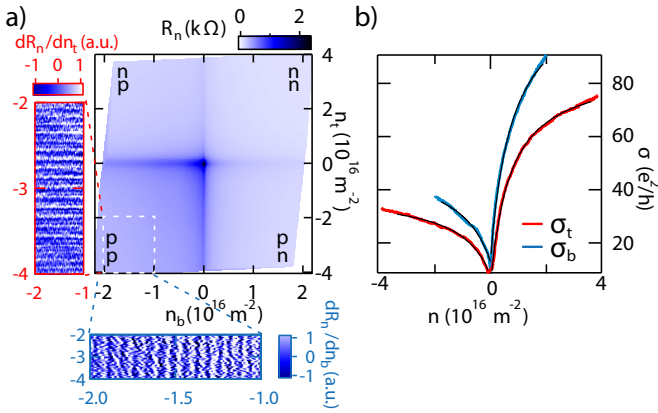**Figure 5.4.** a) R_n of J_2^{DLG} as a function of top and bottom electron density. The red (blue) framed graph shows the derivative of R_n in the white dashed enclosed region with respect to n_t (n_b). b) Cuts of the R_n measurements at $n_t = 0$ (blue) and $n_b = 0$ (red) are shown. The black lines are fits of Eq.2.29, which relates the conductivity to n as a function of the mobility and contact resistance.

determine the mobility (μ) and the contact resistance (R_c) of the junction, we calculate the conductivity σ and extract the values in dependence of n_t for $n_b=0$, respectively n_b for $n_t=0$. The conductivities are plotted in Fig.5.4 b and were fitted by Eq.2.29. From the fit we obtain an electron mobility of around 53'000 cm^2/Vs (33'000 cm^2/Vs) and a hole mobility of around 27'000 cm^2/Vs (14'000 cm^2/Vs) for the bottom (top) graphene. A R_c of 170 Ω (190 Ω) and 440 Ω (490 Ω) is extracted for the bottom (top) graphene for the n-doping and the p-doping, respectively. The relatively high μ values and the observation of Fabry-Pérot oscillations indicate ballistic electron transport in both graphene layers with the l_{mfp} larger than L.

5.3.2. Interlayer capacitance of tBLG

We measured the R_n for two JJs with a tBLG as weak link, but instead of applying a large bias voltage to overcome any influence of the superconductivity of the contacts, the sample was heated to 10 K, which is well above the critical temperature ($T_c = \sim 8$ K) of MoRe. The normal state resistance as a function of V_{tg} and V_{bg} for junction one (J$_1^{tBLG}$) with $L=250$ nm and junction two (J$_2^{tBLG}$) with $L=650$ nm is shown in Fig.5.5 a and b, respectively. Several lines of increased resistance are observed. The one indicated by the green arrow in Fig.5.5 a corresponds to the gate voltages, where the two layers have low charge carrier density, i.e. are close to charge neutrality. The resistance is the largest around zero gate voltages, where the E_F of both layers is tuned to their CNPs. At high positive and negative gate voltages two parallel lines appear, pointed out by the white arrows. These are due to a moiré superlattice between the top hBN and the top graphene, which modifies the graphenes band structure [23] as discussed in Ch.4 and leads to the existence of satellite DPs. The orange dashed line in Fig.5.5 a shows an increased resistance, which strongly depends on V_{bg}. We attribute this observation to a difference of the top gates lever arm between the bulk and the contact regions of the tBLG. Close to the contacts the lever arm is reduced due to the profile of the MoRe contacts (see Fig.5.2), which leads to a upwards bending of the top gate at the contacts. Therefore, V_{bg} dominates the charge carrier concentration in the contact region of the tBLG. The same feature is observed for J$_2^{tBLG}$ (see Fig.5.5 b). It is less pronounced due to the longer junction length, such that the overall resistance is more dominated by the bulk.

By taking a closer look at the line of enhanced resistance around the CNPs (green arrow), one observes as for the DLG device a splitting of the line of increased resistance corresponding to one ore the other layer being at charge neutrality (see Fig.5.5 c & d). This splitting is way less pronounced as in the DLG case since the interlayer capacitance is way larger, due to the small interlayer distance. The opposite sign of V_{tg} and V_{bg} leads to an electric field, i.e. a displacement field ($D = \frac{e(n_t - n_b)}{2}$), between the two graphene layers,
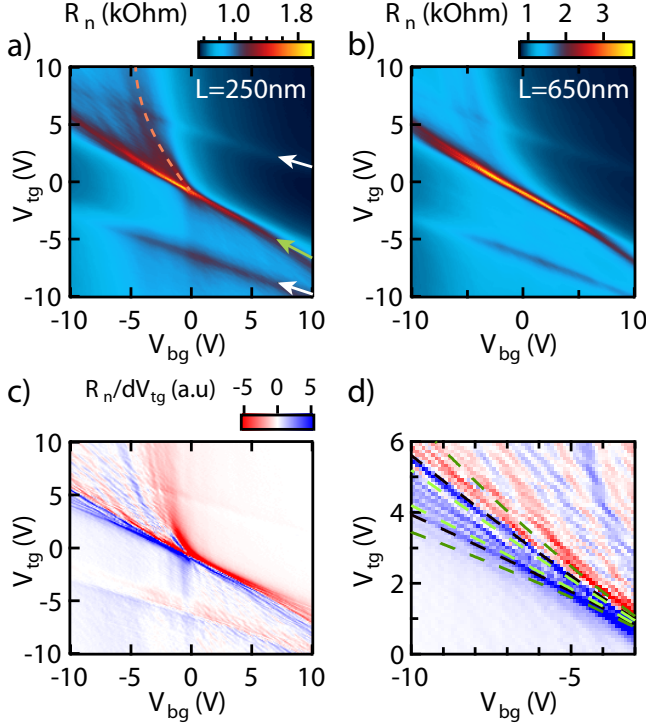
Figure 5.5. a) Resistance of J_1^{tBLG} measured as a function of top and back gate voltage at $10\,\mathrm{K}$. The green arrow indicated the line were both graphene layers are doped close to charge neutrality. The white arrows are pointing at lines of increased resistance corresponding to satellite DPs due to the existence of a hBN-graphene moiré superlattice. The orange dashed line indicates the dependence of the DP of the tBLG graphene close to the MoRe contacts. b) Resistance of J_2^{tBLG} measured as a function of top and back gate voltage at $10\,\mathrm{K}$. c) Derivative of R_n shown in a) with respect to V_{tg}. d) Derivative of R_n shown in a) with respect to V_{tg} for negative values of V_{bg}. The dashed light green, black, and dark green lines correspond to the position of the CNPs of the top and bottom graphene layers for an interlayer capacitance of $5\,\mu\mathrm{F/cm}^{-2}$ (dark green), $7.5\,\mu\mathrm{F/cm}^{-2}$ (black), and $10\,\mu\mathrm{F/cm}^{-2}$ (light green) for $n_b = 0$ and for $n_t = 0$, respectively.

such that $n_t \neq n_b$. The difference in n_t and n_b increases with an increased D and therefore the separation of the CNPs in gate-gate voltages is larger for

large gate voltages as a consequence. In Fig.5.5 d the derivative of R_n with respect to V_{tg} is shown. The red (blue) color indicates negative (positive) changes in R_n, which is used to determine the position of the CNP of the top and bottom graphene layer. From the evolution of the DPs we estimate the interlayer capacitance between the two graphene layers. For this we calculated the charge neutrality lines once for $n_t = 0$ and once for $n_b = 0$ as a function of gate voltages using the equations:

$$
\begin{aligned}
V_{bg} = {} & \frac{\mathrm{sgn}(n_b)\sqrt{\pi}\hbar v_F}{e}\sqrt{|n_b|} + \frac{en_b d_b}{\epsilon_0 \epsilon_r^{hBN}} \\
& - \frac{\sqrt{\pi}\hbar v_F d_b c_{gg}}{e\epsilon_0 \epsilon_r^{hBN}}\left(\mathrm{sgn}(n_t)\sqrt{|n_t|} - \mathrm{sgn}(n_b)\sqrt{|n_b|}\right).
\end{aligned}
\tag{5.1}
$$

$$
\begin{aligned}
V_{tg} = {} & \frac{\mathrm{sgn}(n_t)\sqrt{\pi}\hbar v_F}{e}\sqrt{|n_t|} + \frac{en_t d_t^{eff}}{\epsilon_0 \epsilon_r^{hBN}} \\
& - \frac{\sqrt{\pi}\hbar v_F d_t^{eff} c_{gg}}{e\epsilon_0 \epsilon_r^{hBN}}\left(\mathrm{sgn}(n_b)\sqrt{|n_b|} - \mathrm{sgn}(n_t)\sqrt{|n_t|}\right),
\end{aligned}
\tag{5.2}
$$

where v_F is the Fermi velocity of graphene, d_b is the thickness of the bottom hBN, while d_t^{eff} is the effective thickness of the top dielectric consisting of the hBN, Al_2O_3, and the interlayer capacitance is given by c_{gg}. This equation arise from the same derivation as discussed in Sec.3.3.1 by replacing the hBN based interlayer capacitance by c_{gg}. The best agreements is found for a $c_{gg} = 7.5\,\mu F/cm^{-2}$. This result is plotted as black dashed lines in Fig.5.5 d. In addition we show the results for $c_{gg} = 5\,\mu F/cm^{-2}$ (dark green) and $c_{gg} = 10\,\mu F/cm^{-2}$ (light green) for comparison. Never the less, the extracted value of $7.5\,\mu F/cm^{-2}$ is in good agreement with the values published for large angle tBLG [185, 187]. Note, that this capacitance is about 50 times larger than the interlayer capacitance of the DLG device and as a consequence the splitting of the CNPs is less pronounced.

Using the knowledge of independent control of each layers charge carrier density, we proceed to investigate helical states in the presence of out-of-plane magnetic fields in the DLG and the tBLG structure.

5.4. Helical states in graphene based vdW heterostructures

At large out-of-plane magnetic fields, the four-fold spin and valley degeneracy of the 0th LL is lifted in the DLG and the tBLG devices. Besides an insulating ground state at zero energy, conductance plateaus of $2e^2/h$ at $\nu \pm 1$ arise and correspond to two counter propagating edge channels. These channels are spin polarized and form a quasi 1D helical state delocalized over the two graphene layers.

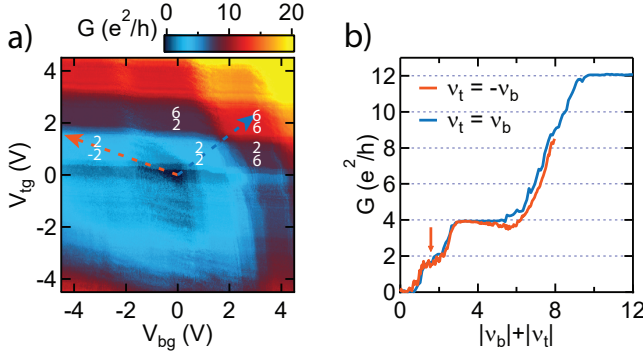## 5.4.1. Helical states in double layer graphene

Figure 5.6. a) Conductance as a function of top and back gate. Clear plateaus of constant conductance are observed. The white numbers indicate the filling factors of the top (upper number) and bottom (lower number) graphene layer within the conductance plateau. b) Cuts of the conductance map shown in a) along equal $n_b = n_t$ (blue) and opposite $n_b = -n_t$ with $n_t > 0$ (orange) as a function of the sum of the absolute filling factors.

To explore the presence of the engineered helical state in the DLG device, we measure the conductance (G) in an out-of-plane magnetic field of 5 T (see Fig.5.6 a). By voltage biasing J_2^{DLG}, well defined conductance plateaus arise as a function of V_{tg} and V_{bg}, visible as regions of well defined homogeneous colors in Fig.5.6 a. In the QH regime the current is carried by a discrete number of edge channels and the number of channels is given by the filling factor [190]. For hBN separated double layers of graphene, the edge channels of the two layers can be counted independently, and G of each plateau is given by the sum of the absolute filling factors in both layers, $G = \frac{e^2}{h}(|\nu_b| + |\nu_t|)$ with $\nu_i = \pm 2, \pm 6, \pm 10, ...$, when none of the degeneracies is lifted, where i is the index for the bottom or the top layer. For increasing but equal charge carrier density in both layers ν_{tot}, defined as $|\nu_b| + |\nu_t|$, is equal to 4,12,20,... In Fig.5.6 b the blue curve corresponds to the cut along $\nu_t = \nu_b$, where the edge channels in the two graphene layers are electron like and propagate in the same direction. We observe plateaus at $4\frac{e^2}{h}$, $12\frac{e^2}{h}$ and $20\frac{e^2}{h}$ as expected. Exceptionally, an additional plateau with $G = 2\frac{e^2}{h}$ exists, which appears due to high quality of the device, that leads to a degeneracy lifting of the 0th Landau level due to many-body correlation [89]. This plateau corresponds to $\nu_{tot} = 2$ with $\nu_t = \nu_b = 1$ meaning that two electron like edge states propagate in

the same direction, one in each layer. The same value of G is observed for $\nu_t = -\nu_b$ with $\nu_t > 0$, but in this case the top layer is electron doped while the bottom is hole doped creating counter propagating edge channels in the two layers. The presence of an insulating ground state at charge neutrality and the lifting of the valley and spin degeneracy indicates that edge channels for $\nu = 1$ and $\nu = -1$ are spin polarized with opposite spins, and together form a 1D helical state [99], which is delocalized over the two graphene sheets by a distance given by the hBN spacer between the layers.

5.4.2. Helical states in tBLG

The transport properties of J_2^{tBLG} at large out-of-plane magnetic field ($6\,T$) was probed by applying a voltage bias. We observe well defined plateaus of constant conductance as function of V_{tg} and V_{bg} as shown in Fig.5.7 a. In this figure we also marked the lines along which $\nu_{tot} = 0$ (red dashed line) and where $\nu_t = \nu_b$ (blue dashed line), which divide the gate-gate map in four quadrants labelled as $I - IV$. As in the case for DLG, the conductance value is in general given by the sum of the filling factors. The conductance plateaus are spread out parallel to $n_{tot} = 0$, which means that n_{tot} is constant on each plateau, but the individual filling factors of each layer are may changed by the displacement field. A schematic drawing of the possible combinations of ν_t and ν_b is shown in Fig.5.7 b). The conductance in quadrant I and III are equal to $2e^2/h$, $4e^2/h$, and $12e^2/h$. In the quadrants II and IV the plateaus are less pronounced and do not match the expected magnitude for a constant ν_{tot}. As discussed in Sec.5.3.2 the electron density in the tBLG differs at the contacts from the electron density in the bulk attributed to a inhomogeneous gating. This results in a pn-junction at the contacts over a large gate range in these particular quadrants. The QH edge states at the pn-junctions are co-propagating and mix depending on their spin [93, 191, 192] and valley [83] polarization, which gives rise to a deviation of the expected sequence. An equilibration of the edge states can also take place in the unipolar regime, when electron density in the bulk is larger than close to the contacts, which leads to circulating states in the bulk connecting the tow edges [193].

Now we focus on the line, where $\nu_{tot}=0$ and therefore $\nu_t = -\nu_b$ and therefore the edge channels of the top and bottom graphene layers are counter propagating. A cut of Fig.5.7 a along the red dashed line ($\nu_{tot} = 0$) is shown as an inset. At charge neutrality ($V_{bg} = 0.4\,V$ and $V_{tg} = -1.2\,V$) the junctions conductance goes below e^2/h. At $\nu_t = \nu_b = 0$ the Fermi energies are within the gap between the electron and hole like bands of the 0th LL, which leads to an insulating state. If the displacement field is increased the conductance rises up to $2e^2/h$ before it decreases again. This decreasing of G in the bipolar regime is distinctly different from the observations in the DLG device, where we found the same sequence as for $\nu_t = \nu_b$. The explanation of this phenom-

ena can be found by taking the spin polarization and scattering between the edge channels into account. Even though, the graphene layers are decoupled in the bulk of the tBLG junction, there may exist a finite scattering probability form one layer to the other. At $\nu_{t/b} = \pm 1$ and ∓ 1 the counter propagating edge states have the opposite spin polarization. This polarization prohibits the backscattering of an electron from one layer to the other, since the spin has to be flipped. If D is increased each layer hosts two edge states, one with spin-up and one with spin-down. Therefore, an electron can now be scattered from one layer to the other without a spin flip process, which leads to equilibration of the edge channels and a reduction of G. This means in conclusion, that the $2e^2/h$ plateau arises due to a helical state formed by the first electron and hole band of the 0th LL [99].

As mentioned the creation of a helical state is only one requirement to realize Majorana zero modes in graphene. The second one is the coupling of this state to a superconductor, which we will investigate in the next section.

5.5. Superconducting correlations in the QH regime?

Superconducting correlations were observed in the QH regime for various graphene based electronics as discussed in Sec.2.4. Amet et al. [108] reported the appearance of so called superconducting pockets in the QH regime, i.e. regions in gate and magnetic field of suppressed resistance . In Fig.2.17 we show some of their findings. The superconducting pockets are attributed to the coupling of the counter propagating QH edge channels on either edge of the graphene (see Fig.2.17 c). This leads to the formation of a delocalized Andreev bound state involving a hybrid electron-hole mode along the contacts, which couples the QH channels of both edges. It has been shown that such a hybrid state indeed can exist along a graphene-superconductor interface [115], but recent findings point into the direction that the correlated states are due to inhomogeneities at the edges, such that the Andreev reflection takes place locally at the same edges, and are not caused by the Andreev reflection from one edge to the other [110, 114]. In another experiment it was shown that the QH edge states can be coupled by a superconducting electrode, which width is narrower than the coherence length of the superconductor. This leads to crossed Andreev reflection between the incoming and out going channel at $\nu = 1$ [106].

In our devices the propagation direction of the edge channels can be chosen for each layer separately, just given by their doping. Like this it is possible to create counter propagating edge states on both sides of the junction. Further, the interlayer distance is in the DLG of the same order and in the tBLG much smaller than the coherence length of MoRe of 10-20 nm [186]. Therefore, a superconducting correlation can be expected in the QH regime, when the edge
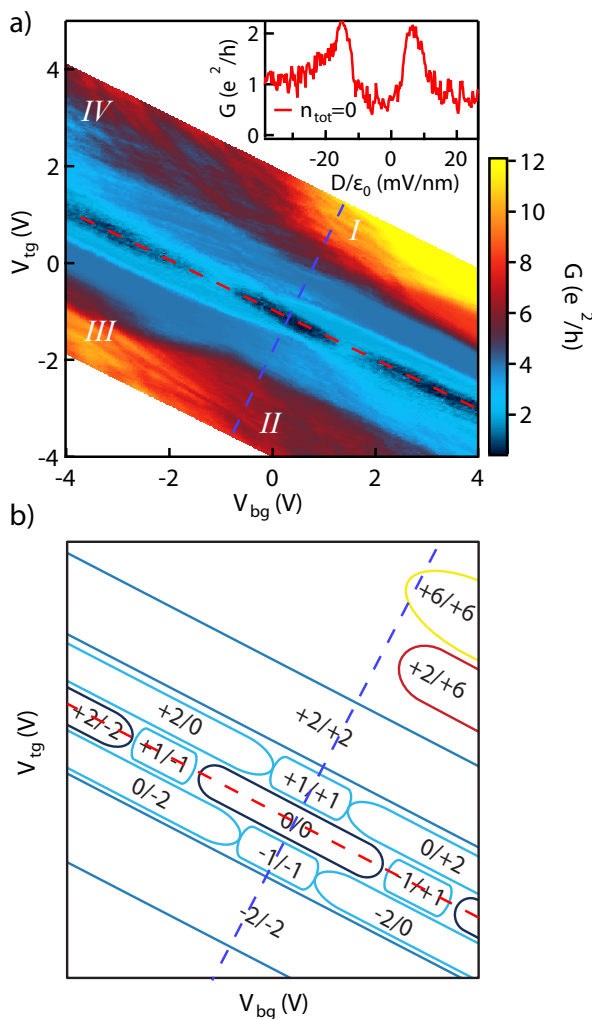
Figure 5.7. a) Conductance at $6\,\mathrm{T}$ as a function of top and back gate for J_2^{tBLG}. The red dashed line corresponds to $\nu_{tot} = 0$ and the blue dashed line corresponds to $\nu_t = \nu_b$. Inset: Conductance as a function of displacement field at $\nu_{tot} = 0$. b) Schematic drawing of the plateaus in the QH regime shown in a). The left number corresponds to the filling factor of the top layer and the right number to the filling factor of the bottom layer.

channels are counter propagating like in a helical state, which was discussed in Sec.5.4. Nevertheless, no sign of suppressed resistance was observed in neither of the samples, as will be shown in the following section. Afterwards we discuss possible explanations for the absence of of any superconducting correlations, which will need further investigations in the future.

5.5.1. Investigation of CAR in the QH regime

To observe potential superconducting correlations in the QH regime the JJs were current biased by a small ac-current of ≤ 50 pA, since the potentially expected signs of a reduced differential resistance are small (<1 nA)[108]. The measurement were taken around $\nu = \pm 1$.

Double layer graphene JJ

Fig.5.8 a to c show the results for J_2^{DLG} (d_{gg}=25 nm) and b to f the one for junction J_1^{DLG} (d_{gg}=12 nm). The magnetic field was set to 5 T, which is well below the critical magnetic field of MoRe (B_c=$\sim$8 T). The resistance was measured as a function of V_{tg} and V_{bg}, once at zero bias (see Fig.5.8 a and d) and once at a finite bias of 5 nA (see Fig.5.8 b and e). We do not observe any signs of superconducting pockets, nor any other large difference between the two measurements for any doping combination of the two layers. For comparison, line cuts of the gate-gate maps are taken and shown in Fig.5.8 c and f. The value of the resistance as a function of V_{bg} shows only minor differences in the noise level.

Twisted bilayer graphene JJ

As shown in Sec.5.4 a plateau of $2e^2/h$ was observed, which corresponds to $\nu_t = \pm 1$ and $\nu_b = \mp 1$. As discussed the edge channels are counter propagating in this regime and form a helical state. To investigate the possibility of induced superconducting correlations, we swept the top gate voltage in a finite range (V_{tg}^{range}) around $\nu_{tot} = 0$ for every V_{bg} to resolve the conductance plateau at $\nu_t = 1$ and $\nu_b = -1$. The measurements are shown in Fig.5.9 were taken at an out-of-plane magnetic field of 6 T, for which the plateau of $\nu_{t/b} = \pm 1$ was clearly observed. As for the DLG JJs we do not observe a significant difference between the dc-current biased (5 nA) measurement and the one at zero bias current measurement. Fig.5.9 c shows two measurements of the resistance at $V_{bg} = -1$ as a function of V_{tg}^{range} for different bias. For some particular values of the gate voltage we observe a significant difference in the resistance, but in contrast to the expectation, where we would expect a dip at zero bias, the measurement at 5 nA shows the smaller values. Therefore, no sign of induced correlation between the QH edge states by the superconducting contacts, even though the interlayer spacing is reduced to a minimum.
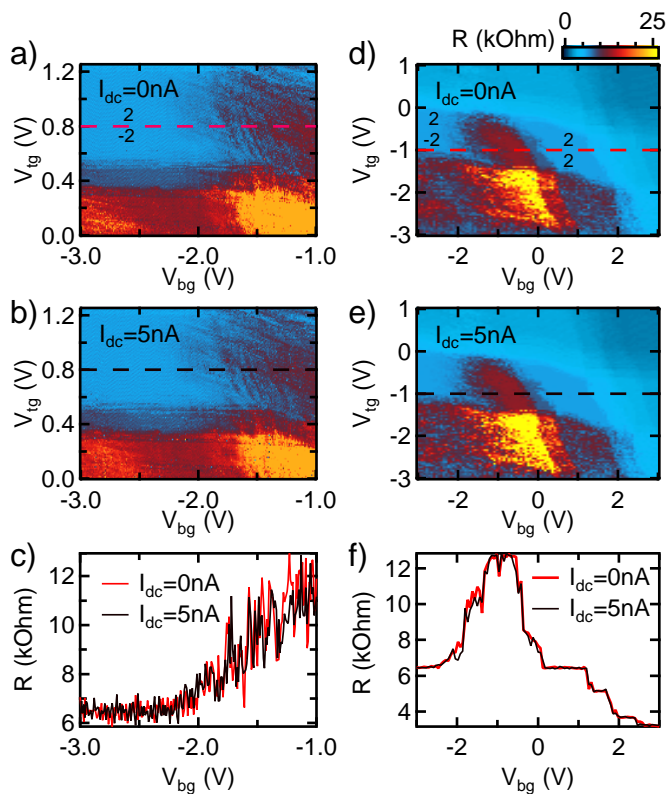
Figure 5.8. a)-b) Resistance of J$_2^{DLG}$ as a function of V_{tg} and V_{bg} at zero dc-current bias (a) and a dc-current bias of 5 nA (b). c) Resistance as a function of V_{bg}. The line cuts are taken from a and b at $V_{tg}=0.8$ V, indicated by the dashed lines. d)-e) Resistance of J$_1^{DLG}$ as a function of V_{tg} and V_{bg} at zero dc-current bias (a) and a dc-current bias of 5 nA (b). f) Resistance as a function of V_{bg}. The line cuts are taken from a and b at $V_{tg}=-1$ V, indicated by the dashed lines.

Figure 5.9. a) Resistance of JJ^2_{tBLG} as a function of V^{range}_{tg} and V_{bg} around $\nu_t = 1/\nu_b = -1$. The applied dc-current bias was 0 A. b) Resistance of JJ^2_{tBLG} as a function of V^{range}_{tg} and V_{bg} around $\nu_t = 1/\nu_b = -1$ for a dc-bias of 5 nA. c) Resistance as a function of V^{range}_{tg} for two different values of bias current. The back gate voltage was fixed at -1 V.

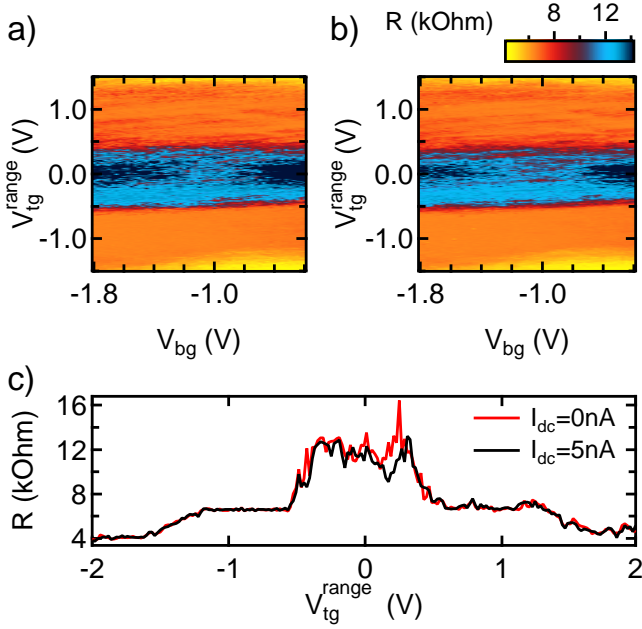## 5.6. Conclusion and Outlook

In conclusion we realized helical states in DLG and tBLG vdW heterostructure. By converting the gate voltages to electron densities using a complete electrostatic model, we extracted an estimation for the mobility and the contact resistance. The high mobility value together with the appearance of Fabry-Pérot oscillations indicate ballistic electron transport in both junctions and a high device quality. A plateau of $2e^2/h$ manifest itself in both structures in the QH regime close to charge neutrality, which corresponds to counter propagating edge states in the two graphene layers. The spin polarization can be observed in the tBLG structure, where the spin prohibits backscattering from one state to the other even though the graphene layers are placed in direct contact [99]. The investigation of superconducting correlations in the QH regime revealed that neither in the DLG JJ, where the layers are separated by a hBN with a thickness of the order of ξ_{MoRe}, nor in the tBLG JJ, where the layers are in direct contact decoupled by a twist angle induced momentum mismatch, superconducting pockets due to CAR were observed. In the case of the DLG JJ the absence of any superconducting correlations is maybe given by the fact that the interlayer spacing was still to large to couple the edge states of the two layers strongly, even though it was reduced to 12 nm. For the tBLG JJ this explanation does not hold, which rises the question, if the momentum mismatch between the layers suppresses crossed Andreev processes. In graphene it is expected that at zero field and for perfect interfaces an incoming electron is reflected as a hole in the other valley [37]. In the tBLG the only possible state is found in the same layer. The later argument can also be applied to the DLG JJ, since the structure was fabricated out of two individual graphene crystals by not knowing their alignment. For the future it would be interesting to study if the coupling of the two layers can be observed if on one side the interlayer spacing in DLG JJ is reduced and on the other side the crystallographic axes of the two graphene layers are aligned.

6 Current phase relation of long graphene Josephson junctions [1]
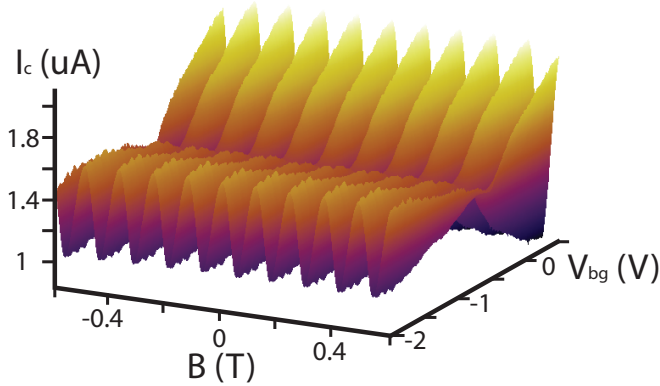
In this chapter we discuss a compact double layer graphene SQUID, which consists of two graphene layers separated by a hBN and shorted by two common superconducting electrodes. This forms two Josephson junctions in parallel. The size of the superconducting loop is therefore reduced to the interlayer distance of the graphene layers at the electrodes. We show, that it is possible to gate control the supercurrent in each graphene Josephson junction separately. This allows to change the SQUID in situ from an asymmetric to a symmetric configuration and to study its magnetic field response in both regimes. In the symmetric case the SQUID acts as a sensor for the magnetic field direction. In the asymmetric regime, it is possible to measure the current phase relation of both graphene layers and we will show that high transparent modes exist in the long, ballistic limit. This device structure and the possibility to observe the interference pattern at large, in-plane magnetic field paves the way to study crossed Andreev reflection as a function of well defined interlayer spacing given by the thinkness of the hBN spacer.

---

[1]Parts of this chapter were published in a similar form in Ref.[101]

6.1. Introduction

Two Josephson junctions (JJ) integrated in parallel into a superconducting loop form a superconducting quantum interference device (SQUID). In this work, we create a SQUID by separating two graphene layers with a thin hBN spacer. Superconducting, one-dimensional, molybdenum-rhenium (MoRe) electrodes connect the double layer graphene (DLG) and from two graphene Josephson junctions (JJ) in parallel as shown in Fig.5.2. The measurements of the normal state resistance (R_N) and in the quantum Hall regime are described in Ch.5. With global top and back gates the I_c of each layer can be individually adjusted, which opens the opportunity to change the SQUID configuration from symmetric to asymmetric in situ. In the symmetric case the SQUID is sensitive to the magnetic flux through the SQUID cross section, but as well to the flux through the graphene sheets, which makes it an ideal candidate for the calibrations of the magnetic field direction. In the asymmetric case we show that we can measure the CPR of the JJs, which reveals high transparent modes contributing to the supercurrent transport in both of layer. Further, the SQUID does not suffer from any screening of the superconducting loop, due to its small and compact structure resulting in an negligible inductance ($\ll 1\,\mathrm{pH}$).

6.2. Device fabrication

We fabricate the DLG SQUID, a six-layered van der Waals (vdW) heterostructures, shown in Fig.5.2 by a standard polycarbonate assisted pick-up technique [129]. The self-aligned MoRe side contacts were sputtered after etching the contact region with CHF_3/O_2 [125]. The hBN on the top and the bottom were used as gate dielectrics. Aluminium oxide (Al_2O_3) with a thickness of 30 nm was grown by atomic layer deposition to electrically insulate the top gate from the contacts as well as from the etched edges of the stack that define the mesa. The fabrication details can be found in Sec.3.1 and App.A. The top gate together with the global graphite back gate allows a independent control of the top (n_t) and the bottom (n_b) electron densities. These are calculated from the gate voltages by taking into account the finite capacitance between the layers and the quantum capacitance of each layer, see Sec.3.3.1. The hBN between the graphene sheets, has three atomically well defined thickness steps. Therefore, SQUIDs with different loop size were defined by the distance between the graphene layers (d_{gg}), which could be fabricated on the same vdW heterostructure. The thicknesses of the hBN were measured with an atomic force microscope before the stacking process. For junction one (J_1^{DLG}) the thickness is 12 nm, for junction two (J_2^{DLG}) it is 25 nm and for junction three (J_3^{DLG}) 50 nm. Scanning electron microscope (SEM) pictures of the top view and the cross section made by a focused ion beam after the measurements are shown

in Fig.5.2. We assign the xy-plane to the graphene plane, where the x-axis (y-axis) is perpendicular (parallel) to the edge contacts. The z-axis is defined in the direction of the normal vector of the graphene sheet.

6.3. Gate control of the total supercurrent

Next, we characterise the superconducting properties of our junctions at zero magnetic field by measuring the I_c, which is defined as the current at which the junction undergoes the transition from its zero to a finite resistance state. Figure 6.1 a shows the measured I_c for J$_2^{DLG}$ as a function of n_t and n_b. Here, I_c was measured by triggering the appearance of a finite voltage (V_{trig}) over the junction, while sweeping the bias current. For the triggering we used a FCA3000 counter (see Sec.3.4). The value of V_{trig} was set to $6\,\mu V$ to be able to measure the I_c over the entire gate range, since the smallest detectable value is given by the maximum of the resistance R_n^{CNP}, here the resistance at the CNP, and therefore $I_c^{min} = \frac{V_{trig}}{R_n^{CNP}} = 2.5\,nA$. We set V_{trig} just above the noise floor of the voltage signal, such that the measurement is sensitive to the voltage noise. This can cause random triggering events, when the noise exceeds V_{trig}, which results in a reduced, wrong value for I_c. Due to this, I_c was measured hundred times for each pair of V_{tg} & V_{bg} and only the maximum value is taken. The maximum I_c deviates not more than 10% from the mean value, which also includes the trigger errors. The critical current of the bottom (top) layer I_c^b (I_c^t) extracted at $n_t = 0$ ($n_b = 0$) shows the similar dependence of n_b (n_t) as the conductivity (see Fig.6.1 b), as expected from the Ambegaokar-Baratoff relation ($I_c \propto 1/R_n$)[46]. The observed minimum value of the I_c is around 40 nA, when both layers are at their DPs. Here, the superconducting coherence length of the Cooper pairs in graphene is given by $\xi_s = \frac{\hbar v_F}{\pi \Delta} = 160\,nm$ [28], with $\hbar$ the reduced Planck constant, and $v_F = 10^6$ m/s the Fermi velocity of graphene, which defines the JJs in the long junction regime.

6.3.1. $R_n I_c$ of J_2^{DLG}

For such a long junction ($\xi_s < L$) the product of R_n and I_c is proportional to the Thouless energy [50] instead of Δ, where E_{th} is given by $1/\tau$, where τ is the time the quasiparticles spend in the graphene, which is equal to L/v_F in the case of a ballistic JJ. The plot for $R_n I_c$ of J$_2^{DLG}$ is shown in Fig.6.2 a. We observe a constant value in each quadrant apart from the CNPs, i.e. nn, np, pn, and pp, which indicates a constant value of E_{th}. While we find $eR_n I_c$ to be a factor of two smaller than $E_{th} = \hbar v_F/L \approx 1\,meV$ when both layers are n doped (0.4 meV), its value is even reduced if they are p-doped (0.25 meV). This is likely due to reflection at the contact doping induced pn-junction, which reduces the contact transparency and causes the charge carriers to stay
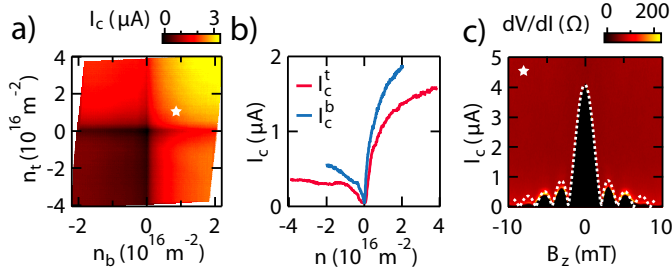
6

Figure 6.1. a) I_c as a function of n_t and n_b. b) Cuts of a) along $n_t = 0$ (blue) and $n_b = 0$ (red). c)Interference pattern of the DLG JJ as a function of out-of-plane magnetic field B_z. The white star in Fig.6.1 a indicates the position in n_b and n_t, where the interference pattern is measured. The interference pattern is overlaid with a Fraunhofer interference pattern (white dashed line) given by Eq.6.1.

longer in the graphene. Also trajectories, which are longer than L or include a reflection at the sample edges as shown in Fig.6.2 b, result in an increased dephasing of the supercurrent carrying trajectories [167]. The reduced value of E_{th} was already discussed in Sec.4.6, where we obtained similar values.

6.3.2. Josephson interference pattern in a small out-of-plane magnetic field

The I_c also depends strongly on the magnetic flux Φ threading through the JJs in z-direction, as it creates a phase difference between the different superconducting channels of the JJ. The dependence of I_c on the out-of-plane magnetic field B_z (perpendicular to graphene layers) was measured by applying a dc current over J_2^{DLG} with a ac modulation of 10 nA and detecting the differential resistance, while V_{tg} was set to 2 V and V_{bg} to 3 V. The result is shown in Fig.6.1 c. If the current distribution is homogeneous and constant along the y-axis, I_c can be expressed as a function of B_z as,

$$I_c(B_z) = I_c(0) \left| \frac{\sin(\pi\Phi(B_z)/\Phi_0)}{\pi\Phi(B_z)/\Phi_0} \right|, \tag{6.1}$$

where Φ_0 is the magnetic flux quantum given by $h/2e$ and $\Phi(B_z) = W(L + 2\lambda_L)B_z$ [28] with $\lambda_L \approx 180$ nm. Since the measured I_c is well described by this Fraunhofer like interference pattern, we conclude that the supercurrent density is indeed constant in both layers. The period of the oscillation in magnetic
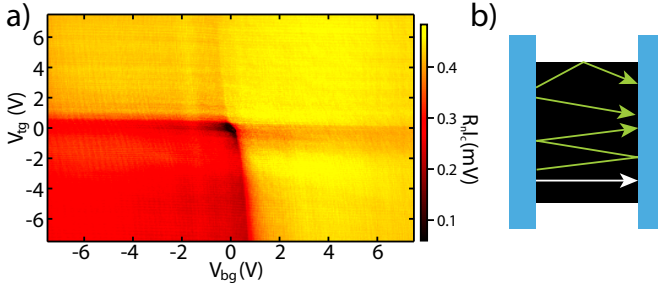
Figure 6.2. a) Product of R_n and I_c as a function of V_{tg} and V_{bg}. If both layers are n doped we observe a value of 0.4 mV. This value reduces to 0.25 mV, if both layers are p doped. b) Schematic drawing of a Josephson junction and possible ballistic trajectories of the supercurrent carrying channels. The superconducting leads are indicated by blue, while the graphene is black. The white arrow corresponds to the shortest trajectory between the leads, while scattering at the physical edge of the graphene, reflection at the imperfect contacts or a finite angle distribution can lead to increased length of the paths.

field is given by the flux through the graphene and the extracted area matches the sample dimensions.

6.3.3. Suppressed resistance in moderate out-of-plane magnetic fields

At magnetic fields large enough to suppress the supercurrent in the JJ according to Eq.6.1, but smaller than the field needed to be in the quantum Hall (QH) regime, irregular oscillations of the resistance around zero current bias are observed in J_2^{DLG} (see Fig.6.3). The gate voltages were set to V_{bg}=-1.5 V and V_{tg}=1.5 V, while the resistance as a function of out-of-plane magnetic field (B_z) was measured with a standard lockin technique. The ac-current amplitude was set to 50 pA. The appearance of these random oscillations were already observed by Ben Shalom et al.[86] and are attributed to the ballistic transport nature of the junction, which leads to billiard like trajectories at the edges of the sample. These trajectories are suspected to form irregularly Andreev states, while the ones in the bulk are fully suppressed by the magnetic field. Therefore, it is another indication of the ballistic transport nature of J_2^{DLG}. Nevertheless, these superconducting pockets disappear at fields larger than 440 mT and were not observed in the QH regime within our resolution of 50 pA, which is in contrast to Ref.[108].
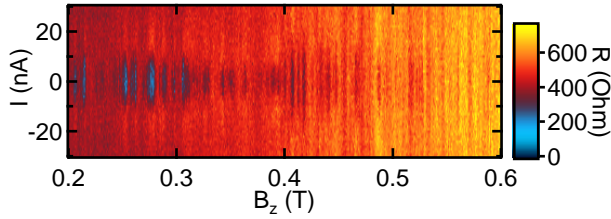
Figure 6.3. Resistance as a function of current bias and out-of-plane magnetic field of JJ_2^{DLG}. A suppression of the resistance around zero bias current was observed up to fields of 440 mT. The gate voltages were set to V_{bg}=-1.5 V and V_{tg}=1.5 V.

6.4. Symmetric SQUID

The measurements shown in Fig.6.1 can not distinguish between the currents that flow in the top or the bottom layer of the DLG. To prove the independent flow and tunability of I_c in both layers, we apply an in-plane magnetic field B_y (y-axis) and measure the SQUID response, which is sensitive to the position and the magnitude of the supercurrent, for various combinations of gate voltages. Thanks to the full gate-tunability of the supercurrents, we are able to access different regimes of the SQUID asymmetries. For this measurement, the alignment of the magnetic field is crucial, since a small out-of-plane component can lead to a fast decay of I_c (see Fig.6.1 c). The calibration of the magnetic field direction is described in the following section.

6.4.1. Calibration and alignment of the in-plane magnetic field

To measure the in-plane magnetic field dependence of such a DLG SQUID device, one has to carefully calibrate and adjust the direction of the magnetic field. The I_c is more sensitive to an out-of-plane magnetic field than to an in-plane field, due to the large ratio between the JJs area and the area of the SQUID loop, e.g. 35:1 for J_2^{DLG}. If the alignment is imperfect, which results in a finite out-of-plane component, the SQUID pattern decays due to the suppression of the supercurrent in the individual junctions given by Eq.6.1. Further we will show that also a component of the magnetic field in x-direction (see Fig.6.4 c) leads to a reduction in I_c as well.

The calibration was performed using a 3D vector magnet with the magnetic fields B_1, B_2, and B_3, which are perpendicular to each other. While the graphene plane was roughly lying in the plane of the first and second magnet with B_1 and B_2, the magnetic field of the third one is pointing out-of-plane. In

a first step we had to measure three different points, that are in the xy-plane of the sample from which one corresponds to $B = 0$. This was done by setting B_1 and B_2 to the values given in the inset of Fig.6.4 a. At each point the out-of-plane magnetic field (B_3) was swept and a Fraunhofer like interference pattern was measured. The point in B_3, where I_c is at the maximum reflects the best compensation of the out-of-plane magnetic field, i.e. correspond to a magnetic field in the plane of the JJs. With these three point we defined two vectors, which have to lie in-plane of the graphene layers. To define now a coordinate system we took the cross product of these two vectors to obtain the normal vector $\vec{n}$ of the plane. Then one of the original vectors was normalized and defined as the temporally x-axis ($\vec{e_x}$). By taking now the cross product of $\vec{e_x}$ and $\vec{n}$ we obtain the unit vector in y-direction ($\vec{e_y}$). The two unit vectors $\vec{e_x}$ and $\vec{e_y}$ span now the plane of the graphene layers and allows us to sweep the magnetic field in this plane. Note, that the direction of the defined vectors are arbitrary and not related to any alignment with the device, e.g. contacts, yet. To calibrate the magnetic field direction with respect to the device structure, we rotated the magnetic field from -360° to 360° for two different magnitudes (see Fig.6.4 b). Curves with a periodicity of 180° were observed as expected, but the origin of their shape was not fully clear in the beginning. Therefore the magnetic field direction was fixed at an angle of a maximum of either curve shown in Fig.6.4 b. By sweeping the magnitude of the magnetic field in these two direction we observed the interference pattern plotted in Fig.6.4 c and d, from which we could determine the in-plane field direction perpendicular to the SQUID (B_y). Note, that I_c also strongly depends on the magnitude of the magnetic field which is applied parallel to the SQUID's cross section, i.e. in supercurrent direction. This suppression by B_x is attributed to the Meissner effect, which expels the magnetic field out of the superconducting contact leading to a finite and inhomogeneous out-of-plane magnetic field through the graphene planes. In the direction of B_y we find the modulation of I_c typical for a SQUID. A small decay of the maximal value is observed at higher fields [194]. This can either come from a magnetic field component in x or z-direction due to an imperfect alignment or due to out-of-plane corrugations of the individual graphene layers [195–197].

6.4.2. Interference pattern in in-plane magnetic field

The in-plane field results in a magnetic flux threading through the loop formed by the two vertically stacked graphene layers and the superconducting electrodes. This flux induces a phase difference between the two JJs, given by $\varphi_t = \varphi_b + \frac{2\pi\Phi}{\Phi_0}$, where φ_t is the phase difference over the top JJ and φ_b is the phase difference over the bottom one. The interference pattern is modulated in Φ with a periodicity of $h/2e$. In general, the total supercurrent (I_s) of the
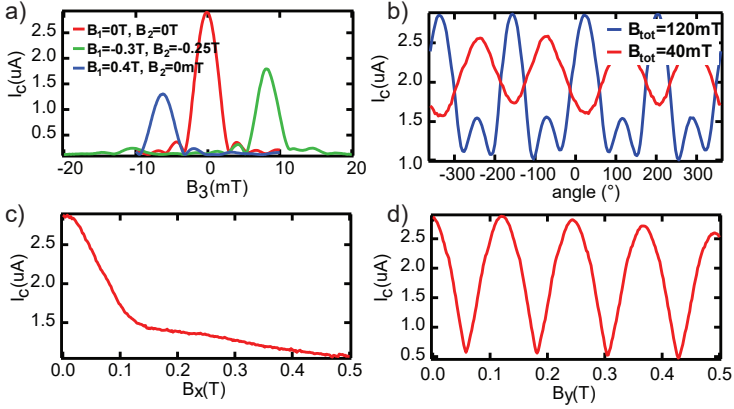
Figure 6.4. a) Critical current as a function of B_3 for three pairs of B_1 and B_2. b) Critical current as a function of the direction of the in-plane field for two fixed magnitudes of the in-plane magnetic field. c) Dependence of the critical current as a function of B_x. d) Critical current as a function of B_y.

SQUID is given by

$$I_s(\varphi_t, \varphi_b) = I_c^t f^t(\varphi_t) + I_c^b f^b(\varphi_b), \tag{6.2}$$

where f^i is the CPR of the i-th JJ and φ_i the phase drop over it. As mentioned, φ_t can be express in terms of φ_b and therefore can be replaced in Eq.6.2. The critical current as a function of Φ is obtained by maximizing $I_s(\varphi_b, \Phi)$ over φ_b for a given magnetic field.

When the two junctions form a symmetric SQUID ($I_c^t = I_c^b$), one obtains for a sinusoidal flux-dependence, i.e. $f^i = \sin(\varphi_i)$, that

$$I_c(B_y) = 2I_c^t |\cos(\pi\Phi/\Phi_0)|. \tag{6.3}$$

Indeed the measurements for all three SQUIDs formed by long JJs show a $|\cos|$ like behavior (see Fig.6.5 a), when they are tuned to $I_c^t \approx I_c^b$[146]. From the periodicity of the interference pattern in magnetic field we extract the cross sectional area, which is given by $L \times d_{gg}$, and find a good agreement with their physical size for the all three junctions [J$_1$: (580 nm×12 nm, J$_2$: (650 nm×25 nm, J$_1$: (530 nm×50 nm)]. Note, that the minimal vlaue of I_c never reaches zero, revealing a small difference between the critical currents of both layers or a non-sinusoidal CPR of the junctions. We show in the next section that even for $I_c^t = I_c^b$ the total critical current does not vanish indicating a non-sinusoidal CPR.
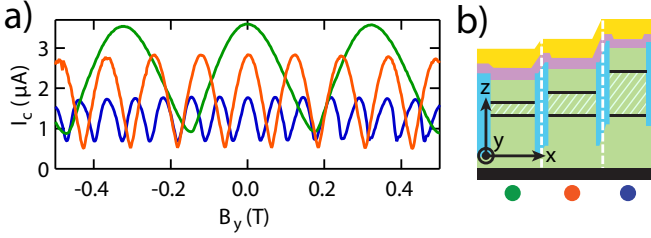
Figure 6.5. a) Interference pattern of DLG JJ as a function of in-plane magnetic field B_y. The different colors correspond to different d_{gg}. b) Schematic cross-section of the different JJ. The coloured dots are related to the interference pattern in a). The flux through the striped areas has to be considered to calculate the period in magnetic field

6.4.3. Minima of $I_c(B_y)$ as a function of V_{tg}

For a symmetric SQUID ($I_c^1 = I_c^2$) with a sinusoidal CPR, one expects a $|\cos(\pi\Phi/\Phi_0)|$ like interference of I_c versus magnetic field. Therefore one would observe that I_c fully vanishes at a magnetic flux equal to $\Phi_0/2$. But if the SQUID is not fully symmetric, the supercurrent flowing in the two JJs will not compensate each other at $\Phi_0/2$, leaving a finite I_c. A non-vanishing critical current can also arise, when the CPR is not sinusoidal, even if the JJs are symmetric. To show that the non-vanishing I_c in the interference pattern in Fig.6.5 a, is not fully due to an asymmetry of the JJ, but rather given by a non-sinusoidal CPR, we measured I_c of J_2 as a function of V_{tg}, while V_{bg} was fixed at 5 V and the in-plane magnetic field at -181.6 mT, which corresponds to a minimum of the interference pattern (see Fig.6.5). When V_{tg} is tuned, mainly the critical current carried by the top graphene layer changes. Therefore, it is possible to change between a symmetric and an asymmetric SQUID configuration. At the CNP of the top layer ($V_{tg} \approx 0$ V) the supercurrent is carried only by the bottom layer and the critical current is therefore only given by I_c^b. When the gate voltage is increased, I_c^t increases. Since there is a phase difference of roughly $\pi/2$ between the JJs due to the magnetic flux, the supercurrent flows in the opposite direction, which leads to a decrease of SQUID's I_c. This trend continues until $I_c^t = I_c^b$, where I_c will reach its minimum in V_{tg} before it starts to increase again due to opposite asymmetry ($I_c^t > I_c^b$). Note, that also for negative V_{tg} we observe a decrease of I_c, but due to the contact doping I_c^t stays always smaller than I_c^b. The non-vanishing I_c in the symmetric SQUID indicates a non-sinusoidal CPR, which is further discussed in Sec.6.5. This can be seen by taking a look at how I_c for a particular Φ is calculated. First, the total supercurrent is given by

$I_s = I_c^t f^t(\varphi_t) + I_c^b f^b(\varphi_b)$ with $\varphi_t = \varphi_b + \pi\Phi/\Phi_0$. For a given magnetic field the phase difference between the junction is fixed but not the value of φ_b. To obtain now I_c, one has to maximize I_s over φ_b. Therefore, to obtain a I_c of zero, I_c has to be zero for all φ_b. This is the case for two sine curves shifted by $\pi/2$ and is never the case if the CPRs are skewed sinusoidal functions.
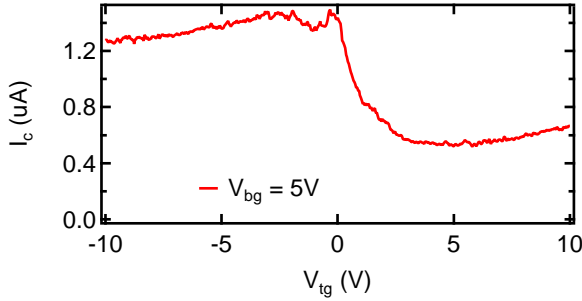

Figure 6.6. I_c as a function of V_{tg} for V_{bg}=5 V. The critical current was measured for a in-plane magnetic field (B_y) of -181.6 mT.

6.4.4. Absence of CAR

In the DLG SQUID, the interlayer distance between the graphene is in the order of the coherence length of MoRe (ξ_{MoRe}=10-20 nm [186]). It has been shown in a double bilayer graphene, that the small distance leads to a coupling of the two layers via crossed Andreev reflection (CAR), where an electron (hole) in one layer is reflected as a hole (electron) into the other one [120]. In Josephson interferometry experiments this CAR contribution leads to an additional period with h/e in the interference pattern [117–119]. This would alter the value of every second maxima of the interference pattern shown in Fig.6.5 a. We, however, observe no signs of a CAR contribution in our measurements, which might be attributed to the fact that d_{gg} is not shorter but comparable to ξ_{MoRe}. Further we note that the graphene edges are not lying exactly on top of each other due to the etching profile, which increases the effective distance between the layers. This profile can be seen in the shape of the interface between the MoRe and the vdWh shown Fig.5.2.

6.5. Asymmetric SQUID and CPR

Finally we measure the CPR of each JJ employing the high individual tunability of the switching currents. The CPR gives an insight into the Cooper

pair transport across the junction, e.g. transparency of Andreev bound states. In the following we discuss how an asymmetric SQUID allows the measurement of the CPR of the JJ with the smaller I_c. For I_c^b much larger than I_c^t ($\frac{I_c^b}{I_c^t} \geq 10$), φ_b can be assumed constant in Eq.6.2 such that f^b stays at its maximum value. This results in a total critical current of the device of $I_c^{tot} = I_c^b + I_c^t f^t(\varphi_b^{max} - \frac{2\pi\Phi}{\Phi_0})$ [198]. In this case a changing flux leads to an oscillation around I_c^b with an amplitude of $\pm I_c^t$, while the shape of the oscillation is given by f^t.

The number of transport channels and their transparencies determine the CPR, and the I_c of a short JJ is then given by

$$I_c = \frac{e\Delta}{2\hbar} \sum_n \frac{t_n \sin(\varphi)}{\sqrt{1 - t_n \sin^2(\varphi/2)}}, \tag{6.4}$$

where t_n is the transparency of the n-th channel and φ is the phase difference over the junction [199–201]. For a superconductor-insulator-superconductor JJ, one expects a sinusoidal CPR since only channels with low transparency ($t_n \ll 1$) contribute to the transport. If the channel transparencies increase the maximum of the CPR starts to deviate from $\varphi_{max} = \pi/2$ towards π [38, 84, 202, 203]. This deviation is quantified by the skewness of the CPR, defined as $S = \frac{\varphi^{max} - \pi/2}{\pi/2}$ [84]. The skewness is 0 when the CPR is sinusoidal and $t_n \ll 1$ and is 1 for $t_n = 1$, which corresponds to a saw tooth like CPR. Note, that S and t_n have a non-linear relation, and a single channel with $t=0.9$ for example causes only a skewness of 0.34.

6.5.1. Skewness of the CPR

In Fig.6.7 a we show the results of the CPR measurements around the CNP for both layers. The reference junction was highly n doped and has a large I_c ($I_c^t \approx 1.5\,\mu A$, $I_c^b \approx 2\,\mu A$ for the top and bottom panel respectively). Four examples of the CPR at different densities are shown in Fig.6.7 b. The positions in n_b are indicated by the coloured lines in Fig.6.7 a. A strong decrease of the amplitude at the CNP is observed (orange). For values of $n_b \neq 0$ we observe a skewed sinusoidal like oscillation. To extract the skewness, the measurement data were fitted over six periods using,

$$I_c^i = \sum_{n=1}^{5} a_n \sin(nf(B_y + B_0)), \tag{6.5}$$

where a_n is the prefactor of the n-th harmonic, f the frequency of the oscillations, and B_0 the shift in magnetic field with respect to the first zero crossing of the oscillation. The prefactors and their ratio is shown in Sec.6.5.2. The skewness as a function of carrier density was extracted from the maximum

6
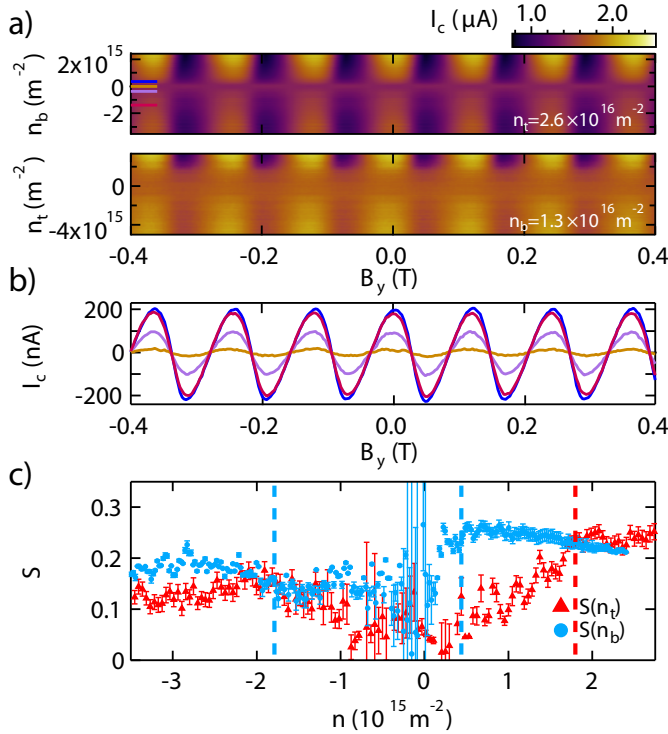
Figure 6.7. a)Interference pattern as a function of n_b (top) and n_t (bottom) for fixed top respectively bottom charge carrier density for JJ_2^{DLG}. b) Cuts of the interference pattern as a function of B_y for different n_b after subtracting the critical current of the reference junction. The color of the curves corresponds to the color of the bars at the left axis of the top graph in a), which indicates the positions in n_b where the line cuts are taken. c) The skewness of the CPR as a function of n_b (blue) and n_t (red) are shown.

value of the fit for both layers and is plotted in Fig.6.7 c. Extracting S from the fit increases its accuracy since several periods are taken into account. The largest S was observed, if the layers are n doped. It reaches a value of around 0.25. For the p doped graphene a S of around 0.15 was deduced from the data. These values decrease when the carrier density is reduced. At the CNP there is large uncertainty in the measurement due to the small amplitude of the oscillation. Nevertheless, towards the CNPs we observe a reduction of the skewness, which indicates that the transparency of the modes reduces when compared to that at higher doping. By fitting the measured curves with Eq.6.4 assuming one channel, we obtain a transparency of 0.6 for p doping and one of around 0.7 for n doping. Even though, the electron transport in the graphene has a ballistic nature, the finite contact resistance limits the transparency. By increasing the electron density, $S(n_b)$ appears to decrease again. This is not due to a decrease of the transparency of the superconducting modes, but has to be attributed to the transition from the asymmetric to the symmetric regime, in which the CPR is not probed any more.

6.5.2. Gate dependence of a_n

To fit the CPR we used Eq.6.5, which contains up to the fifth harmonic in frequency. If the CPR is sinusoidal a_2 to a_5 are all zero and only the first harmonic exists. The non-vanishing amplitudes of the higher harmonic indicate, that the CPR will be skewed and can be used as an alternative measurement quantity to the skewness, which determines the deviation of the CPR from the sinusoidal behavior. For completion, we plot the a_1 to a_3 and the ratio between a_2 and a_1, as well as the ratio between a_3 and a_1 in Fig.6.8. The amplitudes a_4 and a_5 are much smaller than the others and their contribution to S can be neglected. For n (p) doped graphene a skewness of 0.25 (0.15) was extracted. This value corresponds to a ratio of $a_2/a_1 \approx 0.15$ (0.1).

6.5.3. Loop inductance and screening

We note, that the self inductance L_s of the SQUID can also lead to a non-linear dependence of φ as a function of magnetic field [200]. This effect is especially dominant around $\varphi = \pi/2$, where the current in the loop is the largest. This can seem like the observation of a non-sinusoidal CPR as a function of the external flux and must be taken into account, when the external flux is converted into the phase difference over the junction. However our compact DLG SQUID has a very small perimeter, and the L_s can be neglected (see App.6.A).
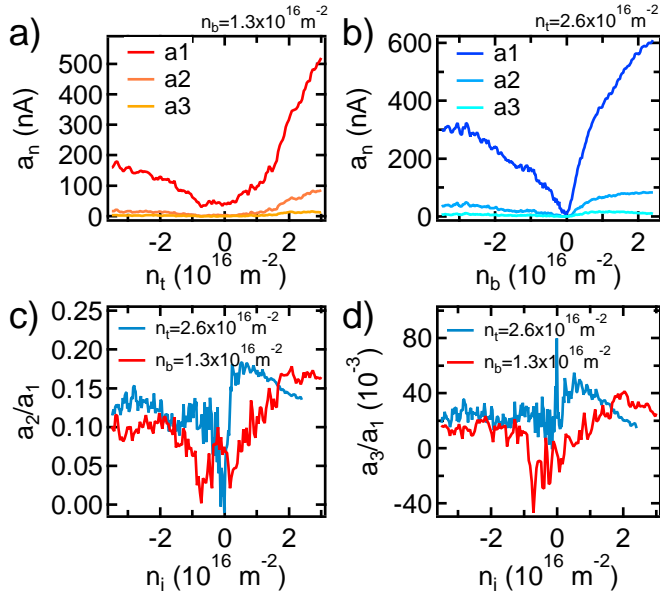
Figure 6.8. a) Fitting coefficients a_1, a_2, and a_3 as a function of n_t for n_b=1.3×10^{-2}. b) Fitting coefficients a_1, a_2, and a_3 as a function of n_b for n_t=2.6×10^{-2}. c) Ratio of a_2 and a_1, which are shown in a) and b). d) Ratio of a_3 and a_1, which are shown in a) and b).

6.6. Conclusion and Outlook

In conclusion, we fabricated a compact double layer graphene SQUID, in which the normal state resistance and critical current of each graphene Josephson junction can be tuned individually by gating. As expected from the Ambegaokar-Baratoff relation the critical current is inverse proportional to the normal state resistance. Therefore, their product is constant, but smaller than the expected Thouless energy in the long, ballistic limit. This is attributed to the imperfection of the contacts, which leads to reflection and an increase of the trajectories. The individual tunability of the critical current of each Josephson junction opens the possibility to continuously tune the SQUID from the symmetric to the asymmetric regime. To measure the SQUID response with respect to an external flux, the in-plane magnetic field had to be carefully calibrated. In the symmetric regime we observe a cosine like interference pattern. The non-vanishing critical current at a flux of half a flux

quantum could be attributed to a slight asymmetry of the critical currents and a non-sinusoidal current phase relation. Note, that no contribution of crossed Andreev reflection to the supercurrent tranport was observed, which would have appeared in an alternation of every second maxima of the in-plane magnetic field interference pattern. The current phase relation was then measured in the asymmetric regime, where one junction was used to phase bias the other. A skewness of 0.15 for hole doped graphene and one of 0.25 for electron doped graphene was observed. This corresponds to a transparency between 0.6-0.7 of a single channel in the short junction limit.

.

6

6.A. Supporting Informations

Calculation of the interference pattern

To get an idea of the asymmetry of the measurement shown in Fig.6.5 a, we calculated the in-plane magnetic field dependence of the I_c. The CPRs were chosen to be equal and with skewness of $S=0.18$. The blue curve is the result of $I_c^b = 1.2\,\mu\text{A}$ and $I_c^t = 0.6\,\mu\text{A}$, the red one for $I_c^b = 1.4\,\mu\text{A}$ and $I_c^t = 1.4\,\mu\text{A}$ and the green for $I_c^b = 2\,\mu\text{A}$ and $I_c^t = 1.4\,\mu\text{A}$. For the blue result we took the dimension (junction length and middle hBN thickness) of J_1^{DLG}, for the red the dimension of J_2^{DLG}, and for the green curve the dimension of J_3^{DLG}. The result reproduces qualitatively the measurements in Fig.6.5 a. Therefore, we conclude that the in-plane magnetic field dependence of J_2^{DLG} was in a rather symmetric state of the SQUID, while for J_1^{DLG} and J_3^{DLG} the SQUID was slightly asymmetric. The calculations also reproduce the shape of the different curves.
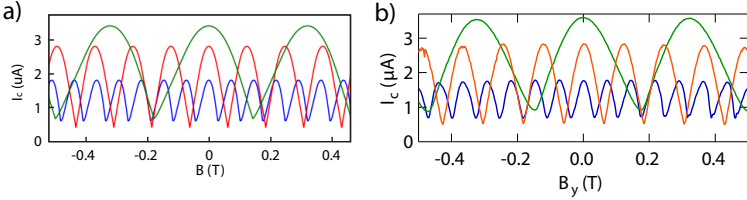

Figure 6.9. a) Calculated interference pattern for a SQUID with a skewed CPR ($S=0.18$). The different curves, indicated by different colors, were obtained for different SQUID areas, which corresponds to the ones of J_1^{DLG} (blue), J_2^{DLG} (red) and J_3^{DLG} (green). b) Measurement of the critical current as a function of in-plane magnetic field for J_1^{DLG}, J_2^{DLG}, and J_3^{DLG}.

Estimation of the loop inductance

The loop inductance (L_s) can lead to a screening of the external magnetic field, which reduces the actual flux (Φ) inside the SQUID. Furthermore, it makes the relation between Φ and the external flux (Φ_{ext}) non linear. When the magnetic field axis is converted to a phase axis, this non linearity has to be taken into account, if L_s or I_c is large. The external flux as a function of Φ can be expressed by

$$\Phi_{ext} = \Phi + L_s I_c f\left(\frac{\pi\Phi}{\Phi_0}\right). \tag{6.6}$$

Moreover, L_s and I_c determine the limit, above which the phase biasing by a magnetic field becomes hysteretic. This limit is given by $2L_sI_c/\Phi_0 \approx 1$. To estimate the loop inductance, we calculated the kinetic inductance (L_k) of the MoRe leads and the geometric inductance (L_g) of the SQUID loop. The sum of these inductances results in L_s.

L_k was measured by the temperature dependence of the resonance frequency (f_{res}) of a $\lambda/4$-resonator.

$$2\pi f_{res} = \cfrac{1}{4l\sqrt{\left(L_m + \cfrac{L_k^0}{1-\left(\frac{T}{T_c}\right)^4}\right) \cdot C_m}}, \qquad (6.7)$$

where l is the length of the resonator and L_k^0 is the kinetic inductance per unit length in the zero temperature limit. The geometric inductance of the resonator (L_m) as well as the geometric capacitance of the resonator (C_m) were calculated as described in Ref.[139]. We obtain a sheet inductance of L_k^s=4.26 pH for a resonator thickness of 70 nm. The kinetic inductance is obtained by multiplying the sheet inductance with the interlayer distance, here d_{gg}=25 nm, and divide it by the the contacts width of 550 nm. By doing so L_k=0.19 pH. Note, that this is an upper bound of the kinetic inductance, since the L_k^s was determined using a 70 nm thick resonator.

To estimate L_g we calculate the inductance of a rectangular loop as derived in Ref.[204] for J_2^{DLG}. Here we take the following values: l_1=L = 650 nm, $l_2 = d_{gg} = 25$ nm, w=0.3 nm (thickness of graphene) and h=1 nm, which corresponds to the width of the loop. By taking h equal to only 1 nm instead of the entire junction width, we get an upper limit of the geometrical inductance of L_g=1.2×10^{-12} H. This has to be done since the used formula does not hold if h is much larger than the product of l_2 and l_2.

We calculate now the difference between Φ_{ext} and Φ at $\Phi = \pi/2$, where the effect of the screening is the strongest. For a critical current of $3\,\mu$A, the difference is not more then 0.3%. Furthermore, the maximal current, which can be passed through the SQUID before it starts to behave hysteretic is $I_c^h \approx 1$ mA. For these reasons screening effects can be neglected in our measurements, since the measured critical currents are way smaller and the non linearity is not present.
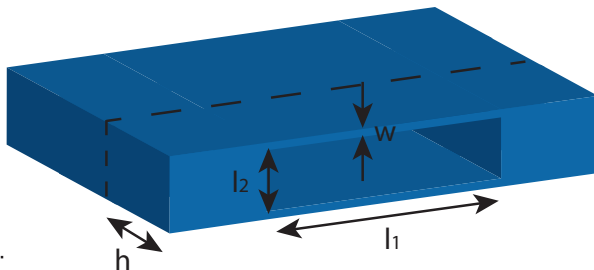
6

6

Figure 6.10. Schematic drawing of the model taken to calculate the geometrical inductance of a DLG SQUID. The thin segment in the center on the top and bottom with a hight w stand for the graphene in the DLG JJ device.

7 Conclusion and Outlook

The goal of this thesis was to investigate the possibility of creating topological superconductivity in graphene based van der Waals heterostructures. The pursued way was to engineer helical quantum Hall states by lifting the spin and valley degeneracy of the 0th Landau level using high quality double layered graphene structures. The counter propagating modes of the helical quantum Hall state were then intended to be coupled by crossed Andreev reflection at a superconductor.

In summary the proximity effect in graphene based van der Waals heterostructres were studied in Josephson junction configurations and multi-layered, high quality structures were engineered to establish helical quantum Hall states in graphene based electronics. The fabrication methods and the procedure are described in Ch.3. In Ch.4, we showed that the supercurrent in graphene-hBN superlattice Josephson junctions reveals signatures of the superlattice's modified bandstructure, like van Hove singularities and the accompanied change of the charge carrier type as well as the appearance of satellite Dirac points. Furthermore, an increased edge to bulk current ratio was observed at the van Hove singularities, which mimics an edge current, but arises due to localisation of the charge carriers in the bulk of the junction [57]. After the Josephson coupling in graphene was realized in a single layer, more complex device structures were investigated, namely large angle twisted bilayer graphene and double layer graphene structures. In Ch.5, we created spin polarized, counter propagating states, which formed a helical quantum Hall state delocalized over the two graphene sheets by gate tune the layers to opposite filling factors of $\nu = \pm 1$. This state manifests itself as a conductance plateau of $2e^2/h$. In the quantum Hall regime no coupling of the counter propagating states were observed in a Josephson junction geometry, which would have been detected as a supercurrent or the appearance of superconducting pockets. The absence of superconducting coupling between the layers is attributed to the potentially to large interlayer spacing, which has to be in the order or well below the superconducting coherence length of MoRe, and the momentum mismatch between the individual layers, such that there is no available state in the other layer for the reflected hole with opposite momentum of the incoming electron. In Ch.6 we studied the in-plane magnetic field dependence of the supercurrent in double layer graphene Josephson junctions. We show that the in-plane

magnetic field dependence is accurate enough to probe eventual h/e periodic signals, which would be an indication of cross Andreev processes. The global and independent tunability of the supercurrent in each graphene layer allowed us to measure their current-phase relation separately, which revealed highly transparent superconducting modes in both of them.

The next step towards topological supercurrent in double layer graphene Josephson junctions is to observe superconducting correlations between the superconducting modes in the two layers, first at low magnetic fields and later in the quantum Hall regime. For that it would be beneficial to reduce the hBN spacer's thickness well below the superconducting coherence length of the superconducting contacts. So far only structures with a minimal spacer thickness of 12 nm were studied. Possibly the alignment of graphenes' momentum space may play a major role in the appearance of crossed Andreev reflection between the layers [37]. The momentum space could be aligned by using the same graphene flake for the top and the bottom layer by the tear and stack technique as described in Ch.3 without introducing a twist angle between the created pieces, while picking up the hBN spacer. Possible measurements to detect a crossed Andreev processes contributing to the supercurrent would then be the following. At zero magnetic field one would expect an increased critical current compared to just the sum of the critical currents carried in the individual layers due to the additional process as observed in a double nanowire device [205]. This could be investigated by measuring the gate dependence of the critical current for each layer while the other is kept at the charge neutrality point, where the critical current is expected to be significantly small. Another possible experiment would be to probe the in-plane magnetic field interference pattern of the critical current, which should host a h/e contribution [118]. Instead of using a Josephson junction device structure one could use a multi-terminal device as in Ref.[120], where the two layers are connected separately and only have one common superconducting contact, to detect the crossed Andreev reflection in graphene by a negative non-local signal. In the quantum Hall regime the interlayer coupling would be potentially observed by a strong reduced resistance at zero bias current, when the edge states in the two graphene layers are counter propagating. Further, a periodicity of h/e is expected when the critical current is measured as a function of in-plane magnetic field.

Furthermore, the helical state in graphene can also be realized by other approaches. As it was shown by Veyrat et al.[98], the ground state of the 0th Landau level changes when the graphene is brought in to close proximity with a SrTiO$_3$ substrate, which has a large dielectric constant and that screens the long range Coulomb interaction between the electrons. This new ground state hosts helical edge states, which could be coupled to superconductors at moderate magnetic fields of 1.5 T. A different route was proposed by Kane and Mele [206], which calculated that at low temperatures graphene can turn into

a quantum spin Hall insulator if Rashba spin orbit coupling is present, such that the bulk is insulating and helical states are present at the edges. Since the intrinsic Kane-Mele type spin orbit coupling in graphene is too weak for observing this effect experimentally, recent studies tried to enhance the spin orbit coupling by van der Waals engineering. It was observed that graphene in proximity to WSe_2, WS_2, and MoS_2 exhibits an increased spin orbit interaction strength [20, 21], but so far it seems that the valley Zeeman spin orbit interaction is the dominating mechanism and not the desired Kane-Mele type. Therefore, further investigations in this direction are still needed.

7

Bibliography

[1] T. D. Ladd, F. Jelezko, R. Laflamme, Y. Nakamura, C. Monroe, and J. L. O'Brien, Nature **464**, 45 (2010).

[2] F. Jazaeri, A. Beckers, A. Tajalli, and J. M. Sallese, arXiv **1908.02656** (2019), 10.23919/MIXDES.2019.8787164.

[3] R. M. Lutchyn, E. P. Bakkers, L. P. Kouwenhoven, P. Krogstrup, C. M. Marcus, and Y. Oreg, Nature Reviews Materials **3**, 52 (2018).

[4] H. Kamerlingh Onnes, Leiden Communication **120b, 122b** (1911).

[5] W. Meissner and R. Ochsenfeld, Die Naturwissenschaften **21**, 787 (1933).

[6] K. S. Novoselov, A. K. Geim, S. V. Morozov, D. Jiang, Y. Zhang, S. V. Dubonos, I. V. Grigorieva, and A. A. Firsov, Science **306**, 666 (2004).

[7] R. Peierls, Annales de l'I. H. P. **3**, 177 (1935).

[8] L. Landau, Phys. Z. Sowjetunion **11**, 26 (1937).

[9] C. R. Dean, A. F. Young, I. Meric, C. Lee, L. Wang, S. Sorgenfrei, K. Watanabe, T. Taniguchi, P. Kim, K. L. Shepard, and J. Hone, Nature Nanotechnology **5**, 722 (2010).

[10] L. Britnell, R. V. Gorbachev, R. Jalil, B. D. Belle, F. Schedin, M. I. Katsnelson, L. Eaves, S. V. Morozov, A. S. Mayorov, N. M. Peres, A. H. Castro Neto, J. Leist, A. K. Geim, L. A. Ponomarenko, and K. S. Novoselov, Nano Letters **12**, 1707 (2012).

[11] D. Le, A. Barinov, E. Preciado, M. Isarraraz, I. Tanabe, T. Komesu, C. Troha, L. Bartels, T. S. Rahman, and P. A. Dowben, Journal of Physics Condensed Matter **27**, 1 (2015).

[12] S. Wu, V. Fatemi, Q. D. Gibson, K. Watanabe, T. Taniguchi, R. J. Cava, and P. Jarillo-Herrero, Science **359**, 76 (2018).

[13] Z. Wang, B. J. Wieder, J. Li, B. Yan, and B. A. Bernevig, Physical Review Letters **123**, 1 (2019).

[14] A. Kononov, G. Abulizi, K. Qu, J. Yan, D. Mandrus, K. Watanabe, T. Taniguchi, and C. Schönenberger, Nano letters **20**, 4228 (2020).

[15] X. Xi, Z. Wang, W. Zhao, J. H. Park, K. T. Law, H. Berger, L. Forró, J. Shan, and K. F. Mak, Nature Physics **12**, 139 (2016).

[16] B. Huang, G. Clark, E. Navarro-Moratalla, D. R. Klein, R. Cheng, K. L. Seyler, D. Zhong, E. Schmidgall, M. A. McGuire, D. H. Cobden, W. Yao, D. Xiao, P. Jarillo-Herrero, and X. Xu, Nature **546**, 270 (2017).

[17] J. C. Leutenantsmeyer, A. A. Kaverzin, M. Wojtaszek, and B. J. V. Wees, 2D Materials **4**, 1 (2017).

[18] Z. Wang, C. Tang, R. Sachs, Y. Barlas, and J. Shi, Physical Review Letters **114**, 1 (2015).

[19] B. Yang, M.-F. Tu, J. Kim, Y. Wu, H. Wang, J. Alicea, R. Wu, M. Bockrath, and J. Shi, 2D Materials Letter **3**, 031012 (2016).

[20] S. Zihlmann, A. W. Cummings, J. H. Garcia, M. Kedves, K. Watanabe, T. Taniguchi, C. Schönenberger, and P. Makk, Physical Review B **97**, 075434 (2018).

[21] T. Wakamura, F. Reale, P. Palczynski, M. Q. Zhao, A. T. Johnson, S. Guéron, C. Mattevi, A. Ouerghi, and H. Bouchiat, Physical Review B **99**, 1 (2019).

[22] T. Völkl, T. Rockinger, M. Drienovsky, K. Watanabe, T. Taniguchi, D. Weiss, and J. Eroms, Physical Review B **96**, 1 (2017).

[23] L. A. Ponomarenko, R. V. Gorbachev, G. L. Yu, D. C. Elias, R. Jalil, A. A. Patel, A. Mishchenko, A. S. Mayorov, C. R. Woods, J. R. Wallbank, M. Mucha-Kruczynski, B. A. Piot, M. Potemski, I. V. Grigorieva, K. S. Novoselov, F. Guinea, V. I. Fal'ko, and A. K. Geim, Nature **497**, 594 (2013).

[24] C. R. Woods, L. Britnell, A. Eckmann, R. S. Ma, J. C. Lu, H. M. Guo, X. Lin, G. L. Yu, Y. Cao, R. V. Gorbachev, A. V. Kretinin, J. Park, L. A. Ponomarenko, M. I. Katsnelson, Y. N. Gornostyrev, K. Watanabe, T. Taniguchi, C. Casiraghi, H. J. Gao, A. K. Geim, and K. S. Novoselov, Nature Physics **10**, 451 (2014).

[25] Y. Cao, V. Fatemi, A. Demir, S. Fang, S. L. Tomarken, J. Y. Luo, J. D. Sanchez-Yamagishi, K. Watanabe, T. Taniguchi, E. Kaxiras, R. C. Ashoori, and P. Jarillo-Herrero, Nature **556**, 80 (2018).

[26] J. G. Daunt and K. Mendelssohn, Proc. Roy. Soc **A185**, 255 (1946).

[27] J. Bardeen, L. N. Cooper, and J. R. Schrieffer, Theory of Superconductivity **105**, 1175 (1957).

[28] M. Tinkham, *Introduction to Superconductivity*, 2nd ed. (McGraw-Hill Book CO., 1996).

[29] T. T. Heikkilä, *The Physics of Nanoelectronics* (2013).

[30] B. D. Josephson, Phys: Lett. **1**, 251 (1962).

[31] H. B. Heersche, P. Jarillo-Herrero, J. B. Oostinga, L. M. K. Vandersypen, and A. F. Morpurgo, Nature **446**, 56 (2007).

[32] K. K. Likharev, Reviews of Modern Physics **51** (1979), 10.1017/CBO9781107415324.004.

[33] G. E. Blonder, M. Tinkham, and T. M. Klapwijk, Physical Review B **25**, 4515 (1982).

[34] Y. V. Nazarov and Y. Blanter, *Quantum Transport: Introduction to Nanoscience* (Cambridge University Press, 2009).

[35] C. W. Beenakker, Reviews of Modern Physics **80**, 1337 (2008).

[36] D. K. Efetov, L. Wang, C. Handschin, K. B. Efetov, J. Shuang, R. Cava, T. Taniguchi, K. Watanabe, J. Hone, C. R. Dean, and P. Kim, Nature Physics **12**, 328 (2016).

[37] C. W. Beenakker, Physical Review Letters **97**, 1 (2006).

[38] L. Bretheau, J. I.-J. Wang, R. Pisoni, K. Watanabe, T. Taniguchi, and P. Jarillo-Herrero, Nature Physics **13**, 756 (2017).

[39] J. D. Pillet, C. H. Quay, P. Morfin, C. Bena, A. L. Yeyati, and P. Joyez, Nature Physics **6**, 965 (2010).

[40] W. Chang, V. E. Manucharyan, T. S. Jespersen, J. Nygård, and C. M. Marcus, Physical Review Letters **110**, 1 (2013).

[41] L. Bretheau, Ç. Ö. Girit, H. Pothier, D. Esteve, and C. Urbina, Nature **499**, 312 (2013).

[42] L. Tosi, C. Metzger, M. F. Goffman, C. Urbina, H. Pothier, S. Park, A. L. Yeyati, J. Nygård, and P. Krogstrup, Physical Review X **9**, 011010 (2019).

[43] F. Chiodi, M. Ferrier, K. Tikhonov, P. Virtanen, T. T. Heikkilä, M. Feigelman, S. Guéron, and H. Bouchiat, Scientific Reports **1**, 1 (2011).

[44] B. Dassonneville, A. Murani, M. Ferrier, S. Guéron, and H. Bouchiat, PHYSICAL REVIEW B **97**, 184505 (2018).

[45] D. B. Szombati, S. Nadj-Perge, D. Car, S. R. Plissard, E. P. Bakkers, and L. P. Kouwenhoven, Nature Physics **12**, 568 (2016).

[46] V. Ambegaokar and A. Baratoff, Physical Review Letters **10**, 486 (1963).

[47] P. Dubos, H. Courtois, B. Pannetier, F. K. Wilhelm, A. D. Zaikin, and G. Schön, Physical Review B **63**, 1 (2001).

[48] C. Li, S. Guéron, A. Chepelianskii, and H. Bouchiat, Physical Review B **94**, 1 (2016).

[49] C. T. Ke, I. V. Borzenets, A. W. Draelos, F. Amet, Y. Bomze, G. Jones, M. Craciun, S. Russo, M. Yamamoto, S. Tarucha, and G. Finkelstein, Nano Letters **16**, 4788 (2016).

[50] I. V. Borzenets, F. Amet, C. T. Ke, A. W. Draelos, M. T. Wei, A. Seredinski, K. Watanabe, T. Taniguchi, Y. Bomze, M. Yamamoto, S. Tarucha, and G. Finkelstein, Physical Review Letters **117**, 1 (2016).

7

[51] R. C. Dynes and T. A. Fulton, Physical Review B **3**, 3015 (1971).

[52] S. Shapiro, Physical Review Letters **11**, 80 (1963).

[53] I. Giaever, Physical Review Letters **14**, 904 (1965).

[54] M. Octavio, M. Tinkham, G. E. Blonder, and T. M. Klapwijk, Physical Review B **27**, 6739 (1983).

[55] C. Handschin, *Quantum Transport in Encapsulated Graphene P-N junctions*, Ph.D. thesis, Basel (2017).

[56] T. Ihn, *Semiconductor Nanostrucutres - Quantum States and Electronic Transport* (2010).

[57] D. I. Indolese, R. Delagrange, P. Makk, J. R. Wallbank, K. Watanabe, T. Taniguchi, and C. Schönenberger, Physical Review Letters **121**, 137701 (2018).

[58] M. Yankowitz, J. Xue, D. Cormode, J. D. Sanchez-Yamagishi, K. Watanabe, T. Taniguchi, P. Jarillo-Herrero, P. Jacquod, and B. J. LeRoy, Nature Physics **8**, 382 (2012).

[59] C. H. Park, L. Yang, Y. W. Son, M. L. Cohen, and S. G. Louie, Physical Review Letters **101**, 1 (2008).

[60] G. L. Yu, R. V. Gorbachev, J. S. Tu, A. V. Kretinin, Y. Cao, R. Jalil, F. Withers, L. A. Ponomarenko, B. A. Piot, M. Potemski, D. C. Elias, X. Chen, K. Watanabe, T. Taniguchi, I. V. Grigorieva, K. S. Novoselov, V. I. Fal'ko, A. K. Geim, and A. Mishchenko, Nature Physics **10**, 525 (2014).

[61] J. L. McChesney, A. Bostwick, T. Ohta, T. Seyller, K. Horn, J. González, and E. Rotenberg, Physical Review Letters **104**, 1 (2010).

[62] M. L. Kiesel, C. Platt, W. Hanke, D. A. Abanin, and R. Thomale, Physical Review B **86**, 1 (2012).

[63] G. Li, A. Luican, J. M. B. Lopes Dos Santos, A. H. Castro Neto, A. Reina, J. Kong, and E. Y. Andrei, Nature Physics **6**, 109 (2010).

[64] R. Brown, N. R. Walet, and F. Guinea, Physical Review Letters **120**, 26802 (2018).

[65] R. V. Gorbachev, I. Riaz, R. R. Nair, R. Jalil, L. Britnell, B. D. Belle, E. W. Hill, K. S. Novoselov, K. Watanabe, T. Taniguchi, A. K. Geim, and P. Blake, Small **7**, 465 (2011).

[66] M. J. Zhu, A. V. Kretinin, M. D. Thompson, D. A. Bandurin, S. Hu, G. L. Yu, J. Birkbeck, A. Mishchenko, I. J. Vera-Marun, K. Watanabe, T. Taniguchi, M. Polini, J. R. Prance, K. S. Novoselov, A. K. Geim, and M. B. Shalom, Nature Communications **8**, 1 (2017).

[67] J. R. Wallbank, A. A. Patel, M. Mucha-Kruczyński, A. K. Geim, and V. I. Fal'Ko, Physical Review B **87**, 1 (2013).

7

[68] M. Lee, J. R. Wallbank, P. Gallagher, K. Watanabe, T. Taniguchi, V. I. Fal'Ko, and D. Goldhaber-Gordon, Science **353**, 1526 (2016).

[69] E. H. Hwang, S. Adam, and S. D. Sarma, Physical Review Letters **98**, 1 (2007).

[70] S. Adam, E. H. Hwang, V. M. Galitski, and S. Das Sarma, Proceedings of the National Academy of Sciences of the United States of America **104**, 18392 (2007).

[71] J. H. Chen, C. Jang, S. Xiao, M. Ishigami, and M. S. Fuhrer, Nature Nanotechnology **3**, 206 (2008).

[72] X. Hong, K. Zou, and J. Zhu, Physical Review B - Condensed Matter and Materials Physics **80**, 1 (2009).

[73] M. I. Katsnelson and A. K. Geim, Philosophical Transactions of the Royal Society A: Mathematical, Physical and Engineering Sciences **366**, 195 (2008).

[74] L. Wang, P. Makk, S. Zihlmann, A. Baumgartner, D. I. Indolese, K. Watanabe, T. Taniguchi, and C. Schönenberger, Physical Review Letters **124**, 1 (2020).

[75] N. Tombros, A. Veligura, J. Junesch, M. H. Guimaräes, I. J. Vera-Marun, H. T. Jonkman, and B. J. Van Wees, Nature Physics **7**, 697 (2011).

[76] B. Terrés, L. A. Chizhova, F. Libisch, J. Peiro, D. Jörger, S. Engels, A. Girschik, K. Watanabe, T. Taniguchi, S. V. Rotkin, J. Burgdörfer, and C. Stampfer, Nature Communications **7**, 1 (2016).

[77] R. Kraft, J. Mohrmann, R. Du, P. B. Selvasundaram, M. Irfan, U. N. Kanilmaz, F. Wu, D. Beckmann, H. Von Löhneysen, R. Krupke, A. Akhmerov, I. Gornyi, and R. Danneau, Nature Communications **9**, 1 (2018).

[78] I. Meric, M. Y. Han, A. F. Young, B. Ozyilmaz, P. Kim, and K. L. Shepard, Nature Nanotechnology **3**, 654 (2008).

[79] A. F. Young and P. Kim, Nature Physics **5**, 222 (2009).

[80] V. V. Cheianov and V. I. Fal'ko, Physical Review B - Condensed Matter and Materials Physics **74**, 1 (2006).

[81] M. I. Katsnelson, K. S. Novoselov, and A. K. Geim, Nature Physics **2**, 620 (2006).

[82] O. Klein, Zeitschrift für Physik **53**, 157 (1929).

[83] C. Handschin, P. Makk, P. Rickhaus, M. H. Liu, K. Watanabe, T. Taniguchi, K. Richter, and C. Schönenberger, Nano Letters **17**, 328 (2017).

[84] G. Nanda, J. L. Aguilera-Servin, P. Rakyta, A. Kormányos, R. Kleiner, D. Koelle, K. Watanabe, T. Taniguchi, L. M. Vandersypen, and S. Goswami, Nano Letters **17**, 3396 (2017).

[85] V. E. Calado, S. Goswami, G. Nanda, M. Diez, A. R. Akhmerov, K. Watanabe, T. Taniguchi, T. M. Klapwijk, and L. M. K. Vandersypen, Nature Nanotechnology **10**, 761 (2015).

7

[86] M. Ben Shalom, M. J. Zhu, V. I. Fal'ko, A. Mishchenko, A. V. Kretinin, K. S. Novoselov, C. R. Woods, K. Watanabe, T. Taniguchi, A. K. Geim, and J. R. Prance, Nature Physics **12**, 318 (2016).

[87] K. V. Klitzing, G. Dorda, and M. Pepper, Physical Review Letters **45**, 494 (1980).

[88] J. R. Williams, D. A. Abanin, L. Dicarlo, L. S. Levitov, and C. M. Marcus, Physical Review B - Condensed Matter and Materials Physics **80**, 1 (2009).

[89] Y. Zhang, Z. Jiang, J. P. Small, M. S. Purewal, Y. W. Tan, M. Fazlollahi, J. D. Chudow, J. A. Jaszczak, H. L. Stormer, and P. Kim, Physical Review Letters **96**, 1 (2006).

[90] A. F. Young, C. R. Dean, L. Wang, H. Ren, P. Cadden-Zimansky, K. Watanabe, T. Taniguchi, J. Hone, K. L. Shepard, and P. Kim, Nature Physics **8**, 550 (2012).

[91] D. A. Abanin, P. A. Lee, and L. S. Levitov, Physical Review Letters **96**, 1 (2006).

[92] K. Nomura and A. H. MacDonald, Physical Review Letters **96**, 1 (2006).

[93] F. Amet, J. R. Williams, K. Watanabe, T. Taniguchi, and D. Goldhaber-Gordon, Physical Review Letters **112**, 1 (2014).

[94] A. J. Giesbers, L. A. Ponomarenko, K. S. Novoselov, A. K. Geim, M. I. Katsnelson, J. C. Maan, and U. Zeitler, Physical Review B - Condensed Matter and Materials Physics **80**, 1 (2009).

[95] M. Tahir and K. Sabeeh, Journal of Physics Condensed Matter **24** (2012), 10.1088/0953-8984/24/13/135005.

[96] H. A. Fertig and L. Brey, Physical Review Letters **97**, 2 (2006).

[97] A. F. Young, J. D. Sanchez-Yamagishi, B. Hunt, S. H. Choi, K. Watanabe, T. Taniguchi, R. C. Ashoori, and P. Jarillo-Herrero, Nature **505**, 528 (2014).

[98] L. Veyrat, C. Déprez, A. Coissard, X. Li, F. Gay, K. Watanabe, T. Taniguchi, Z. Han, B. A. Piot, H. Sellier, and B. Sacépé, Science **367**, 781 (2020).

[99] J. D. Sanchez-Yamagishi, J. Y. Luo, A. F. Young, B. Hunt, K. Watanabe, T. Taniguchi, R. C. Ashoori, and P. Jarillo-Herrero, Nature Nanotechnology **12**, 118 (2016).

[100] P. San-Jose, J. L. Lado, R. Aguado, F. Guinea, and J. Fernández-Rossier, Physical Review X **5**, 1 (2015).

[101] D. I. Indolese, P. Karnatak, A. Kononov, R. Delagrange, R. Haller, L. Wang, P. Makk, K. Watanabe, T. Taniguchi, and C. Schönenberger, arXiv (2020).

[102] V. Mourik, K. Zuo, S. M. Frolov, S. R. Plissard, E. P. Bakkers, and L. P. Kouwenhoven, Science **336**, 1003 (2012).

7

[103] L. P. Rokhinson, X. Liu, and J. K. Furdyna, Nature Physics **8**, 795 (2012).

[104] A. Das, Y. Ronen, Y. Most, Y. Oreg, M. Heiblum, and H. Shtrikman, Nature Physics **8**, 887 (2012).

[105] H. J. Suominen, J. Danon, M. Kjaergaard, K. Flensberg, J. Shabani, C. J. Palmstrøm, F. Nichele, and C. M. Marcus, Physical Review B **95**, 1 (2017).

[106] G. H. Lee, K. F. Huang, D. K. Efetov, D. S. Wei, S. Hart, T. Taniguchi, K. Watanabe, A. Yacoby, and P. Kim, Nature Physics **13**, 693 (2017).

[107] K. Komatsu, C. Li, S. Autier-Laurent, H. Bouchiat, and S. Guéron, Physical Review B - Condensed Matter and Materials Physics **86**, 1 (2012).

[108] F. Amet, C. T. Ke, I. V. Borzenets, Y.-M. Wang, K. Watanabe, T. Taniguchi, R. S. Deacon, M. Yamamoto, Y. Bomze, S. Tarucha, and G. Finkelstein, Science **352**, 966 (2016).

[109] A. W. Draelos, M. T. Wei, A. Seredinski, C. T. Ke, Y. Mehta, R. Chamberlain, K. Watanabe, T. Taniguchi, M. Yamamoto, S. Tarucha, I. V. Borzenets, F. Amet, and G. Finkelstein, Journal of Low Temperature Physics **191**, 288 (2018).

[110] A. Seredinski, A. Draelos, M. T. Wei, C. T. Ke, T. Fleming, Y. Mehta, E. Mancil, H. Li, T. Taniguchi, K. Watanabe, S. Tarucha, M. Yamamoto, I. V. Borzenets, F. Amet, and G. Finkelstein, MRS Advances **3**, 2855 (2018).

[111] M. Ma and A. Y. Zyuzin, Europhysics Letters **21**, 941 (1993).

[112] A. Y. Zyuzin, Physical Review B **50**, 323 (1994).

[113] M. Stone and Y. Lin, Physical Review B - Condensed Matter and Materials Physics **83**, 1 (2011).

[114] A. Seredinski, A. W. Draelos, E. G. Arnault, M. T. Wei, H. Li, T. Fleming, K. Watanabe, T. Taniguchi, F. Amet, and G. Finkelstein, Science Advances **5**, 1 (2019).

[115] G. H. Park, M. Kim, K. Watanabe, T. Taniguchi, and H. J. Lee, Scientific Reports **7**, 1 (2017).

[116] L. Zhao, E. G. Arnault, A. Bondarev, A. Seredinski, T. F. Larson, A. W. Draelos, H. Li, K. Watanabe, T. Taniguchi, F. Amet, H. U. Baranger, and G. Finkelstein, Nature Physics **16**, 862 (2020).

[117] V. S. Pribiag, A. J. Beukman, F. Qu, M. C. Cassidy, C. Charpentier, W. Wegscheider, and L. P. Kouwenhoven, Nature Nanotechnology **10**, 593 (2015).

[118] B. Baxevanis, V. P. Ostroukh, and C. W. Beenakker, Physical Review B - Condensed Matter and Materials Physics **91**, 1 (2015).

7

[119] F. K. De Vries, T. Timmerman, V. P. Ostroukh, J. Van Veen, A. J. Beukman, F. Qu, M. Wimmer, B. M. Nguyen, A. A. Kiselev, W. Yi, M. Sokolich, M. J. Manfra, C. M. Marcus, and L. P. Kouwenhoven, Physical Review Letters **120**, 1 (2018).

[120] G.-H. Park, K. Watanabe, T. Taniguchi, G.-H. Lee, and H.-J. Lee, Nano Letters **19**, 9002 (2019).

[121] Z. Wang, D. K. Ki, H. Chen, H. Berger, A. H. MacDonald, and A. F. Morpurgo, Nature Communications **6**, 1 (2015).

[122] Z. Wang, D. K. Ki, J. Y. Khoo, D. Mauro, H. Berger, L. S. Levitov, and A. F. Morpurgo, Physical Review X **6**, 1 (2016).

[123] T. Wakamura, F. Reale, P. Palczynski, S. Guéron, C. Mattevi, and H. Bouchiat, Physical Review Letters **120**, 1 (2018).

[124] Y. Y. Wang, R. X. Gao, Z. H. Ni, H. He, S. P. Guo, H. P. Yang, C. X. Cong, and T. Yu, Nanotechnology **23**, 1 (2012).

[125] L. Wang, I. Meric, P. Y. Huang, Q. Gao, Y. Gao, H. Tran, T. Taniguchi, K. Watanabe, L. M. Campos, D. A. Muller, J. Guo, P. Kim, J. Hone, K. L. Shepard, and C. R. Dean, Science **342**, 614 (2013).

[126] J. O. Island, X. Cui, C. Lewandowski, J. Y. Khoo, E. M. Spanton, H. Zhou, D. Rhodes, J. C. Hone, T. Taniguchi, K. Watanabe, L. S. Levitov, M. P. Zaletel, and A. F. Young, Nature **571**, 85 (2019).

[127] Y. Cao, V. Fatemi, S. Fang, K. Watanabe, T. Taniguchi, E. Kaxiras, and P. Jarillo-Herrero, Nature **556**, 43 (2018).

[128] A. David, P. Rakyta, A. Kormányos, and G. Burkard, Physical Review B **100**, 85412 (2019).

[129] P. J. Zomer, M. H. D. Guimaraes, J. C. Brant, N. Tombros, and B. J. Van Wees, Applied Physics Letters **105**, 1 (2014).

[130] P. Rickhaus, J. Wallbank, S. Slizovskiy, R. Pisoni, H. Overweg, Y. Lee, M. Eich, M.-H. Liu, K. Watanabe, T. Taniguchi, V. Fal'ko, T. Ihn, and K. Ensslin, , 1 (2018).

[131] D. G. Purdie, N. M. Pugno, T. Taniguchi, K. Watanabe, A. C. Ferrari, and A. Lombardo, Nature Communications **9**, 1 (2018).

[132] D. I. Indolese, *Fabrication and Characterisation of Amorphous Superconducting Films by Co-sputtering*, Ph.D. thesis (2015).

[133] F. Silsbee, J. Wash. Acad. Sci **6** (1916).

[134] J. G. Daunt and T. S. Smith, Physical Review **88**, 309 (1952).

[135] J. K. Hulm and B. B. Goodman, Physical Review **106**, 659 (1957).

[136] R. A. Hein, J. W. Gibson, M. R. Pablo, and R. D. Blaugher, **129**, 1961 (1963).

7

[137] S. Nau, *Thesis*, Ph.D. thesis (2014).

[138] K. Watanabe, K. Yoshida, and T. Aoki, Japanese Journal of Applied Physics **33**, 570 (1994).

[139] S. Gevorgian, Electronics Letters **30**, 1236 (1994).

[140] J. Kong, N. R. Franklin, C. Zhou, M. G. Chapline, S. Peng, K. Cho, and H. Dai, Science **287**, 622 (2000).

[141] N. Klein and H. Gafni, IEEE Transactions on Electron Devices **ED-13**, 281 (1966).

[142] Y. Hattori, T. Taniguchi, K. Watanabe, and K. Nagashio, ACS Nano **9**, 916 (2015).

[143] J. Kolodzey, S. Member, E. A. Chowdhury, T. N. Adam, G. Qui, I. Rau, J. O. Olowolafe, J. S. Suehle, and Y. Chen, IEEE Transactions on Electron Devices **47**, 121 (2000).

[144] M. T. Allen, O. Shtanko, I. C. Fulga, A. R. Akhmerov, K. Watanabe, T. Taniguchi, P. Jarillo-Herrero, L. S. Levitov, and A. Yacoby, Nature Physics **12**, 128 (2016).

[145] S. Hart, H. Ren, T. Wagner, P. Leubner, M. Mühlbauer, C. Brüne, H. Buhmann, L. W. Molenkamp, and A. Yacoby, Nature Physics **10**, 638 (2014).

[146] L. Angers, F. Chiodi, G. Montambaux, M. Ferrier, S. Guéron, H. Bouchiat, and J. C. Cuevas, Physical Review B **77**, 1 (2008).

[147] I. Brihuega, P. Mallet, H. González-Herrero, G. Trambly De Laissardière, M. M. Ugeda, L. Magaud, J. M. Gómez-Rodríguez, F. Ynduráin, and J. Y. Veuillen, Physical Review Letters **109**, 1 (2012).

[148] Y. Kim, P. Herlinger, P. Moon, M. Koshino, T. Taniguchi, K. Watanabe, and J. H. Smet, Nano Letters **16**, 5053 (2016).

[149] A. Murani, A. Kasumov, S. Sengupta, Y. A. Kasumov, V. T. Volkov, I. I. Khodos, F. Brisset, R. Delagrange, A. Chepelianskii, R. Deblock, H. Bouchiat, and S. Guéron, Nature Communications **8**, 1 (2017).

[150] J. A. Van Dam, Y. V. Nazarov, E. P. Bakkers, S. De Franceschi, and L. P. Kouwenhoven, Nature **442**, 667 (2006).

[151] S. De Franceschi, L. Kouwenhoven, C. Schönenberger, and W. Wernsdorfer, Nature Nanotechnology **5**, 703 (2010).

[152] B. Hunt, T. Taniguchi, P. Moon, M. Koshino, and R. C. Ashoori, Science **340**, 1427 (2013).

[153] Y.-J. Yu, Y. Zhao, S. Ryu, L. E. Brus, K. S. Kim, and P. Kim, Nano letters **9**, 3430 (2009).

[154] A. L. Smith, *Survey of Materials for Theremionic Converters*, Tech. Rep. (1970).

7

[155] Z. Dou, S. Morikawa, A. Cresti, S. W. Wang, C. G. Smith, C. Melios, O. Kazakova, K. Watanabe, T. Taniguchi, S. Masubuchi, T. Machida, and M. R. Connolly, Nano Letters **18**, 2530 (2018).

[156] J. Martin, N. Akerman, G. Ulbricht, T. Lohmann, J. H. Smet, K. Von Klitzing, and A. Yacoby, Nature Physics **4**, 144 (2008).

[157] A. Woessner, P. Alonso-González, M. B. Lundeberg, Y. Gao, J. E. Barrios-Vargas, G. Navickaite, Q. Ma, D. Janner, K. Watanabe, A. W. Cummings, T. Taniguchi, V. Pruneri, S. Roche, P. Jarillo-Herrero, J. Hone, R. Hillenbrand, and F. H. Koppens, Nature Communications **7**, 1 (2016).

[158] R. Kraft, M. H. Liu, P. B. Selvasundaram, S. C. Chen, R. Krupke, K. Richter, and R. Danneau, arXiv **2006.14995** (2020).

[159] S. Russo, M. F. Craciun, M. Yamamoto, A. F. Morpurgo, and S. Tarucha, Physica E: Low-Dimensional Systems and Nanostructures **42**, 677 (2010).

[160] F. Xia, V. Perebeinos, Y. M. Lin, Y. Wu, and P. Avouris, Nature Nanotechnology **6**, 179 (2011).

[161] J. C. Cuevas and F. S. Bergeret, Physical Review Letters **99**, 1 (2007).

[162] R. V. Gorbachev, J. C. W. Song, G. L. Yu, A. V. Kretinin, F. Withers, Y. Cao, A. Mishchenko, I. V. Grigorieva, K. S. Novoselov, L. S. Levitov, and A. K. Geim, Science **346**, 448 (2013).

[163] V. Panchal, A. Lartsev, A. Manzin, R. Yakimova, A. Tzalenchuk, and O. Kazakova, Scientific Reports **4**, 1 (2014).

[164] A. Lherbier, B. Biel, Y. M. Niquet, and S. Roche, Physical Review Letters **100**, 1 (2008).

[165] C. R. Dean, L. Wang, P. Maher, C. Forsythe, F. Ghahari, Y. Gao, J. Katoch, M. Ishigami, P. Moon, M. Koshino, T. Taniguchi, K. Watanabe, K. L. Shepard, J. Hone, and P. Kim, Nature **497**, 598 (2013).

[166] P. Moon and M. Koshino, Physical Review B **90**, 1 (2014).

[167] A. Lodder and N. Y. V, Phys. Rev. B **58**, 5783 (1998).

[168] M. T. Allen, O. Shtanko, I. C. Fulga, J. I. Wang, D. Nurgaliev, K. Watanabe, T. Taniguchi, A. R. Akhmerov, P. Jarillo-Herrero, L. S. Levitov, and A. Yacoby, Nano Letters **17**, 7380 (2017).

[169] T. A. Fulton and L. N. Dunkleberger, Phys. **9**, 4760 (1974).

[170] J. Clarke, A. N. Cleland, M. H. Devoret, D. Esteve, and J. M. Martinis, Science **239**, 992 (1988).

[171] M. H. Devoret, J. M. Martinis, and J. Clarke, Physical Review Letters **55**, 1908 (1985).

[172] L. Fu and C. L. Kane, Physical Review Letters **100**, 1 (2008).

7

[173] J. Alicea, Physical Review B - Condensed Matter and Materials Physics **81**, 1 (2010).

[174] A. Y. Kitaev, Physics-Uspekhi **44**, 131 (2001).

[175] J. D. Sau, R. M. Lutchyn, S. Tewari, and S. Das Sarma, Physical Review Letters **104**, 1 (2010).

[176] D. Aasen, M. Hell, R. V. Mishmash, A. Higginbotham, J. Danon, M. Leijnse, T. S. Jespersen, J. A. Folk, C. M. Marcus, K. Flensberg, and J. Alicea, Physical Review X **6**, 1 (2016).

[177] F. Harper, A. Pushp, and R. Roy, Physical Review Research **1**, 1 (2019).

[178] A. Fornieri, A. M. Whiticar, F. Setiawan, E. Portolés, A. C. Drachmann, A. Keselman, S. Gronin, C. Thomas, T. Wang, R. Kallaher, G. C. Gardner, E. Berg, M. J. Manfra, A. Stern, C. M. Marcus, and F. Nichele, Nature **569**, 89 (2019).

[179] W. Mayer, M. C. Dartiailh, J. Yuan, K. S. Wickramasinghe, A. Matos-Abiague, I. Žutić, and J. Shabani, arXiv **1906.01179**, 1 (2019).

[180] K. C. Nowack, E. M. Spanton, M. Baenninger, M. König, J. R. Kirtley, B. Kalisky, C. Ames, P. Leubner, C. Brüne, H. Buhmann, L. W. Molenkamp, D. Goldhaber-Gordon, and K. A. Moler, Nature Materials **12**, 787 (2013).

[181] C. Charpentier, S. Fält, C. Reichl, F. Nichele, A. Nath Pal, P. Pietsch, T. Ihn, K. Ensslin, and W. Wegscheider, Applied Physics Letters **103**, 28 (2013).

[182] M. Yankowitz, Q. Ma, P. Jarillo-Herrero, and B. J. LeRoy, Nature Reviews Physics **1**, 112 (2019).

[183] M. Kharitonov, Physical Review B - Condensed Matter and Materials Physics **85**, 1 (2012).

[184] I. F. Herbut, Physical Review B - Condensed Matter and Materials Physics **75**, 1 (2007).

[185] J. D. Sanchez-Yamagishi, T. Taychatanapat, K. Watanabe, T. Taniguchi, A. Yacoby, and P. Jarillo-Herrero, Physical Review Letters **108**, 1 (2012).

[186] J. Talvacchio, M. A. Janocko, and J. Greggi, Journal of Low Temperature Physics **64**, 395 (1986).

[187] P. Rickhaus, M.-H. Liu, M. Kurpas, A. Kurzmann, Y. Lee, H. Overweg, M. Eich, R. Pisoni, T. Tamaguchi, K. Wantanabe, K. Richter, K. Ensslin, and T. Ihn, arXiv , 1 (2019).

[188] K. K. Kim, A. Hsu, X. Jia, S. M. Kim, Y. Shi, M. Dresselhaus, T. Palacios, and J. Kong, ACS Nano **6**, 8583 (2012).

[189] A. Lale, E. Scheid, F. Cristiano, L. Datas, and B. Reig, Thin Solid Films **666**, 20 (2018).

[190] Y. Zhang, Y. W. Tan, H. L. Stormer, and P. Kim, Nature **438**, 201 (2005).

7

[191] B. Özyilmaz, P. Jarillo-Herrero, D. Efetov, D. A. Abanin, L. S. Levitov, and P. Kim, Physical Review Letters **99**, 2 (2007).

[192] K. Zimmermann, A. Jordan, F. Gay, K. Watanabe, T. Taniguchi, Z. Han, V. Bouchiat, H. Sellier, and B. Sacépé, Nature Communications **8**, 1 (2017).

[193] D. S. Wei, T. Van Der Sar, J. D. Sanchez-Yamagishi, K. Watanabe, T. Taniguchi, P. Jarillo-Herrero, B. I. Halperin, and A. Yacoby, Science Advances **3**, 1 (2017).

[194] R. Steinigeweg, F. Jin, D. Schmidtke, H. De Raedt, K. Michielsen, and J. Gemmer, Physical Review B **95**, 1 (2017).

[195] N. J. Couto, D. Costanzo, S. Engels, D. K. Ki, K. Watanabe, T. Taniguchi, C. Stampfer, F. Guinea, and A. F. Morpurgo, Physical Review X **4**, 1 (2014).

[196] Y. Kim, P. Herlinger, T. Taniguchi, K. Watanabe, and J. H. Smet, ACS Nano **13**, 14182 (2019).

[197] S. Zihlmann, P. Makk, M. K. Rehmann, L. Wang, M. Kedves, D. Indolese, K. Watanabe, T. Taniguchi, D. M. Zumbühl, and C. Schönenberger, ar **2004.02690**, 1 (2020).

[198] M. L. Della Rocca, M. Chauvin, B. Huard, H. Pothier, D. Esteve, and C. Urbina, Physical Review Letters **99**, 1 (2007).

[199] I. O. Kulik and A. N. Omel'yanchuk, JETP Letters **21**, 96 (1975).

[200] A. A. Golubov, M. Y. Kupriyanov, and E. Il'ichev, Reviews of Modern Physics **76**, 411 (2004).

[201] E. M. Spanton, M. Deng, S. Vaitiekenas, P. Krogstrup, J. Nygård, C. M. Marcus, and K. A. Moler, Nature Physics **13**, 1177 (2017).

[202] M. D. Thompson, M. Ben Shalom, A. K. Geim, A. J. Matthews, J. White, Z. Melhem, Y. A. Pashkin, R. P. Haley, and J. R. Prance, Applied Physics Letters **110**, 1 (2017).

[203] C. D. English, D. R. Hamilton, C. Chialvo, I. C. Moraru, N. Mason, and D. J. Van Harlingen, Physical Review B **94**, 1 (2016).

[204] L. F. Shatz and C. W. Christensen, PLoS ONE **9** (2014), 10.1371/journal.pone.

[205] K. Ueda, S. Matsuo, H. Kamata, S. Baba, Y. Sato, Y. Takeshige, K. Li, S. Jeppesen, L. Samuelson, H. Xu, and S. Tarucha, Science Advances **5**, 1 (2019).

[206] C. L. Kane and E. J. Mele, Physical Review Letters **95**, 0 (2005).

A Fabrication Recipes

In the following we give the detailed fabrication recipes used to build the nano structures.

A.1. Van der Waals heterostructure fabrication

A.1.1. Material sources

1. Graphite: NGS Trading & Consulting GmbH, natural graphite source

2. HOPG: HQ-graphene

3. hBN: T. Taniguchi et al., National Institute for Material Science, 1-1 Namiki, Tsukuba 305-0044, Japan

4. Exfoliation tape: NITTO ELP-150P-LC

A.1.2. Annealing

1. Forming gas: H_2/N_2 (8%/92%)

2. Pressure 10-50 mbar

3. Ramping to 300 $^\circ$C in 30 min

4. Hold temperature for 3-4 hours

5. Cool down to 30 $^\circ$C in 30 min

A.2. Reactive ion etching

A.2.1. CHF$_3$/O$_2$

1. CHF$_3$/O$_2$ (40 sccm/4 sccm); power 60 W; pressure 60 mTorr

2. Etching rates:
   - hBN: 0.3-0.33 nm/s

- SiO$_2$: ∼0.23 nm/s

- graphite: 0.07 nm/s

A.2.2. SF$_6$/Ar/O$_2$

1. SF$_6$/Ar/O$_2$ (20 sccm/5 sccm/4 sccm); power 50 W; pressure 25 mTorr

2. Etching rates:
   - hBN: >6.35 nm/s
   - SiO$_2$: ∼0.5 nm/s

3. After the SF$_6$ etching a O$_2$ plasma (A.2.3) was used to remove cross-linked PMMA.

A.2.3. O$_2$

1. O$_2$ (20 sccm); power 60 W; pressure 40 mTorr

2. Etching rates:
   - hBN: ∼0.33 nm/s
   - PMMA: ∼1.66 nm/s

A.2.4. O$_2$ prior ALD

1. O$_2$ (16 sccm); power 30 W; pressure 250 mTorr; time 20 s

A.3. Electron beam lithography

A.3.1. PMMA mask for etching and contact deposition

1. PMMA 950k diluted in Anisole (solid content 4.5-5.5%)

2. Spin coat at 4000 rpm for 40 s with ramp rate of 1000 rpm/s ($\approx 450\,nm$)

3. Back out at 180 °C for 3 min

4. Exposure with e-beam (EHT=20 kV; dose≈400 μC/cm^2)

5. Development in cold (∼5 °C) IPA:H$_2$O (7:3) for 60 s

6. Blow dry with N$_2$

A.3.2. PMMA lift-off

1. Sample in Acetone (T=50 °C) for 30 min

2. Remove remaining metal by Acetone flow created with a syringe

3. Transfer sample into IPA

4. Wash off Acetone

5. Blow dry with N_2

A.4. Metal deposition

A.4.1. Fabrication of 1D MoRe contacts

1. PMMA mask defined by EBL (A.3.1)

2. CHF_3/SF_6 etching (A.2)

3. Sputter MoRe using a AJA ATC Orion

4. Ignite plasma (Ar 30 sccm, pressure 20 mT, power 50 W)

5. Presputter for 1-2 min

6. Adjust parameters according to sputtering recipe

7. Single MoRe (1:1) target:
   - power 100 W
   - background pressure 2 mTorr
   - Ar flow 30 sccm
   - Sample rotation "on"
   - hight 40 cm
   - rate 0.27 nm/s

8. Co-sputtering:
   - power$_{Mo}$ 200 W; power$_{Re}$ 35 W
   - background pressure 10 mTorr
   - Ar flow 30 sccm
   - hight 20 cm
   - rate 0.19 nm/s

9. Lift-off in Acetone (A.3.2)

A.4.2. Fabrication of Au contacts

1. PMMA mask defined by EBL (A.3.1)

2. CHF$_3$/SF$_6$ etching (A.2) was used for 1D contacts

3. The metal was deposited using a Sharon e-beam evaporator

4. 5 nm of Ti or Cr was deposited as a sticking layer

5. Evaporate Au

6. Lift-off in Acetone (A.3.2)

A.4.3. Fabrication of metal top gates

1. PMMA mask defined by EBL (A.3.1)

2. Short CHF$_3$ (3-5 s) etching (A.2) to increase the adhesion

3. The metal was deposited using a Sharon e-beam evaporator

4. 5 nm of Ti or Cr was deposited as a sticking layer

5. Evaporate Au

6. Lift-off in Acetone (A.3.2)

A.5. Growth of aluminium oxide

1. O$_2$ cleaning step (see App.A.2.4)

2. growth of Al$_2$O$_3$ by atomic layer deposition

   - build sample into main chamber
   - preheat chamber to 225°C
   - perform 250 cycles:
   - open water source for 0.05 s
   - wait for 12 s
   - open trimethylaluminium source for 0.04 s
   - wait for 10 s

3. this results in an Al$_2$O$_3$ thickness of 30 nm

A.6. PC mixture

1. clean glass vial with chloroform and magnetic stirring bar

2. add 0.7 g of Poly(Bisphenol A carbonate)

3. add 20 ml of chloroform

4. close the vial and seal it with parafilm

5. let it stir over night at 40° C to dissolve the PC

A

Curriculum Vitae

David I. Indolese
Born on 19$^{\text{th}}$ January 1991 in Laufenburg (Switzerland)

Education

8/2016–10/2020	**PhD in experimental physics at the University of Basel**

- Dissertation in the group of Prof. Dr. C. Schönenberger
  "Engineered graphene Josephson junctions probed by quantum interference effects"

9/2014–6/2016	**Masters of Science in Physics at the University of Basel**

- Master thesis in the group of Prof. Dr. C. Schönenberger (University of Basel)
  "Spin pumping into graphene detected by inverse spin Hall-effect"

- Project work in the group of Prof. Dr. C. Schönenberger (University of Basel)
  "Fabrication and characterization of amorphous superconducting films by co-sputtering"

9/2012–8/2014	**Bachelors of Science in Physics at the University of Basel**
9/2010–8/2012	**Bachelors of Science in Physics at ETH Zürich**
2009	**Matura** Gymnasium Muttenz, Basel-Landschaft

Positions

8/2016–10/2020	*Teaching assistant for physics at the University of Basel*
9/2015–1/2016	*Teaching assistant for mathematics at the University of Basel*

Publications

- *"Compact SQUID realized in a double layer graphene heterostructure"*
  D.I. Indolese, P. Karnatak, A. Kononov, R. Delagrange, R. Haller, L. Wang, P. Makk, K. Watanabe, T. Taniguchi, and C. Schönenberger
  Nano Lett. **20**, 7129 (2020)

- *"Signatures of van Hove Singularities Probed by the Supercurrent in a Graphene-hBN Superlattice"*
  D.I. Indolese*, R. Delagrange*, P. Makk, J.R. Wallbank, K. Watanabe, T. Taniguchi, and C. Schönenberger
  Physical Review Letter **121**, 137701 (2018)

- *"Wideband and On-Chip Excitation for Dynamical Spin Injection into Graphene"*
  D.I. Indolese*, S. Zihlmann*, P. Makk, C. Jünger, K. Thodkar, and C. Schönenberger
  Physical Review Applied **10**, 044053 (2018)

- *"Current-phase relation, Inductance and Screening of a Graphene based rf-SQUID"*
  R. Haller, G. Fülöp,, **D.I. Indolese**, K. Watanabe, T. Taniguchi, and C. Schönenberger
  in preparation

- *"Mobility enhancement in graphene by in situ reduction of random strain fluctuations"*
  L. Wang, P. Makk, S. Zihlmann, A. Baumgartner, **D.I. Indolese**, K. Watanabe, T. Taniguchi, and C. Schönenberger
  Physical Review Letter **124** 157701 (2020)

- *"Out-of-plane corrugations in graphene based van der Waals heterostructures"*
  S. Zihlmann, P. Makk, M.K. Rehmann, L. Wang, M. Kedves, **D.I. Indolese**, K. Watanabe, T. Taniguchi, D.M. Zumbühl, and C. Schönenberger
  Phys. Rev. B **102**, 195404 (2020)

A

- *"Experimental demonstration of the suppression of optical phonon splitting in 2D materials by Raman spectroscopy"*
  M. De Luca, X. Cartoixà, **D.I. Indolese**, J. Martín-Sánchez, K. Watanabe, T. Taniguchi, C. Schönenberger, R. Trotta, R. Rurali, and I. Zardo
  2D Materials **7** 035017 (2020)

* Equal contribution

Talks

- *Widerstandsloser Elektronentransport in 2D*
  Outreach University of Basel, Basel (Switzerland), February 2020

- *Tuneable interference pattern in a planar graphene SQUID*
  Graphene Workshop 19, Budapest (Hungary), October 2019

- *Fabrication of Graphene based Nanoelectronics*
  User Event 2019 of SNI's Nano Imaging Lab, Basel (Switzerland), June 2019

- *Supercurrent in a hBN-graphene moiré superlattice*
  Lunch Seminar - QCQT PhD School, Basel (Switzerland), November 2018

- *Supercurrent in a hBN-graphene moiré superlattice*
  TopoGraph Kick-off Meeting, Budapest (Hungary), September 2018

- *Supercurrent in a hBN-graphene moiré superlattice*
  Graphene Workshop 18, Basel (Switzerland), June 2018

- *Graphen mit supraleitenden Kontakten*
  Outreach SNI, Basel (Switzerland), May 2018

- *Edge current in hBN-graphene moiré superlattice*
  14$^{\text{th}}$ Capri Spring School on Transport in Nanostructures, Capri (Italy), April 2018

- *Towards topological states in graphene superconducting devices*
  QSIT junior Meeting, Passugg (Switzerland), June 2017

A

Poster Contributions

- *"Superconducting proximity effect in hBN-graphene moiré superlattice"*
  697. WE-Heraeus-Seminar, Bad Honnef (Germany), June 2019

- *"Superconducting proximity effect in hBN-graphene moiré superlattice"*
  IWEPNM 19, Kirchberg (Austria), March 2019

- *"Signatures of van Hove singularities probed by the supercurrent in a graphene - hBN superlattices"*
  Graphene Week, San Sebastian (Spain), September 2018

- *"Graphene superconducting hybrid devices"*
  QSIT Junior Meeting, Passugg (Switzerland), June 2017

- *"Novel quantum transport features in low-dimensional systems"*
  QSIT General Meeting, Arosa (Switzerland), January 2017

Acknowledgements

After four years as a PhD student I look back on a great time, with a lot of interesting physics, with ups and downs, and with a lot of support and guidance of great people and scientists, without whom this work would have been impossible. They gave me the opportunity to get in touch with the very interesting and broad field of nano-electronics & quantum transport and to gain a deeper understanding of the underlying physical phenomena. Therefore, I want to thank all these people in the following lines.

In the first place I want to thank Prof. Dr. Christian Schönenberger, who gave me the opportunity to pursue the research summarized in this thesis. With his open mind, great interest in the field and liberal leadership style he creates an ideal working space for young scientist to explore and develop their skills by encouraging them to realize their own ideas and by giving critical input when it is needed. Especially, I want to thank Christian, that he hired me after my master thesis even though the funding situation in the beginning was difficult, which needed several proposals to be sorted out. The group trips were always a great opportunity to learn more about ones fellow students and get in touch with different cultures and backgrounds, which created a collaborative and sympathetic environment.

I also want to thank Dr. Srijit Goswami and Dr. Sophie Guéron for taking part in my doctoral committee, for their critical review of my thesis, and I really appreciate their expenditure of time.

Especially, I feel blessed for the great support in all belongings by my supervising post-docs, with whom I had the pleasure to work in the past four years. All of them contributed to my research and scientific education. First I want to thank Dr. Raphaëlle Delagrange, who supervised my during the first two years of my PhD and teached my a lot of valuable knowledge about superconductivity, Josephson junctions, the counter measurement, and research in general. Together we spent quite some time in the lab and shared depressing, but luckily mainly great moments. Further, I want to thank Dr. Paritosh Karnatak and Dr. Artem Kononov, who supported me in the second half of my PhD and were open to any scientific or science regarding discussions. Their input helped me many times to sort my thoughts and plan the next steps. A big thanks goes as well to Dr. Péter Makk, who always stayed interested in the progress of my research even after he went back to Budapest. With his

A

broad knowledge about the field, he raised many times the right concerns and pointed out open questions of the field, which have not been answered yet.

I also want to thank every member of the 2D team, which I had the pleasure to be a part of. They were always willing to help and open-minded to discuss and realize new ideas. I remember making my first stacks together with Dr. Clevin Handschin, who shared all his fabrication experience with me and took a lot of time to show me everything step by step. I also appreciate all the help of Dr. Simon Zihlmann, who already supervised my master thesis. His broad knowledge and his huge drive gave my research a big boost, since it gave me the opportunity to make a lot of different experiences in the lab from which I could profit afterwards. But I also want to thank him for the common time we spent beyond the work, for all the discussion, the hospitality in Basel when the last train was already departed, and the excavation in the garden for the pool. Further I want to thank Dr. Lujun Wang, with whom I shared many experiences during the fabrication and measurements of our devices. The close exchange of knowledge and thoughts facilitated our life in the lab a lot. I never want to miss the conferences we visited together with all the people we met, ideas we discussed and the best piece of beef we shared in San Sebastian. At this point I also thank Martin Endres for his efforts in the lab as the clean room responsible to keep the things running and the interest plus working power he invested in our common project - graphene Josephson junctions on $SrTiO_3$, which sadly did not work out so far. Of course I don't want to miss to thank Matthijs Hermans, Zarina Mingazheva, Mehdi Ramezani, Blesson Varghese, Ian Correa Sampaio, and Fabian Oppliger for the nice talks about different 2D materials and 2D research, which broadened my horizons.

A special thanks goes to my friends Dr. Gergő Fülöp and Roy Haller. It was great to get in touch with radio-frequency measurements and to realize a joint project together, which would have been impossible without their expertise and commitment. With both of them I share many memories for which I am very grateful.

I also like to thank Lukas Gubser and Dr. Paritosh Karnatak for covering my back while I was writing my thesis by taking care of the scanning electron microscope and the supervision of my successor Matthijs Hermans.

The time during my PhD was not only exciting due to the explored physics, but as well due to the people with whom one gets and stays in touch. With my former fellwo students the dPW, namely Roy Haller, Oliver Braun, David Marti, Dr. Sebastian Wagner, Kenneth Marschall and Partick Hümbeli, I spent many nice evenings cooking, eating, drinking, discussing and just enjoying life. Sometimes we also obtained new ideas for our research and combined our different expertises to try something new. For taking these opportunities I want to thank Oliver Braun and Dr. Peter Rickhaus, even though we struggled a lot and the outcome was little, but this also belongs to science.

At this point I would like to thank as well Dr. Christian Jünger, who